DOKUZ EYLÜL UNIVERSITY
GRADUATE SCHOOL OF NATURAL AND APPLIED SCIENCES

BIO-OPTICAL CHARACTERISTICS OF MEDITERRANEAN SEA: LIGURIAN SEA

by
Fethi BENGİL

August, 2015
İZMİR

BIO-OPTICAL CHARACTERISTICS OF MEDITERRANEAN SEA: LIGURIAN SEA

A Thesis Submitted to the
Graduate School of Natural and Applied Sciences of Dokuz Eylül University
In Partial Fulfillment of the Requirements for the Degree of Doctor of Philosophy in Marine Science and Technology, Living Marine Resources Program

by
Fethi BENGİL

August, 2015
İZMİR

Ph.D. THESIS EXAMINATION RESULT FORM

We have read the thesis entitled **"BIO-OPTICAL CHARACTERISTICS OF MEDITERRANEAN SEA: LIGURIAN SEA"** completed by **FETHİ BENGİL** under supervision of **PROF. DR. ŞÜKRÜ T. BEŞİKTEPE** and we certify that in our opinion it is fully adequate, in scope and in quality, as a thesis for the degree of Doctor of Philosophy.

Prof. Şükrü T. BEŞİKTEPE

Supervisor

Prof. Dr. H. Baha BÜYÜKIŞIK

Thesis Committee Member

Yrd. Doç. Dr. A. Hüsnü ERONAT

Thesis Committee Member

Prof. Dr. Dilek EDIGER

Examining Committee Member

Doç. Dr. E. Yesim ÖZKAN

Examining Committee Member

Prof.Dr. Ayşe OKUR

Director

ACKNOWLEDGMENT

I am always grateful to my supervisor Prof. Dr. Şükrü Turan Beşiktepe, for his supervision and providing me many opportunities to improve my skills through out my study period. I would like to thank to the thesis committee members; Prof. Dr. Hasan Baha Büyükışık and Assist. Prof. Dr. Atilla Hüsnü Eronat for their valuable comments. I also want to thank to my colleague Assoc. Dr. Murat Gündüz for his help. He has never given up to answer my questions. I thank also “OSS2015” EU 7th Frame project.

I am grateful to Dr. Charles Trees and Dr. Violeta Sanjuan Calzado from CMRE for their help, critiques and advices throughout the PhD period. I will always follow their scientific way to teach, to share my knowledge as they did for me. I have appreciated the scientific and engineer teams of BP’09 Cruise and crew of “RV/ Alliance” for providing extensive dataset of the Ligurian Sea.

I am especially grateful to Dr. David McKee for his endless help, critiques and advices. He was like my second supervisor for the last year of my PhD period. I will always remember our long discussions during my “wee” visit to his laboratory.

I am grateful to my friends, Vahit Alan, Murat Özaydınlı, Gökhan Kaboğlu, Sinem Oğuz, Barış Akçalı, Janset Kankuş for their motivation throughout the PhD period. They always listened me, when I need.

I would like to give special thanks to my precious, my life, and my darling, my Elizabeth Grace Tunka. Thesis would not be completed without her support and motivation. I am grateful to have you in my life.

I am deeply grateful to my precious family for their love and unconditional support. I cannot find adequate words to express my appreciation; I love them.

Fethi BENGİL

BIO-OPTICAL CHARACTERISTICS OF MEDITERRANEAN SEA: LIGURIAN SEA

ABSTRACT

Physical and bio-optical data were analyzed to understand and represent bio-optical characterization of the Ligurian Sea in highly productive season and water types were identified based on IOPs in view of the combined use of optical measurements and ecosystem modeling. Physical measurements showed two distinctive zones in the Ligurian Sea, central and coastal zone, as parallel to the common knowledge of the Ligurian Sea. Bio-optical measurements indicated two distinctive particulate populations, which define bio-optical water types in the Ligurian Sea with agreement with physical properties. Physical properties and bio-optical properties of the study area are strongly linked to each other. Based on understanding the bio-optical properties, a bio-optical model was developed provide an effective characterization the optical properties of the region. Developed model is validated using independent data set. Validation results showed that major features of the optical characteristics of the region have been satisfactorily captured in the bio-optical model. Validation results showed also the model is better than the previous models due to the inclusion of non-biogenic material in addition to biogenic material.

Keywords: Bio-optical characterization, chlorophyll, total suspended solids, salinity, bio-optical model, Ligurian Sea

AKDENİZ'İN BİYO-OPTİK ÖZELLİKLERİ: LİGURYA DENİZİ

ÖZ

Akdeniz'in bilimsel anlamda en iyi bilinen bölgelerinden biri olan Ligurya Denizi'nin biyo-optik özelliklerini belirlemek ve modellemek için fiziksel ve biyo-optik verisetleri analiz edilmiştir. Fiziksel ölçümler, Ligurya Denizi ile ilgili genel bilgilere uygun olarak, birbirinden farklı özellikler gösteren iki bölgenin olduğunu göstermiştir. Biyo-optik ölçümler de, fiziksel özelliklere uygun olarak, alanda birbirinden farklı partikül populasyonlarına sahip iki bölgenin varlığına işaret etmektedir. Fiziksel ve biyo-optik verisetlerinden yapılan analizler, fiziksel ve biyo-optik özellikler arasında güçlü bir ilişki olduğunu göstermiştir. Belirlenen biyo-optik özelliklerin karakterizasyonunu sağlamak üzere bir biyo-optik model geliştirilmiş ve geliştirilen bu model bağımsız bir veriseti ile test edilmiştir. Validasyon sonuçları, biyo-optik model tahminlerinin alanın genel biyo-optik özelliklerini temsil ettiğini göstermiştir. Ayrıca, geliştirilen modelin alanda önceden kullanılmış olan modellerden daha iyi sonuçlar verdiği görülmüştür. Bunun nedeni, modelde biyolojik olmayan maddelerin de hesaba katılmasıdır.

Anahtar kelimeler: Biyo-optik karakterizasyon, klorofil, toplam askıda katı madde, tuzluluk, biyo-optik model, Ligurya Denizi

CONTENTS

Page

LIST OF FIGURES

Page

LIST OF TABLES

Page

CHAPTER ONE
INTRODUCTION

1.1 General Introduction

The temporal and spatial variability of oceanic optical properties are fundamental to many biogeochemical processes in the sea (Dickey & Falkowski, 2002). Underwater light fields regulate photosynthesis, contribute to solar heating and determine ocean color remote sensing signals. In recent years it has become increasingly apparent that coupled physical-ecosystem models require appropriate representation of the underwater light field, particularly in the context of using ocean color remote sensing data for assimilation and validation (Rothstein et al., 2006; Dickey, Lewis, & Chung, 2006). Advances in computing power and availability of fast and accurate radiative transfer models (e.g. Ecolight, Sequoia Scientific) offer the potential to incorporate comprehensive light field models into aquatic ecosystem models, with the promise of significant improvements in the prediction of biogeochemical and physical properties.

Early attempts to integrate light field models into coupled ecosystem models tended to use very basic approaches to modeling the underwater light field. For example, Beşiktepe, Lermusiaux, & Robinson (2003) used the chlorophyll concentration (Chl) and the Lambert-Beer law to obtain attenuation coefficients and from this estimate underwater light fields. Recent studies have adopted more sophisticated approaches to model underwater light fields (e.g. Fujii, Boss, & Chai, 2007; Shulman et al., 2013; Ciavatta et al., 2014). Future efforts, incorporating full solution of the radiative transfer equation, will require parameterization with a complete set of inherent optical properties (IOPs). Moreover, there will be a need to relate these IOPs to relevant ecosystem model currencies in order to track evolution of the light field in time with changes in physical and biogeochemical properties of the system. Considerable effort has already gone into the development of bio-optical models for different natural water systems (Prieur & Sathyendranath, 1981; Gordon & Morel, 1981; Morel, 1988; Bricaud, Roesler, & Zaneveld, 1995; Bricaud, Morel, Babin, Allali, & Claustre1998; Loisel & Morel, 1998; Morel & Maritorena, 2001; Velluci, 2007; Morel, 2009).

Most bio-optical models are constructed using optically active constituents (OACs) as currency terms, with typical components such as: phytoplankton, detrital or non-algal particles and colored dissolved organic material (CDOM). Even such a simple scheme presents difficulties in terms of relating optical variables to parameters that can be included in an ecosystem model currency scheme. Phytoplankton is the least awkward component, usually being represented by chlorophyll concentration as a proxy currency. The remainder of the particle population is much harder to define. In open ocean systems, operating under the Case 1 definition, other particles may be assumed to be derived from the phytoplankton population, e.g. detrital particles and associated bacterial populations, and these might also be related to Chl. However, in shallow coastal waters there is also the potential for significant populations of non-biogenic particles from terrigenous sources or from benthic re-suspension. These particles are unlikely to be related to Chl and must, instead, be represented by some measure of total suspended solid concentration (TSS). However, given the contribution from phytoplankton and associated biogenic materials to TSS, there is an a priori requirement for consideration of further refinement of this parameterization to account for the 0complex nature of the particle population. CDOM is also problematic when considering Case 1 versus Case 2 scenarios. Under the Case 1 approach, CDOM is assumed to be a product of algal-related biological activity and has been successfully related to Chl for open ocean waters. However, coastal areas subject to riverine inputs will present CDOM signals that are unrelated to Chl. Here there are grounds for investigating the potential of relating CDOM signals to salinity given the association with freshwater inputs (e.g. Bowers, Harker, Smith, & Tett, 2000).

The study area for this paper is the Ligurian Sea, which is located in the northwestern part of the Mediterranean Sea between southeast France, northwest Italy and the island of Corsica (Figure 1). This is an area, which has been extensively studied previously with well-established circulation patterns, e.g. Astraldi &

Gasparini (1992). Cyclonic circulation in the Ligurian Sea leads to the formation of three distinct hydrological zones; a thermal front (frontal zone) which separates less dense warm coastal peripheral water (coastal zone) from denser cold offshore water (central zone) (Picco et al., 2010). These structures are permanent but show some seasonal and interannual variability (Astraldi, Gasparini, Manzella, & Hopkins, 1990; Picco et al., 2010). The upper layer of the Ligurian Sea has seasonal differences in nutrient ratios with changes from nitrate limitation in winter to phosphate limitation in summer due to seasonal hydrological regime variations (Marty, Chiaverrini, Pizay, & Avril, 2002). Nutrient availability is controlled by vertical mixing and determines the timing of algal blooms. Winter mixing leads to the formation of a winter – early spring bloom while a second bloom in April – May depends on subsequent mixing events (Raick, Delhes, Soetaert, & Gregory, 2005).

1.2 Aim of The Study

The main aim of this study is to develop and test a bio-optical model for the Ligurian Sea, which uses chlorophyll-a and total suspended solid concentrations and salinity that can be obtained from a coupled physical-ecosystem model, based upon derivation of mass-specific inherent optical properties with different versions for deep offshore waters and shallow, optically complex coastal waters. This is an important step for establishing a conceptual framework to integrate a robust bio-optical model into future coupled physical-ecosystem models. The choice of optically active components currency parameters (Chl, TSS and Salinity) reflect parameters that could be obtained both from autonomous in situ sensor systems and from ecosystem model outputs. Chl and TSS may also be derived from ocean color remote sensing, whilst salinity can be obtained from microwave remote sensing e.g. Aquarius.

The thesis is concentrated on the following objectives to meet the aim:

- Describing the physical properties of the Ligurian Sea. Physical properties have strong relationships with bio-optical properties. Physical properties are important to understand dynamics of the study area.

- Describing the inherent and apparent optical properties of the Ligurian Sea. Bio-optical properties help to understand bio-optical water types in the study area. The modeling effort is required for understanding the properties of water masses that effect the performance of the model.

- Qualities of the datasets are important for setting up and testing the model. Datasets can be used separately with empirical, model and direct measurements to evaluate the results for the approaches.

- After confirming and concluding the previous objectives, developing, running and testing a bio-optical model for the Ligurian Sea.

CHAPTER TWO
LITERATURE SURVEY

2.1 Ocean Optics

2.1.1 Inherent Optical Properties

When light passes through the aquatic media, there are two factors that change its properties within the media; absorption and scattering. Absorption and scattering properties of the aquatic media are called Inherent Optical Properties (IOPs). These properties depend only on the amount and composition of optically active components and do not depend on the light fields within aquatic media. Absorption is the capturing of the photon to obtain its energy by molecules that transform the radiative energy to different energy forms within the aquatic media. Scattering is the deviation in the direction of the incident photon with losing its radiative energy or no change in its radiative energy by matter within the media. Volume scattering function is used to define angular distribution of scattered light after dispersing of the light beam to parameterize scattering and it is another component of inherent optical properties.

Absorption coefficient, a(λ), which is used to define absorption and identified as absorbed part of incident flux (A), is normalized by dividing thickness of passed layer (Δr) (Eq. 2.1). Scattering coefficient, a(λ), is used to define absorption and identified as deviated part of incident flux (B, by dividing deviated from incident flux to incident flux) that is normalized by dividing thickness of passed layer (Eq. 2.2). Volume scattering function (also known as VSF and β(ψ;λ)) is the deviated part of incident flux in unit solid angle (ψ) and unit volume. Its integration in scattered angles between 0° and π also gives scattering coefficient (Eq. 2.3).

$$a(\lambda)=\lim_{\Delta r\to 0}\left(\frac{A(\lambda)}{\Delta r}\right) \qquad (2.1)$$

$$b(\lambda)=\lim_{\Delta r \to 0}\left(\frac{B(\lambda)}{\Delta r}\right) \quad (2.2)$$

$$b(\lambda)=2\pi\int_{0}^{\pi}\beta(\psi;\lambda)\sin\psi d\psi \quad (2.3)$$

Scattering is used commonly in studies of ocean optics in two main groups as backward (backscattering) and forward scattering coefficients based on angular integration of VSF besides total integration of VSF. Forward scattering coefficient is the integration of VSF between 0° and π/2, while backscattering coefficient is the integration of VSF between π/2and π.

Another term is attenuation coefficient in IOPs. Attenuation coefficient, c(λ), defines the whole lost energy by interaction of light and matter. It is obtained by sum of absorption and scattering coefficient (Eq. 2.4)

$$c(\lambda)= a(\lambda)+b(\lambda) \quad (2.4)$$

2.1.2 The Radiance Fields

The radiance fields are important to understand how much available light for photosynthesis and distribution of underwater light (Kirk, 2011). Mostly used variables are radiance and irradiance to define the underwater radiance fields. These variables might change only with the physical ambient, even though the IOPs remain the same. Thus, they can call as candidate Apparent Optical Properties (AOPs) (Oceanopticbook, n.d.).

The most easily measured properties of underwater light are radiance and irradiance. Radiance at a point in space, as function of the direction, L(θ, ϕ), is the radiant flux (Φ) at that point in a given direction per unit solid angle per unit area (dS) at right angles to the direction of propagation (Eq. 2.5). Definition of the irradiance at a point of a surface, E; is the radiant flux incident on an infinitesimal element of a surface, containing the point under consideration, divided by the area of that element (Eq. 2.6). In other words, it is the integration of radiance in interested surface (e.g. net irradiance in Eq. 2.7). Relationship between radiance and irradiance are presented in Figure 2.1.

Quantity of the radiance is difficult to measure due to many angles needed for complete description of the light field. Useful properties are used based on the aim of the designed studies. Most used integrations are upwelling irradiance (E_u), which is the radiance integration of upper side of the horizontal plane, and downwelling irradiance (E_d), which is the radiance integration of lower side of horizontal plane. Difference between E_u and E_d is also defined as net irradiance. If these integrations are done in upper and lower hemisphere, instead of horizontal plane, scalar upwelling (E_{ou}) and scalar downweling irradiance (E_{od}) will be obtained, respectively.

$$L(\theta, \phi)= d^2\Phi/dS\cos\theta d\omega \tag{2.5}$$

$$E= d\Phi/dS \tag{2.6}$$

$$\vec{E}= \int_{-4\pi} L(\theta, \phi)\cos\theta d\omega \tag{2.7}$$

2.1.3 Apparent Optical Properties

Apparent optical properties (AOPs) are the light properties that not only depend on aquatic medium but also the directional structure of the radiant field. They also show stability to explain aquatic medium. Irradiance is also known as the candidate AOPs (Oceanopticbook, n.d.) due to its possibility to change easily and greatly according to the changes in the light field, thus it is difficult to explain aquatic medium. Certain ratios of the radiant fields at certain thicknesses of depth are better describers, because changes in ambient light have less influence and changes in components of aquatic media have more influence on them. These facts give them advantage for describing changes in aquatic media. Using ambient radiant field and, thus, direct measurement ability makes them also commonly used by researchers.

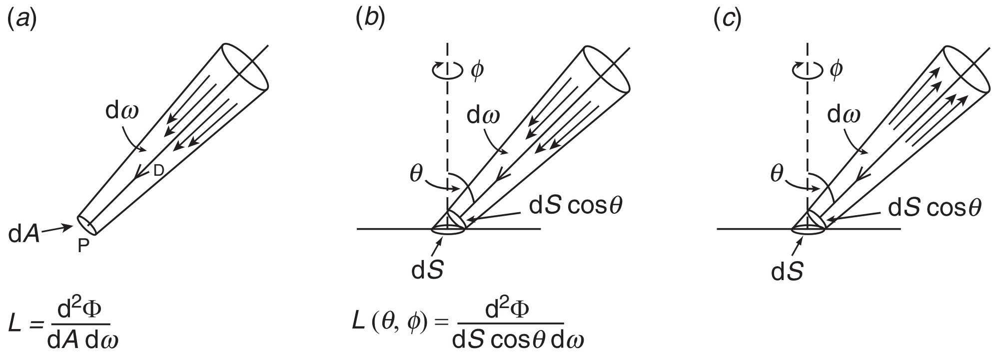

Figure 2.1"Definition of radiance. (a) Field radiance at a point in space. The field radiance at P in the direction D is the radiant flux in the small solid angle surrounding D, passing through the infinitesimal element of area dA at right angles to D divided by the element of solid angle and the element of area. (b) Field radiance at a point in a surface. It is often necessary to consider radiance at a point on a surface, from a specified direction relative to that surface. dS is the area of a small element of surface. L(θ, ϕ)is the radiance incident on dS at zenith angle θ (relative to the normal to the surface) and azimuth angle ϕ: its value is determined by the radiant flux directed at dS within the small solid angle, do, centred on the line defined by θ and ϕ. The flux passes perpendicularly across the area dScosθ, which is the projected area of the element of surface, dS, seen from the direction θ, ϕ. Thus the radiance on a point in a surface, from a given direction, is the radiant flux in the specified direction per unit solid angle per unit-projected area of the surface. (c) Surface radiance. In the case of a surface that emits radiation the intensity of the flux leaving the surface in a specified direction is expressed in terms of the surface radiance, which is defined in the same way as the field radiance at a point in a surface except that the radiation is considered to flow away from, rather than on to, the surface" (Kirk, 2011).

Most commonly used AOPs are diffuse attenuation coefficients at certain layer of depth (K(z)) and reflectances (R). Different K(z) and R such as downwelling diffuse attenuation coefficient and remotely sensed reflectance can be derived by using different ratios of radiant fields. Spectral diffuse attenuation coefficient, $K_d(z; \lambda)$, defines diminishing of light at a layer of depth (Eq. 2.8) and is used commonly in ecological study for understanding the penetration of light in water column to relate it with photo-physiological processes. Remote sensing reflectance (R_{rs}) is the ratio between the water leaving radiance (upwelling radiance just above the sea surface) and downwelling irradiance just above the sea surface (Eq. 2.9). It is very important for remote sensing studies and also is mentioned by Sanjuan-Calzado (2009) as "R_{rs} presents very little dependence on sun angle and strong dependence on water optical properties, absorption and scattering, which makes it an ideal AOP in optical modeling".

Optical depth is a term relating AOP to express the light fields and is obtained by $1/K_d$. Optical depth is not the real depth; it describes how much diminution of irradiance occurs when light travels through aquatic media. Even though real depth can change, optical depth always defines the same light condition, e.g. 4.6th optical depth is euphotic depth that real depth varies depending on aquatic media.

$$K_d(z,\lambda)=-E_d(z,\lambda)\frac{dEd}{dz} \tag{2.8}$$

$$R_{rs}(\theta,\phi,\lambda)=\frac{L_w(\theta,\phi,\lambda)}{E_d(z=0^+,\lambda)} \tag{2.9}$$

2.1.4 Radiative Transfer Equation

Radiative transfer model explains simply the relationship between IOPs and AOPs. IOPs and environmental conditions are used as input. The radiant fields are obtained by using radiative transfer equation (RTE) and then, AOPs are derived (Figure 2.2).

RTE describes radiance changes from any point in the aquatic media. Some assumptions are required for solving the radiative transfer equation. Assumptions are layered horizontally in the aquatic media, constant radiance; that is monochromatic and polarized, at surface and omitted fluorescence emissions. Based on these assumptions, change in radiance in certain zenith and azimuth angles (θ, ϕ, respectively) at depth (z) is a result of the loss by attenuation along the distance passed through and gain by scattering that comes from other directions, which is determined by volume scattering function in the angle between the two directions; θ, ϕ and θ′, ϕ ′(Eq. 2.10). Schematic representation of the RTE is shown in Figure 2.3

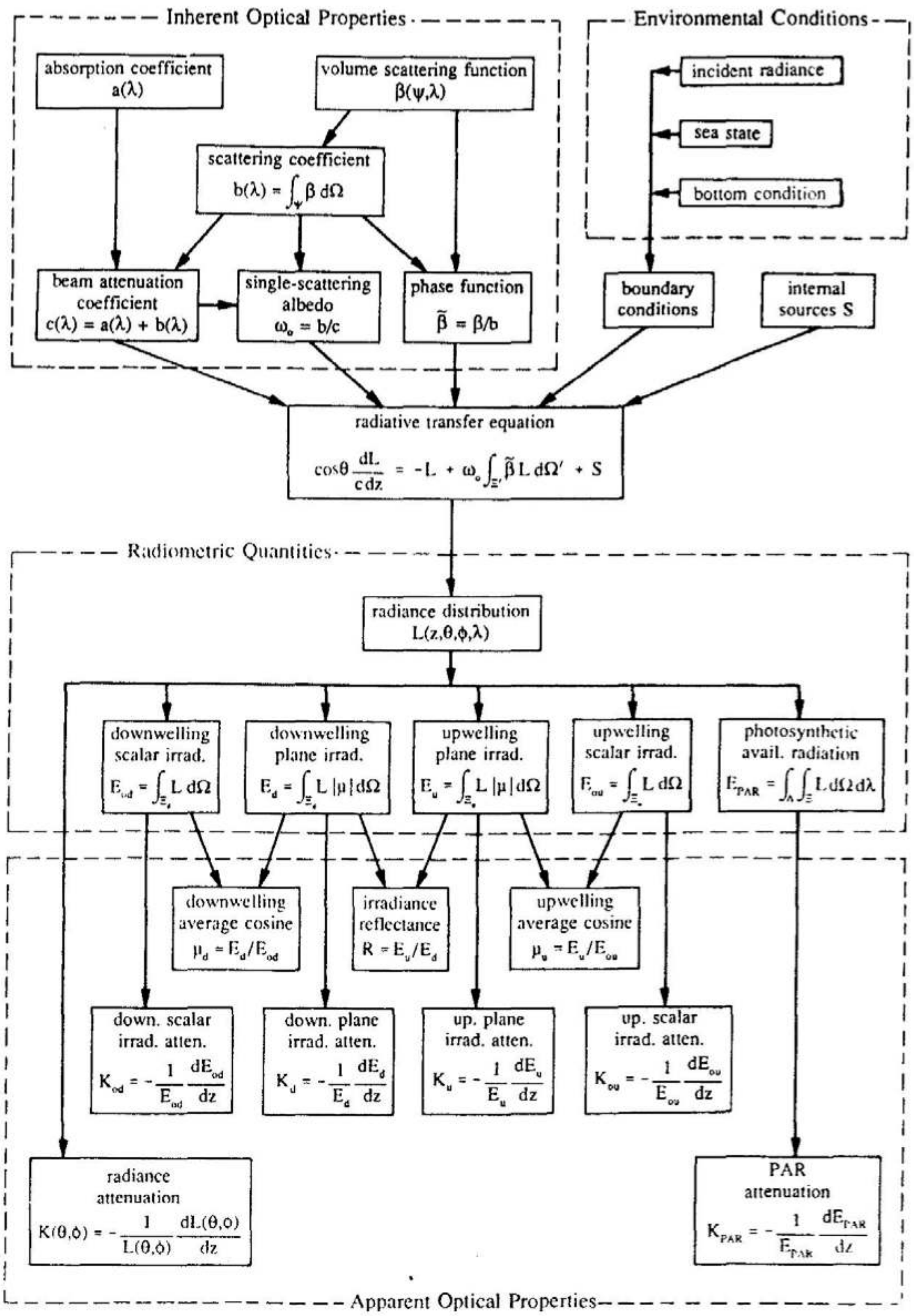

Figure 2.2 Schematic flow chart of radiative transfer modeling and relationship connections of IOPs and AOPs (Mobley, 1994).

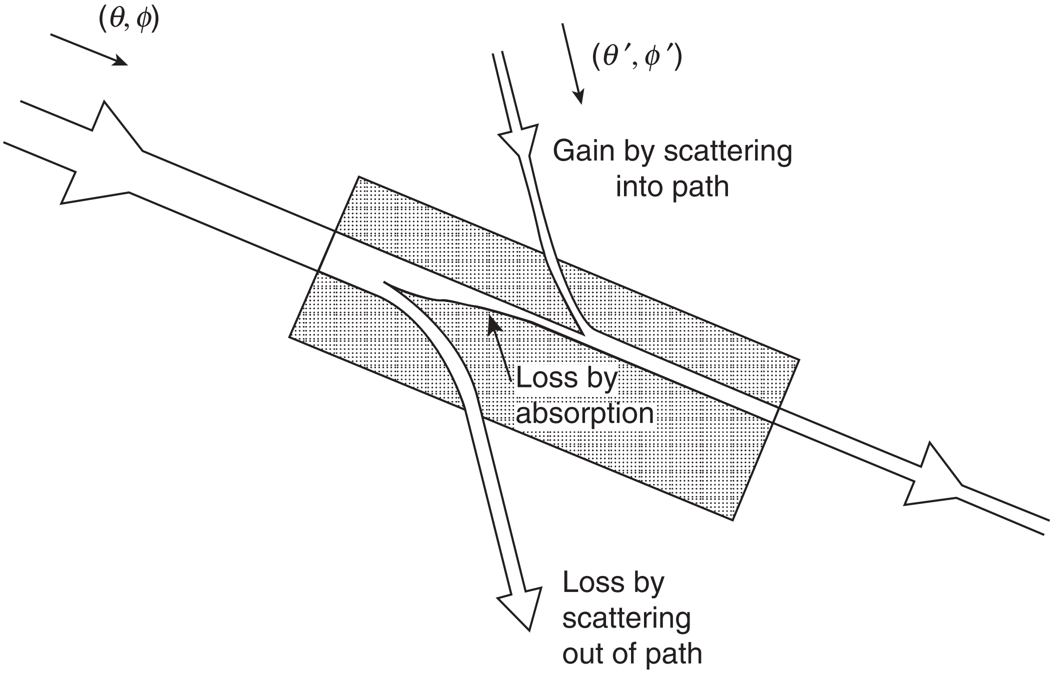

Figure 2.3The schematic presentation of the RTE for the radiance (illustration from Kirk (2011)).

$$\cos\theta \frac{dL(z,\theta,\phi)}{dz} = -c(z)L(z,\theta,\phi) + \int_{2\pi} \beta(z, \theta, \phi; \theta', \phi')L(z,\theta',\phi')d\omega((\theta',\phi') \qquad (2.10)$$

2.1.5 Optically Active Constituents in Seawater

Optically active constituents (OACs) are the matters that affect the optical properties of the seas. They have strong bonds especially with inherent optical properties, which can express as function of OACs (Sanjuan-Calzado, 2009). Constituents, which are classified in OACs, are grouped based on similarity in their optical properties. Relevant to this study, main groups of OACs are seawater itself, colored dissolved organic matters (CDOM), non-algal particles and phytoplankton. There are many studies conserning these main groups that are linked to inherent optical properties. These groups are also obtained as variables or related to variables of the ecosystem models. Relationships between OACs and IOPs are explained in the content of the model development in Chapter 4.4.

2.1.5.1 Water

Optical properties of the water as the media of OACs are well known. Absorption of the water is strong in red region of visible spectrum while it shows increasing trend through to blue region and has very weak absorption in blue region. Seawater absorption changes modestly due to temperature, salinity and pressure. Smith & Baker (1981) conducted measurements for the spectrum of seawater absorption with an assumption of negligible impact of salinity. Accurate measurements of the water absorption with high sensitivity were done by Pope & Fry (1997) using integrating cavity absorption meter.

Spectral scattering properties of seawater show exponential relationship with wavelengths, that can be expressed as mathematical relation. While the scattering coefficient decreases, the wavelength increases. Backscattering and forward scattering coefficients contribute half and half by theoretical study of Morel (1974).

2.1.5.2 Phytoplankton

Phytoplankton is the most complicated group to model due to different physiological and optical properties of different phytoplankton taxa. Even though the modeling has difficulties, most common approach is to use Chlorophyll-a to express inherent or apparent optical properties for this main group. Chlorophyll pigments are most contributed pigments, especially Chlorophyll-a, among pigment types. This dominancy makes it possible to express relationship between phytoplankton and inherent optical properties with a degree of uncertainty.

Absorption coefficient by phytoplankton is an important source to define optical properties in oceanic waters (Case 2 waters). This fact is pointed out in many studies (Bidigare, Schofield, & Prezelin, 1989; Hoepffner & Sathyendranath, 1991; Aguirre-Gomez, Weeks, & Boxall, 2001; Barlow et al., 2002; Velluci, 2007). Spectral absorption characteristic of phytoplankton shows two important peaks; one is big in blue region and another one is relatively small in red region. Absorption is very low in green region. Variations in spectral pattern of the phytoplankton absorption are due to packaging affect, intensity of the light, quality and availability of the nutrient, circadian rhythms and other sources of variability from oceanic circulation as well as composition of phytoplankton taxa, that have various physiological features (Velluci, 2007). Most common used expressions are normalized absorption by phytoplankton named under specific inherent optical properties (SIOPs) and SIOP models that are expressed as exponential relation with application to global or local coefficients.

Scattering at phytoplankton is one of the challenges in optical oceanography due to limitation in measurement and varies from one species to another. Finding isolated phytoplankton species is hard in natural waters. There are other OACs as well as other species of phytoplankton in seawater. It should also be noted that some specific backscattering and scattering measurements are available for some certain species from culture studies in laboratory. However, backscattering ratio has variation among species due to some species having inorganic shelves all over the wall of the cells with different inorganic compounds and patterns. Most used measurements in sea water are done by volume scattering meters to obtain converted backscattering coefficient in empirical methods, and then scattering can be obtain by analytical relations. Power-fit relationship between chlorophyll-a and backscattering or scattering coefficient are used for parameterization of these variables.

2.1.5.3 Non-algal Particles

Main components for this group are inorganic particles such as minerals from rivers or atmosphere and organic matters such as detritus, other planktonic groups besides phytoplankton. This group is known with weak absorption but high backscattering properties.

Absorption by non-algal particles shows some differences depending on the particle types; spectral shape of the absorption can model as decreasing exponential function from blue region to red region with a reference wavelength in the blue region, generally at 440 nm. The absorption is assumed negligible in the red region, while main contribution is seen in blue region. The empirical relationships are defined from local or global datasets to derive reference absorption coefficient by non-algal particles.

Inorganic composition of non-algal particles such as minerals are known to have high scattering and particularly high backscattering properties since they are inorganic substances. They contribute in high ratio to total scattering compared to phytoplankton, thus existence of these groups are very important to define the bio-optical water types.

2.1.5.4 Colored Dissolved Organic Matter

Colored dissolved organic matter (CDOM) is the fulvic acid and humic acid part of the dissolved organic matter that is the formation of the degradation of organic matter and exudates by organisms. Other common names for this group are 'yellow substance', 'gelbstoff' and 'gilvin'. Main source for CDOM in oceanic water is from degradation of phytoplankton cells. The source in coastal area varies depending on terrestrial and/or atmospheric inputs such as rainfall and river flow with water soluble humic substance.

Absorption spectrum of the CDOM is similar to the absorption spectrum of non-algal particles, but amplitude of the absorption coefficient shows generally higher than absorption by non-algal particles. It has decreasing exponential distribution from blue region to red region. Chlorophyll-a can be related with the absorption by CDOM in offshore regions because of having phytoplankton as main source, while this relationship is deviated due to carried substance from the terrestrial.

Scattering by CDOM, which is the dissolved part of the OACs, is generally considered as negligible.

2.2 Models

2.2.1 Ecosystem Modeling

Ecosystem is a dynamic system of biogeochemical processes that have interactions with environmental stresses. Ecosystem models are defined as mathematical tools with a series of differential equations to understand and predict environmental processes as a representation of the real world in temporal and spatial scales (Gregoire & Oğuz, 2008) diverse from simple nutrient-phytoplankton-zooplankton (NPZ) models to more complex models with many state variable and interactions with different medias. There are many successful applications of ecosystem models in the marine environment. An example representation of compartments in an ecosystem model is given in Figure 2.5

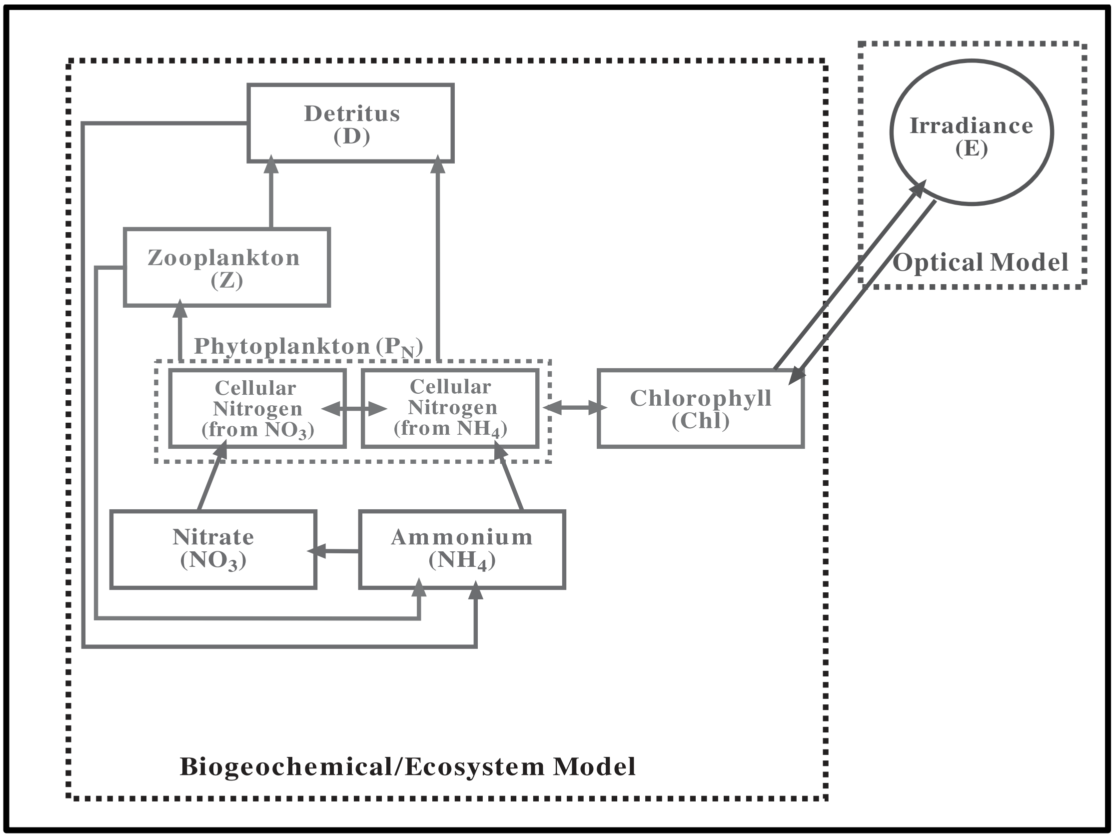

Figure 2.4 Schematic representation of components of ecosystem model (Beşiktepe, 2003).

Using modeling of biogeochemical processes in the marine environment has increased rapidly in the last three decades. “Ecosystem models seek to reproduce and predict ocean biogeochemical cycles, where the models are constrained by physical parameters such as; wind, currents, density and light. The hydrographic aspects of marine ecosystems can generally be defined through ocean circulation models, which are largely independent of the ecosystem itself and represent external forcing on ecosystem models. On the other hand the physical optics, determining the light environment, are two-way coupled with ecosystem models. Because light interacts with particles as defined by the biogeochemical processes, the specification of the optical behavior of the seawater and its constituents should be considered a crucial element of any ecosystem model” (Trees et al., 2012). An example schematic representation of coupled physical-ecosystem model is given in Figure 2.5

“Originally, a primary function of marine ecosystem models was to help in the development of understanding; also, they were applied in fisheries models to predict the abundance of specific commercial fish stocks. Now, they are being asked to do much more. On local and regional scales, there is growing recognition that management of marine resources and assessment of human perturbations must encompass the whole ecosystem, not individual species.” (Rothstein, 2006).

2.2.2 Bio-optical Models

Morel (2009) defined two meanings for the term of bio-optical models; while the first meaning of the term is; tools used to analyze, and then predict, the optical properties of biological materials, the second meaning which is more related to this study, refers to ways of describing and forecasting the ‘bio-optical state’ of the aquatic media as functions of biological activities. These functions are related with both, IOPs and AOPs of water and might be empirical, descriptive or derived from field measurements.

Chlorophyll-a concentration is generally used for this purpose to quantify algal content as dominant pigment group. This approach is reasonable for oceanic waters;

however, bio-optical properties are determined with the contribution of substances that originate from terrestrial sources in coastal waters. This fact shows the requirement of local set-up and practical methods to use bio-optical models for further purposes.

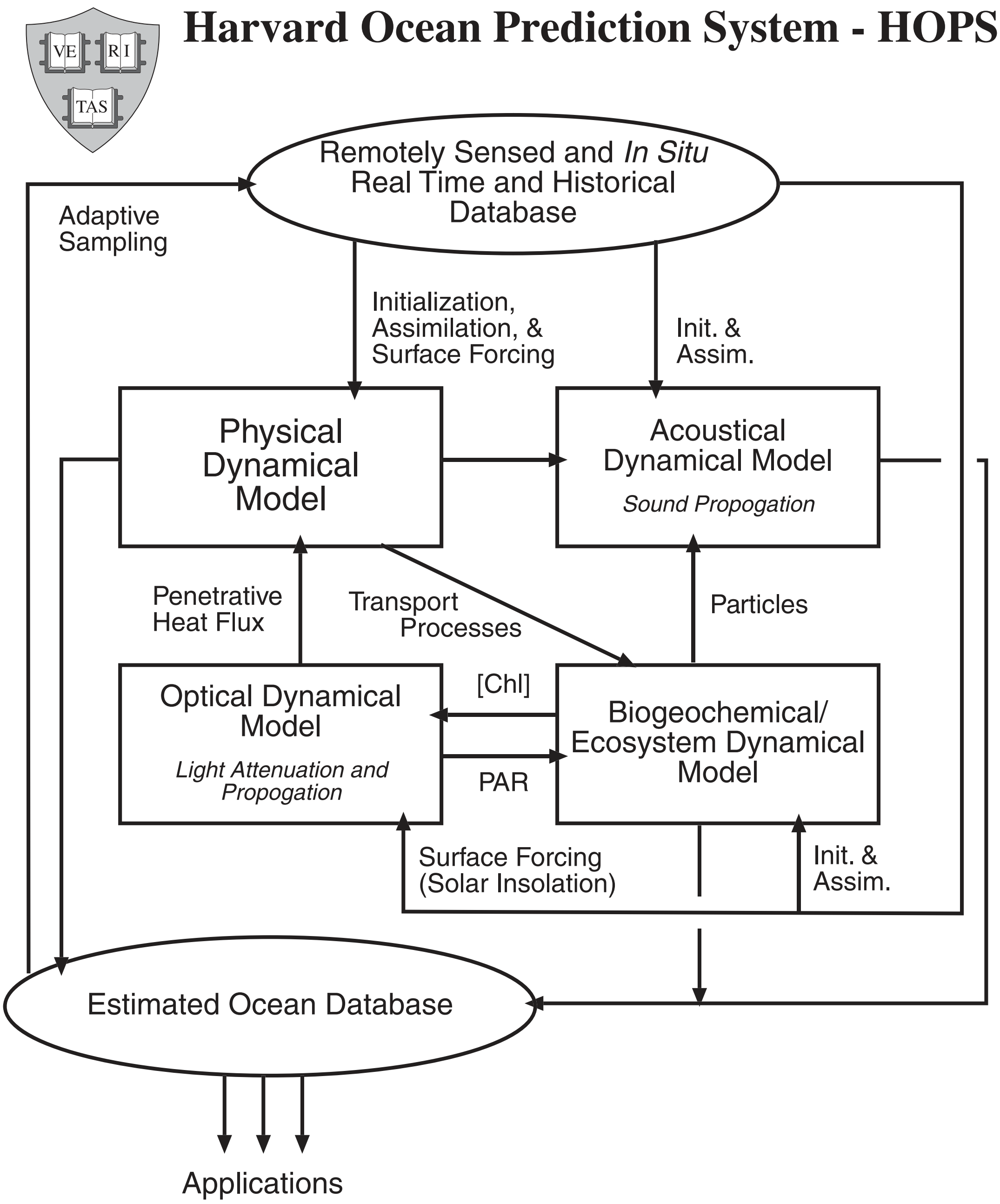

Figure 2.5 Schematic representation of coupled physical-ecosystem model (Beşiktepe, 2003).

Approach of coupled ecosystem models with bio-optics became popular in the last decade because the availability of estimating the underwater light distribution from state variables of the ecosystems models (Figure 2.6). This integration is relatively easy for oceanic waters where light fields are driven by phytoplankton, as it is still a big challenge and requires local set-ups for coastal waters. Application from literature shows the bio-optical integration from simple approaches to complex approaches.

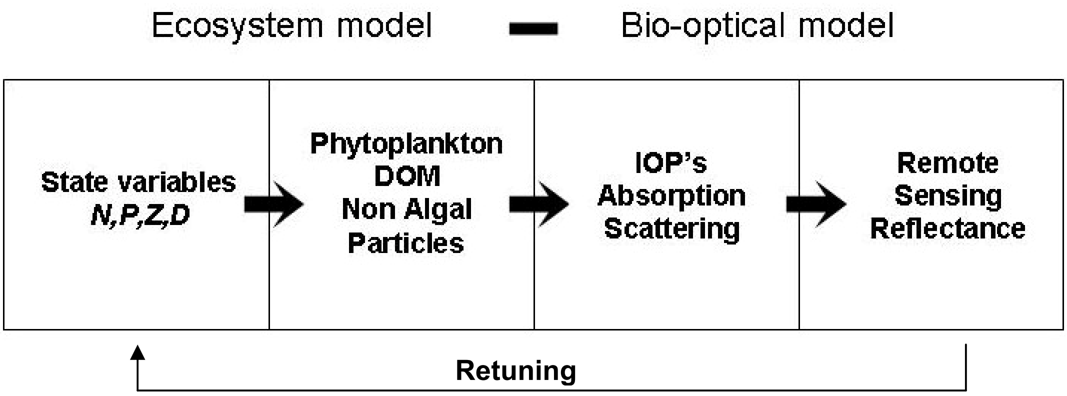

Figure 2.6 Schematic representation of conversion and connections between ecosystem and bio-optical models (Sanjuan-Calzado, 2009).

Underwater distribution and variability of PAR are important for marine ecosystem models to calculate the underwater light fields, particularly in euphotic zone, more accurately related to phytoplankton distribution and biomass.

The simple models are an application of Lambert-Beer law using attenuation coefficient of seawater. The approach calculates K_d parameter by using chlorophyll measurements at depths. K_d is the sum of attenuation of phytoplankton with contribution of chlorophyll measurement and seawater attenuation.

Another approach was offered by Lee, Du, Arnone, Liew, & Penta (2005). They used IOP derived from remotely sensed data to calculate K_d value with an empirical relationship between IOP and AOP. They assumed IOPs do not change (homogenously) in the water column. The approach that was presented by Penta et al. (2008) is extent scheme of the approach of Lee et al. (2005). Bio-optical conversions were used for non-homogenous waters to adapt K_d parameters in different depths. Absorption by water and specific chlorophyll absorption were used with chlorophyll concentration to calculate total absorption at each depth. Backscattering was obtained with conversion of scattering related with chlorophyll.

The most complex approach is to use radiative transfer models to link IOP, which is obtained from bio-optical model, and AOP. These models are computationally intensive. Even though it might be inefficient in large-scale, high-resolution ecosystem models, the results are more accurate. Fuji et al. (2007) is the first study to discuss coupled optical-ecosystem model. State variables were used to calculate absorption and scattering for aquatic media with OAC and radiative transfer modeling was applied to obtain AOPs. Then, the light fields retrieved from AOPs were used to redistribute biological activity, that are dependent to the light.

2.3 The Ligurian Sea

The Ligurian Sea, a branch of the Mediterranean Sea in the northwestern, lies among the northwestern coasts of Italy, coasts of the southeastern France (and Monaco) and the northern coasts of Corsica (French Island). As seen in Figure 2.7, the Ligurian Sea is an abyssal depression delimited by the shallow water shelf of the Tuscan Archipelago toward the southeast and largely opens toward the western Mediterranean. The continental shelf is narrow and steeps deeply (Esposito & Manzella 1982).

Eastern coasts of the Ligurian Sea has many river plumes; most significant impact is by the River Arno. It's impact is seen along the coast of Tuscany region of Italy

The northwestern part of the Mediterranean Sea, which includes the Ligurian Sea, is the most investigated and, thus, the most known region in the Western Mediterranean Sea (Astraldi & Gasparini, 1992). A general cyclonic circulation affecting Modified Atlantic Water (MAW) in surface layer and Levantine Intermediate Water (LIW) in deeper layer from surface to 1000 m deep (Astraldi & Gasparini, 1992; Esposito & Mazella, 1982) characterizes the Ligurian Sea. In result of affection of the cyclonic circulation, hydrological structure of the Ligurian basin has three distinct zones; Thermal front (as a frontal zone) separates less dense warm coastal peripheral water from denser cold central zone water (Picco et al., 2010). These structures in the Ligurian basin are permanent but show some variability during seasons and years depending on the features of the Tyrrhenian Current and the Western Corsica Current, which flows into the Eastern Ligurian Sea and merge there with each other (as named the Ligurian Provencal Current) (Astraldi et al., 1990; Picco et al., 2010).

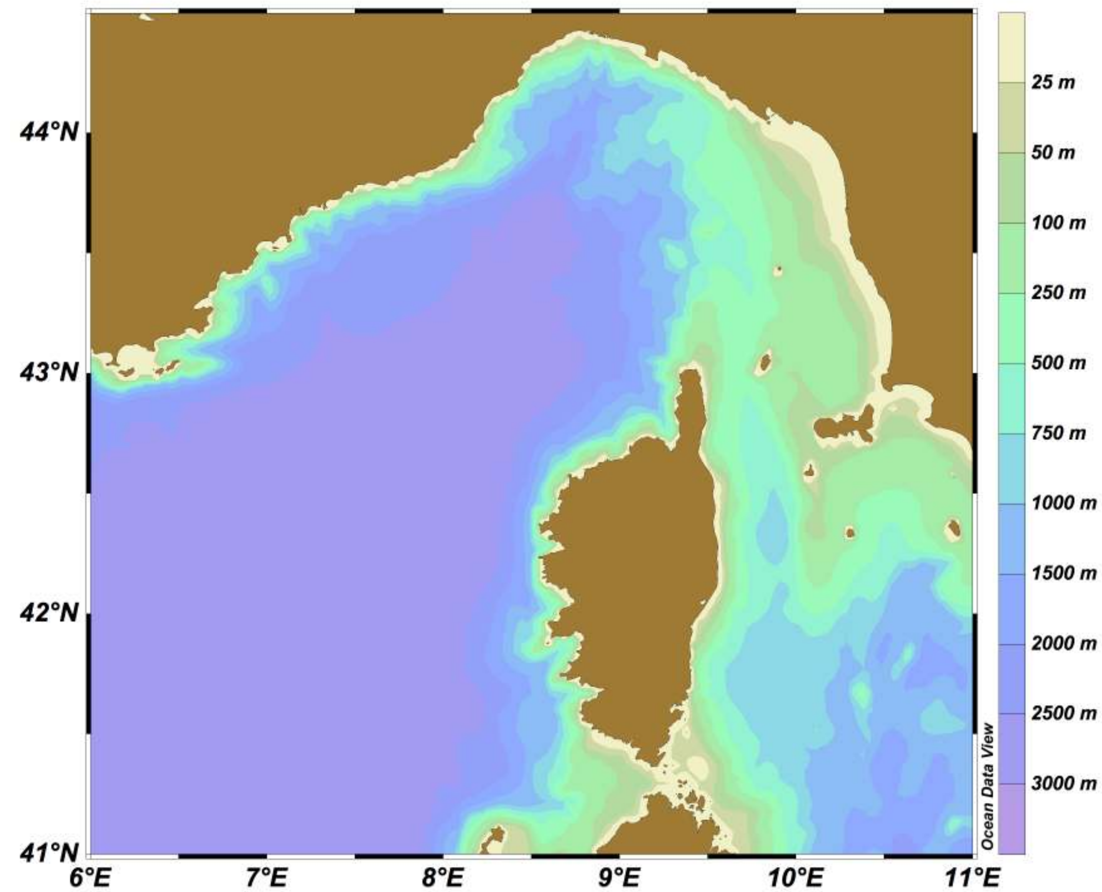

Figure 2.7 Bathymetry of the Ligurian Sea (The map is obtained from Ocean Data View software)

The Tyrrhenian Current is characterized with northward flowing water that moves through the Corsica Channel to the Eastern Ligurian Sea. Bathymetry of the Corsica Channel acts tı constrict the flow when moving northward. It has current oscillations thought the year, more energetic during the winter than summer, and may have inter-annual differences in current velocities. These oscillations and inter-annual differences in flow cause changes in amplitude of meanders and small eddies in the

Ligurian shelf in winter, where the current provides potential energy to help sustain the larger scale cyclonic circulation in the Ligurian basin in form of the Ligurian Current. The Tyrrhenian Current is a major source to define general characteristics of the water mass in continental shelf of the Ligurian Sea, even though runoff is available from local rivers such as Arno (Astraldi et al., 1990; Astraldi & Gaspardi, 1992).

The Western Corsican Current is another current that flows northward into the Eastern Ligurian Sea and moves from the northwestern side of the Island of Corsica. As mentioned by Astraldi & Gasparini (1992), the current maintains its stable feature with annual variability, but seasonal variability is important for lateral shifting in frontal zone; when the current is stronger, in late winter and spring, the front shifts closer to Italian coasts. When the current is weaker, in autumn, the front moves closer to central side of the Ligurian basin.

The study by Marty et al. (2002) based on DYFAMED station located in the central zone of Ligurian Sea shows that; phosphate is a limiting factor like the characteristics of the Mediterranean Sea. Surface layer has seasonal differences in nutrient ratios with a shift from nitrate limitation in winter to phosphate limitation in summer due to seasonal hydrological regime variations.

Vertical mixing is the main factor in biological productivity due to effect on distribution of nutrients. Winter-early spring blooms are seen after winter mixing and second bloom may be seen in April-May depending on availability of vertical mixing. After summer when nutrients are reduced due to shallow physical stratification, strong winds cause vertical mixing and there is another bloom in autumn related with the enrichment in nutrient of the surface layers (Raick et al., 2005).

As mentioned by Lazzara et al. (2010), a few studies have been carried in the eastern Ligurian Sea concerning phytoplanktonic communities. Northern Tuscany coasts in the Eastern Ligurian Sea are generally meso-oligotrophic by the effects of river inputs and pico-nano planktonic species dominant. Analyzed contribution of phytoplankton groups by Raick et al. (2005) shows also that nanoplankton group is dominant throughout the year and it is also dominant for PP in Ligurian Sea.

Lazzara et al. (2010) defined 3 sub-regions in the Ligurian Sea as oceanic (central), neritic (between oceanic and coastal), and coastal zones based on common physical and biological features; Ligurian oceanic zone feature shows a quite different seasonal pattern from the coastal zone because of both the primary productivity and the pelagic phyto-mass cycles. The coastal cycle is characterized as continuous throughout the season, with relatively high production from March to September. Spring bloom in March is seen in coastal zone, which has colder waters from rivers and terrestrial inputs, and time series analyses by ocean color support this fact.

Related with primary production, a large proportion of carbon budget occurs in oceanic waters, while coastal water has higher variance in time and spatial (Lazzara et al., 2010).

The Ligurian Sea has limited study on bio-optical properties even though it has wide bio-optical data set with cruises and moorings. Observations from northwestern coast to central zone of the Ligurian Sea by bio-optical glider in winter 2007 showed the highest particulate backscattering (at 470 nm) and lowest contribution of small particles over total particles were seen in the surface layer of coastal zone, whereas comparatively lower values of particulate backscattering (at 470) and higher contribution of small particles were seen in the surface layer of the central zone (Niewiadomska et al., 2008).

CHAPTER THREE
MATERIAL AND METHODS

3.1 Study Area

The data used in this study were collected during the BP09 Cruise between March 13th and 26th 2009 in the Ligurian Sea. Figure 3.1 shows the locations of the sampling stations. Stations can be classified into two groups; onshore and offshore. The onshore group includes stations located on the coastal shelf and along transects perpendicular to the coast. Terrigenous material from River Arno plume impacts a number of these stations significantly. The offshore group includes stations located in the Ligurian-Provencal Basin and represent deep, clear oceanic waters that are separated from the coastal zone by a permanent thermal front.

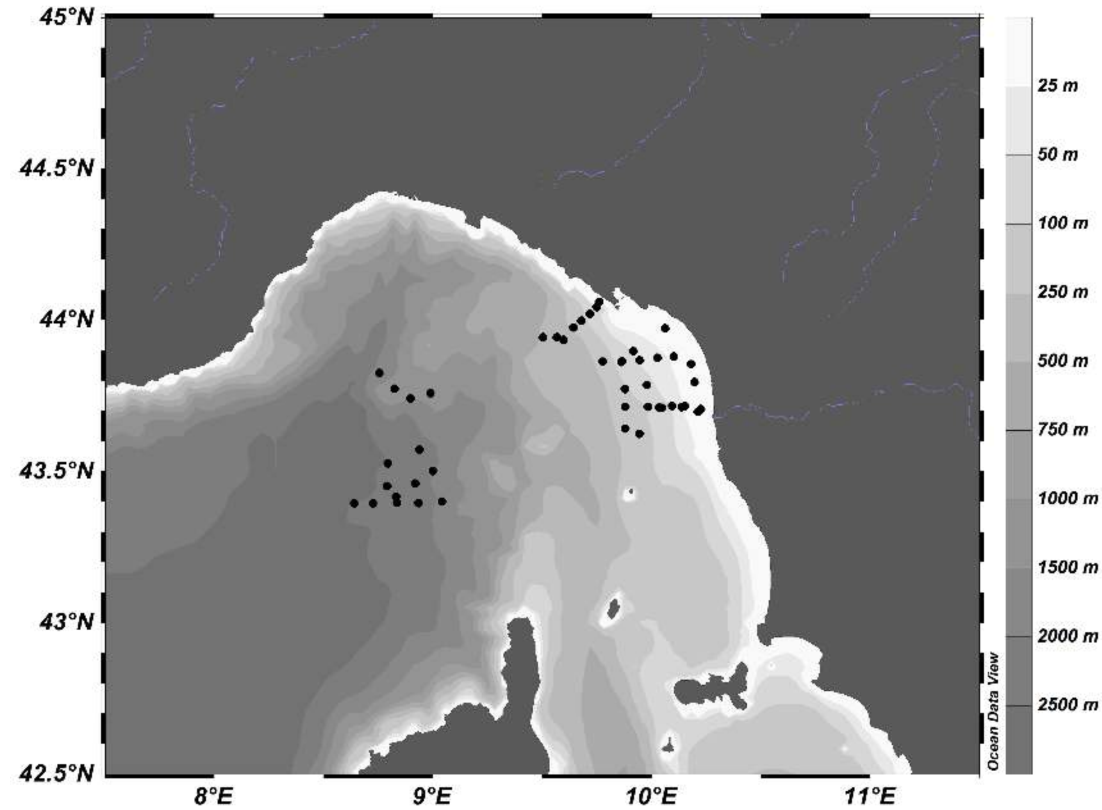

Figure 3.1 Study area and location of the stations in the Cruise BP'09.

3.2 The Data

All variables used in the study are listed in Table 3.1. Hydrographic measurements were made using a Seabird SBE 9 CTD system equipped with temperature, conductivity, fluorescence and turbidity sensors. Fluorescence data were calibrated using chlorophyll-*a* concentrations from HPLC measurements, while turbidity data were calibrated using total suspended solids measurements. These were used to generate proxy profiles of Chl and TSS subsequently used in modeling efforts.

Chlorophyll concentration was measured using standard HPLC measurements on samples filtered through GF/F filters, stored in liquid nitrogen and transported to laboratories for later analysis. Colleagues collected Chl data presented here from MUMM. The Marine Chemistry Laboratory of the MUMM using a reversed phase, acetone-based method with a C18 column and a Jasco FP-1520 fluorescence detector, analyzed triplicate HPLC samples. In this paper Chl refers to the Chlorophyll *a* concentration and does not include contributions from other pigments.

Total suspended solids concentrations (TSS) were obtained by colleagues from MUMM by filtering samples through pre-ashed, rinsed and pre-weighed 47mm GF/F filters. Samples were rinsed with several aliquots of ultrapure water, taking care to rinse the edge of the filter to minimize salt retention. Filters were stored frozen and returned to the lab where they were dried and reweighed.

The absorption of all dissolved and suspended components minus water was measured using a Point Source Integrating Cavity Absorption Meter (PSICAM) (Röttgers *et al.,* 2005, 2007; Röttgers & Doerffer, 2007). This instrument has previously been extensively validated and has been shown to provide very high accuracy (± 2 %) absorption coefficients across a wide range of water conditions. A 1 m liquid waveguide capillary cell (LWCC) with an Ocean Optics USB2000 mini-spectrometer was used to measure absorption by CDOM. This instrument is somewhat faster than the PSICAM and provides noise range of ± 0.0001 m^{-1} (95%

Prediction Interval) at 532 nm. In both cases, measurements were made against fresh Milli-Q references and all samples were corrected for the effects of salinity and temperature on water absorption (Röttgers & Doerffer, 2007). From these measurements particulate absorption, $a_p(\lambda)$, was derived by subtraction of CDOM absorption, a_{CDOM}, from PSICAM non-water absorption, a_{PSICAM} (Eq.3.1).

Table 3.1 List of variables that are used in the study.

Variable	Instrument	Numbers of Station	Comment
Temperature	Seabird SBE 9 system	44	
Salinity	Seabird SBE 9 system	44	Derived from conductivity sensor
Fluorescence	Chelsea Aqua 3	44	
Turbidity	Seapoint Turbidity	44	
Chlorophyll-a	HPLC	32	Marine Chemistry Lab. Of MUMM
Total Suspended Solids		35	
Absorption by CDOM	PSICAM, LWCC	35	
Absorption by particles	PSICAM	35	
Absorption by detrital	Beam spectrometer	35	
Absorption by phytoplankton	PSICAM, Beam spectrometer	35	Bysubtracting of detrital absorption from total particulate absorption.
Absorption coefficient	AC-9	42	without absorption by water
Attenuation coefficient	AC-9	42	
Scattering coefficient	AC-9	42	Bysubtracting of absorption from attenuation absorption with proportional scattering correction
Backscattering coefficient	BB9	42	
Downward Irradiance	Hyperpro free-falling profiler	44	
Upward radiance	Hyperpro free-falling profiler	44	

$$a_p = a_{g+p} - a_g \tag{3.1}$$

Particulate optical density (OD_p) was measured on freshly filtered samples using a Shimadzu UV-2501 PC dual beam spectrophotometer. Between 1 and 2 litres of sample were filtered through a 25 mm GF/F filter with nominal 0.7 μm retention limit which was mounted directly against the exit port of the spectrophotometer sample chamber. An unused GF/F filter, wetted with 0.2μm filtered seawater from the same station, was used as a reference sample and mounted on the reference port of the spectrophotometer. After measuring particulate optical density, the sample filter was exposed to a dilute sodium hypochlorite solution until visual loss of pigmentation occurred. The bleached filter pad was rinsed with 0.2 μm filtered seawater before being returned to the sample detector and a further scan for detrital optical density (OD_{det}) was completed. Detrital absorption spectra were visually examined to ensure that all pigment features, including phycobiliproteins, were removed. The sample was re-bleached and re-scanned if necessary. The absorption coefficient is obtained from Eq. 3.2.

$$a(\lambda)=2.303\,\frac{OD_{corr}A_{fp}}{\beta V_f} \qquad (3.2)$$

Where A_{fp} is the exposed area of the filter pad, V_f is the volume of sample filtered and β is the path length amplification factor. Filter pad absorption spectra were initially baseline corrected at 750 nm (Cleveland & Weidemann, 1993). Equation (3.2) can be rewritten for detrital absorption a_{det} by replacing OD_p with OD_{det}. Samples were corrected for path length amplification using a novel procedure described in detail in McKee et al. (2014). This approach uses linear regression of filter pad absorption against particulate absorption obtained by subtracting CDOM absorption from total non-water absorption measured by the PSICAM to provide both the path length amplification factor and offset correction for each sample. These values were then also used to correct bleached filter pad absorption measurements giving a_{det}, with phytoplankton absorption coefficients, a_{ph}, finally obtained by subtracting detrital absorption from total particulate absorption (Eq. 3.3).

$$a_{ph}(\lambda)=a_p(\lambda)-a_{det}(\lambda) \qquad (3.3)$$

In situ absorption and attenuation measurements were made with an AC-9 absorption and attenuation meter (WET Labs Inc.) with a 25 cm path-length operating at 412, 440, 510, 532, 555, 650, 676 and 715 nm. AC-9 measurements were calibrated during the cruise with ultrapure water (Milli-Q, Millipore) and the salinity and temperature dependence of pure water were corrected in all samples (Pegau, Grey, & Zaneveld, 1997) using data from a Seabird SBE 19plus CTD. The *proportional* correction by Zaneveld, Kitchen, & Moore (1994) was used to correct AC-9 absorption data for scattering collection errors. In situ backscattering measurements were made with a BB9 backscattering meter (WET Labs Inc.) operating at 412, 440, 510, 532, 595, 660, 676, 715 nm. BB9 data were linearly interpolated where necessary to match AC-9 wavelengths and were corrected for temperature, salinity and path length absorption effects in line with the manufacturer's instructions. The AC-9 and BB9 were deployed simultaneously, measuring IOPs from the surface to the maximum depth possible in shallow stations or down to a maximum of 100 m for deeper stations.

Radiometric data were collected using a Hyperpro (SatlanticInc.) free-falling profiler configured with hyper-spectral radiometric sensors measuring downwelling irradiance (E_d) and upwelling radiance (L_u), with a reference above-surface irradiance (E_s) sensor mounted at the highest point of the ship's superstructure. The profiling radiometer was deployed in a multicast mode to sample the surface layer repeatedly at each station enabling optimal calculation of light field parameters in the top 10 m. In addition, where possible, a deep radiometer cast collected enabling observation of light penetration below the surface layer. A bespoke data processing routine was developed to correct for changes in solar elevation during the cast sequence and to minimize the impact of surface effects.

Underwater light fields were modeled using EcoLight 5.0 (Mobley, Sequoia Scientific) running with IOPs derived from the bio-optical model developed below and Fournier – Forand scattering phase functions generated from particulate backscattering ratio ($b_{bp}(\lambda)/b_p(\lambda)$) following Mobley et al., (2002). Output wavelengths and depths were chosen to match AC-9 wavelengths and measured above surface downwards irradiance data were used to set boundary conditions. Raman scattering by water was included in simulations, but fluorescence contributions from CDOM and phytoplankton were not.

"NOMAD is a publicly available, global, high quality in situ bio-optical data set for use in ocean color algorithm development and satellite data product validation activities. Data products include coincident observations of water-leaving radiances and Chlorophyll a concentrations, along with relevant metadata, such as the date, time, and coordinates of data collection and binary processing flags. Inherent optical properties (IOPs; e.g., spectral absorption and backscattering coefficients) and aerosol optical thicknesses have been or will be included in the near future" (Seabass, n.d.).

Ocean color data obtained from NASA (http://oceancolor.gsfc.nasa.gov/cgi) were used to evaluate changes in Ligurian Sea in terms of sea surface temperature (SST) and diffuse attenuation coefficient at 490 nm (Kd 490). Products of SST obtained from MODIS Aqua (night time; appr. 1 km resolution) with Long-wave SST Algorithm (http://oceancolor.gsfc.nasa.gov/DOCS/modis_sst/) and products of K_d 490 nm obtained from MERIS Full Resolution images (appr. 300 m resolution) with an updated operational algorithm as defined in ocean color website (http://oceancolor.gsfc.nasa.gov/REPROCESSING/R2009/kdv4/). Images were chosen from cloud free days in the period of the cruise at the beginning of the cruise, just after wind mixing event and at the end of the cruise.

3.3 Variables

Previous studies define mean Chl concentration for first optical depth (Z_{pd}) that contributes approximately 90% to signal of water leaving radiance or euphotic zone (Z_{eu}) that 1% of surface PAR reaches (Morel, 1988;Morel & Maritorena, 2001;Velluci, 2007). In this study, euphotic zone is calculated by irradiance profiles and first optical depth is converted as Eq.3.4. PAR was calculated using Eq. 3.5 Cumulateded Chl concentration in euphotic zone and first optical depth was calculated, mean Chl concentration in Z_{eu} was calculated by Eq. 3.6 where z corresponds to $Z_{eu;}$ mean weighted Chl concentration in Z_{pd} was calculated by Eq. 3.7.

$$Z_{pd}=Z_{eu}/\ln(100) \tag{3.4}$$

$$PAR=\int_{400}^{700}\frac{\lambda}{hc}Ed(\lambda)d\lambda \tag{3.5}$$

$$[CHL]=\frac{1}{ZEU\text{-}ZO}\int_{ZO}^{Z}Chl(Z)DZ \tag{3.6}$$

$$Cm=\frac{\int_{Zo}^{Zpd}Chl(z)\exp(-2K(Z)dz}{\int_{Zo}^{Zpd}\exp(-2K(Z)dz} \tag{3.7}$$

The diffuse attenuation coefficients K(λ) for E_d(λ) (and L_u(λ)) were calculated from the obtained data in profiles. Mean diffuse attenuation coefficient for Ed(λ) for the Z_{eu} and Z_{pd} (correspond to Z_m) was calculated by Eq. 3.8. Then, biogenic contribution (K_{bio}(λ)) to K(λ) was calculated by subtracting the water contribution K_w(λ) (Eq. 3.9) (the data retrieved from Morel & Maritorena (2001)).

$$K(\lambda)=\frac{1}{Zm}\ln(\frac{Ed(0\text{-},\ \lambda)}{Ed(Zm,\ \lambda)}) \tag{3.8}$$

$$K_{bio}(\lambda)=K(\lambda)-K_w(\lambda) \tag{3.9}$$

The method from Morel (1988) and its reappraising (Morel & Maritorena, 2001), also detailed by Velluci (2007) in Mediterranean scale, related K_{bio}(λ) with [Chl] through a least square fit analysis of power regression (Eq. 3.10) by derivation of two coefficients called as χ(λ) and e(λ).

$$K_{bio}(\lambda)=\chi(\lambda)[Chl]^{e(\lambda)} \tag{3.10}$$

The study considered the bands between 400 and 555 nm. As mentioned in Velluci (2007) and Morel & Maritorena (2001), Kd(λ) at longer wavelengths is flattened by Raman emission and this might be the reason measured of attenuation coefficients being less than expected in case contribution by only water.

CHAPTER FOUR
RESULTS

4.1 Overview of Oceanography of the Ligurian Sea in March 2009

4.1.1 Wind Mixing Event

The cruise was conducted at the end of the winter season, and a warming of the surface layer was observed in the CTD profiles acquired in the first half of the cruise (14^{th} – 19^{th} March 2009). Then, CTD measurements indicated a vertical mixing in the last half of the sampling period (20^{th} – 26^{th} March 2009). The surface water started to become colder due to effect of wind-induced vertical mixing (Figure 4.1). This was confirmed by meteorological data obtained on deck (from11th to 20th of March 2009), NCEP obtained from NOAA (http://www.esrl.noaa.gov/psd/data/gridded/data.ncep.reanalysis.surfaceflux.html) (from 11th to 20th of March 2009) and data from Bastia Weather Station (http://www.tutiempo.net/en/Climate/Bastia/03-2009/77900.htm). Meteorological data sets show good agreement with each other in the period that all have the data (Figure 4.2). As seen in the figure, the 20^{th} of March has the first wind speed peak and a second peak was seen on the 24^{th} of March.

To see the differences, a time section of the stations on each sampling day is presented in Figure 4.1. Temperature profiles get relatively colder and form more straight form through the sampling period. Density profiles indicate denser water column formed by vertical mixing due to wind mixing episodes. Less variation through the vertical section of the profiles result deeper mixing layer in upper part of water column. Parallel to the wind speed variation, increases in mixed layer depth based on density (threshold 0.01) are evident for wind mixing event in the area during the period of the cruise (Figure 4.2).

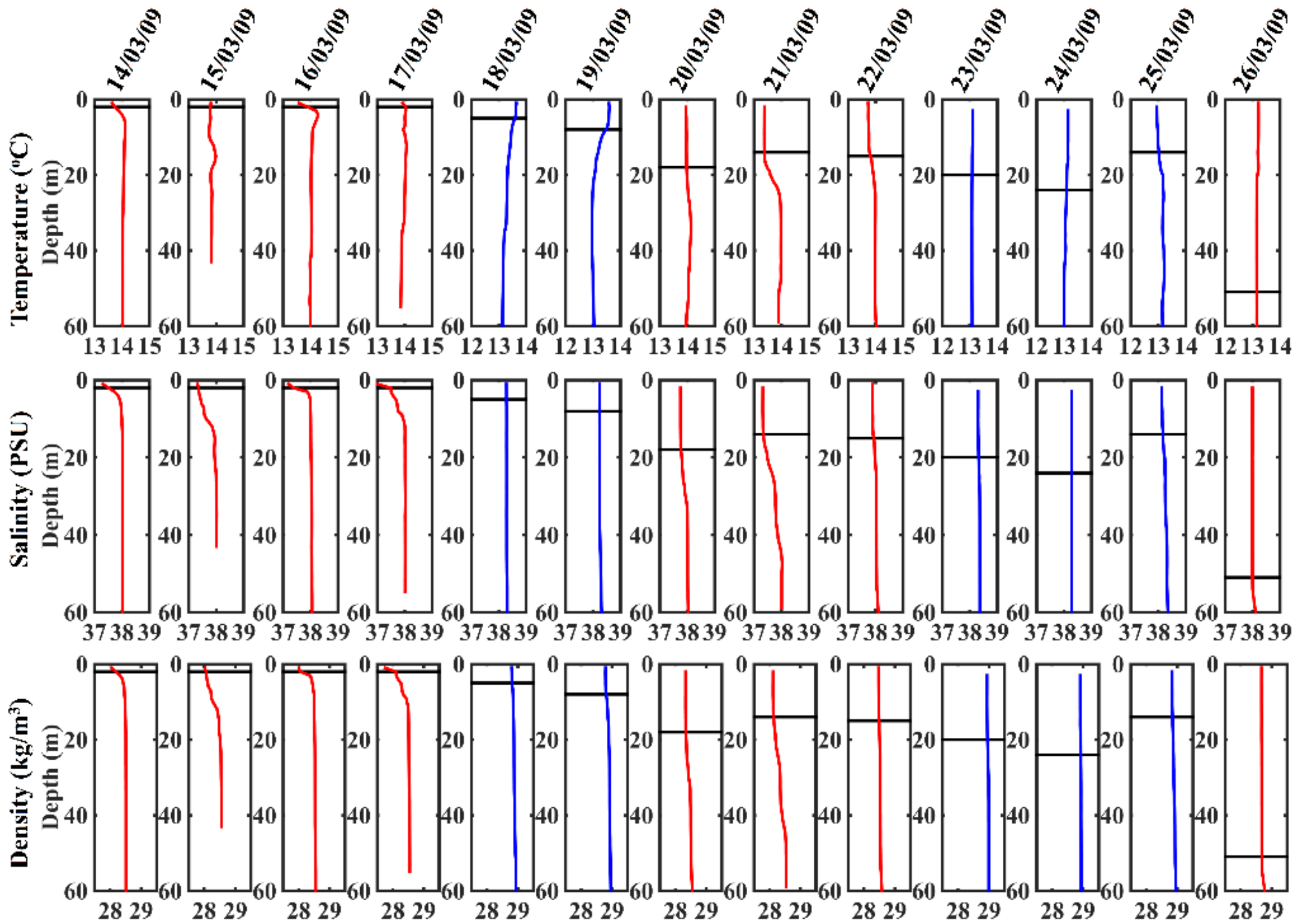

Figure 4.1Profilers of temperature, salinity and density from the selected stations from each sampling day (from the first day to the last) during the cruise period. Blue line indicates off-shore station; red line indicates on-shore station. Horizontal black line shows the mixed layer depth (MLD) on profile (MLD is for density 0.01 threshold).

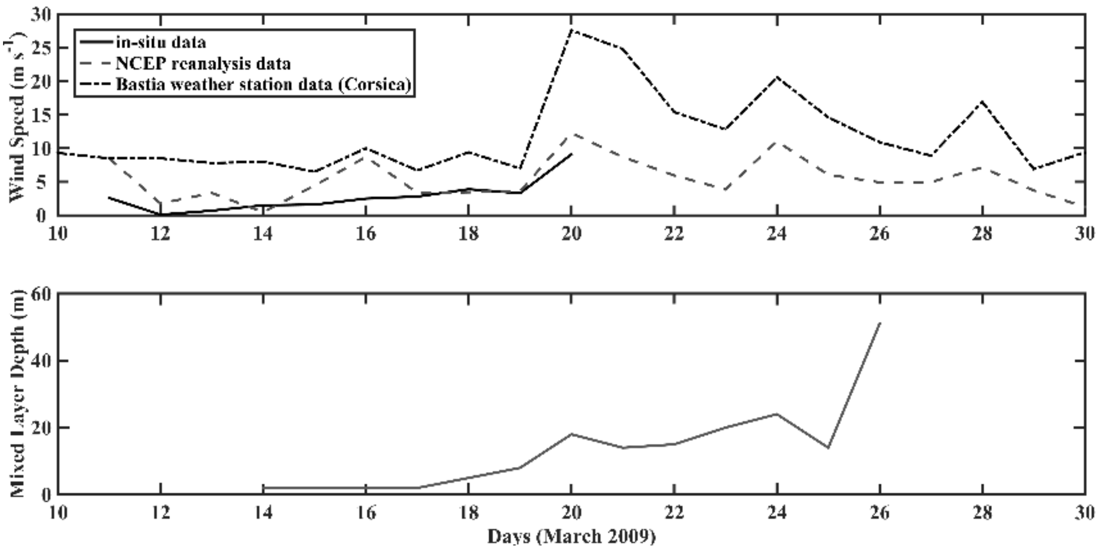

Figure 4.2 Wind speed variation from different data sources during the cruise period (upper panel) and mixed layer depth variation (lower panel) from selected station of each day during the cruise period.

Precipitation data was available for Pisa (Pisa/S. Giusto Weather Station, http://www.tutiempo.net/en/Climate/Pisa_S_Giusto/03-20 09/161580.htm), which is the closest city to the River Arno. There was no big contribution of precipitation during the cruise (Figure 4.3).

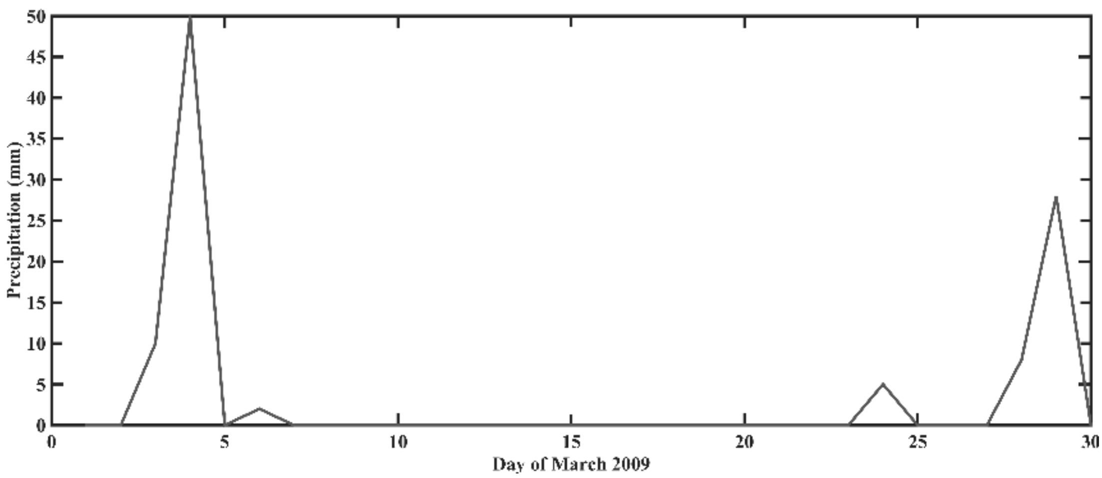

Figure 4.3 Precipitation during March 2009 in Pisa/S. Giusto Weather Station.

4.1.2 Hydrography

Vertical profiles of CTD measurement are grouped into two region groups, as coastal and off-shore, with agreement to common knowledge in the Ligurian Sea. Average values for temperature, salinity and density profiles of the station in both regions are presented in Figure 4.4. Temperature is colder in central (off-shore) region than coastal region. It should be also noted that some stations on coastal also have relatively colder water due to the River Arno discharge. Distinctions in temperature profiles are more evident at depths deeper than 20 meters between the regions. Wind mixing impact on surface can also be seen in average profiles. The average profile before wind mixing are a seasonal thermocline in upper layer, while the average after wind mixing has straight, well-mixed and colder vertical profile form in both shelf and central zones (see dashed and solid lines in Figure 4.4). Salinity and density profiles have also two distinctive characteristics between the regions (Figure 4.4). Higher salinity and density measurements are in central zone (offshore region). Coastal region has varying salinity and density vertical stratification due to impact of the freshwater input of the River Arno, which overlays the dominant Modified Atlantic Water (MAW).

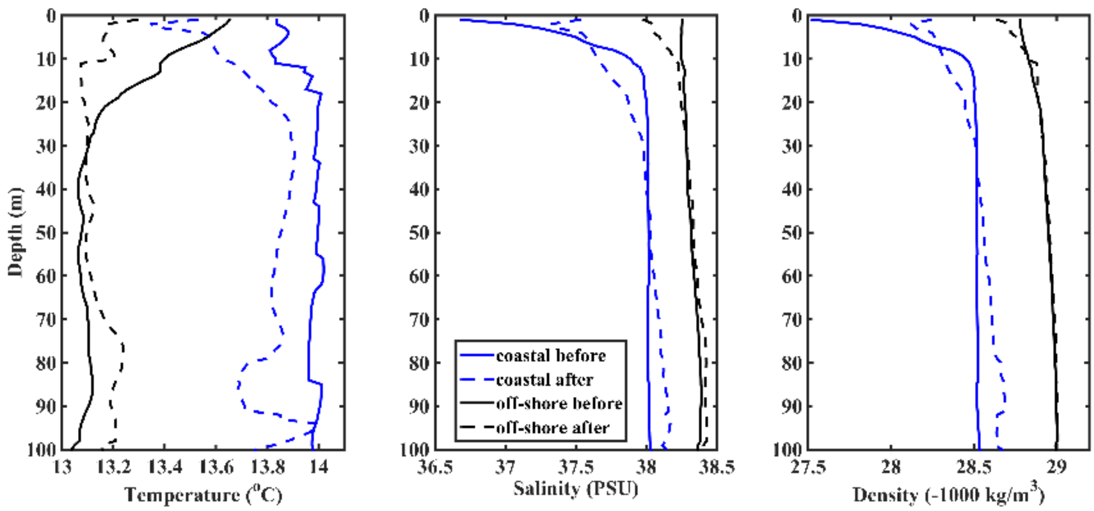

Figure 4.4Averageprofiles of temperature, salinity and density from coastal (blue) and off-shore (black) stations. Solid lines are before mixture (14-19 March 2009) and dashed lines after mixture (20-26 March 2009).

T-S diagram of the profiles measured in the period of the cruise is presented in Figure 4.5. Parallel to the zones in the Ligurian Sea, two main clusters are seen in Figure 4.5. As mentioned by previous studies (Sournia et al., 1990; Picco et al., 2010), stations in the coastal zone have less salty and warmer water and, thus, less dense, while stations in the central zone have saltier and colder, thus, denser water. Stations located in the central zone have values concentrated in the right, lower part of the T-S diagram, with values 13.1 ^{o}C and 38.4 PSU, stations located in the coastal zone have values occupying the remaining part of the T-S diagram, with a major concentration around 13.9 ^{o}C and 38.0 PSU. Three stations are located in a transition zone between onshore and offshore waters and their T-S values connect the two groups. In the central zone MAW and Winter Intermediate Water (WIW) are observed overlying the deeper Levantine Intermediate Water (LIW). Water mass in surface layer shows dispersion in temperature due to occurrence of thermal stratification before wind mixing. Warmer and saltier water at deeper depths indicates LIW. The water mass in the coastal zone derives mainly from MAW. Distribution of upper layer in T-S diagram indicates variations in coastal water due to freshwater inputs as less salty, and horizontal mixing with water of central zone in frontal area. Cold waters observed at surface derive from effects of wind blowing and also of freshwater input of the River Arno. The warmest water was observed in coastal region in the early part of the cruise (before wind mixing episode), while a station sampled on same day had colder than average measurements in the coastal region due to effect of the River Arno. Input of the River Arno is also the reason for large salinity variations in surface layer, causing a dispersion of lower salinity.

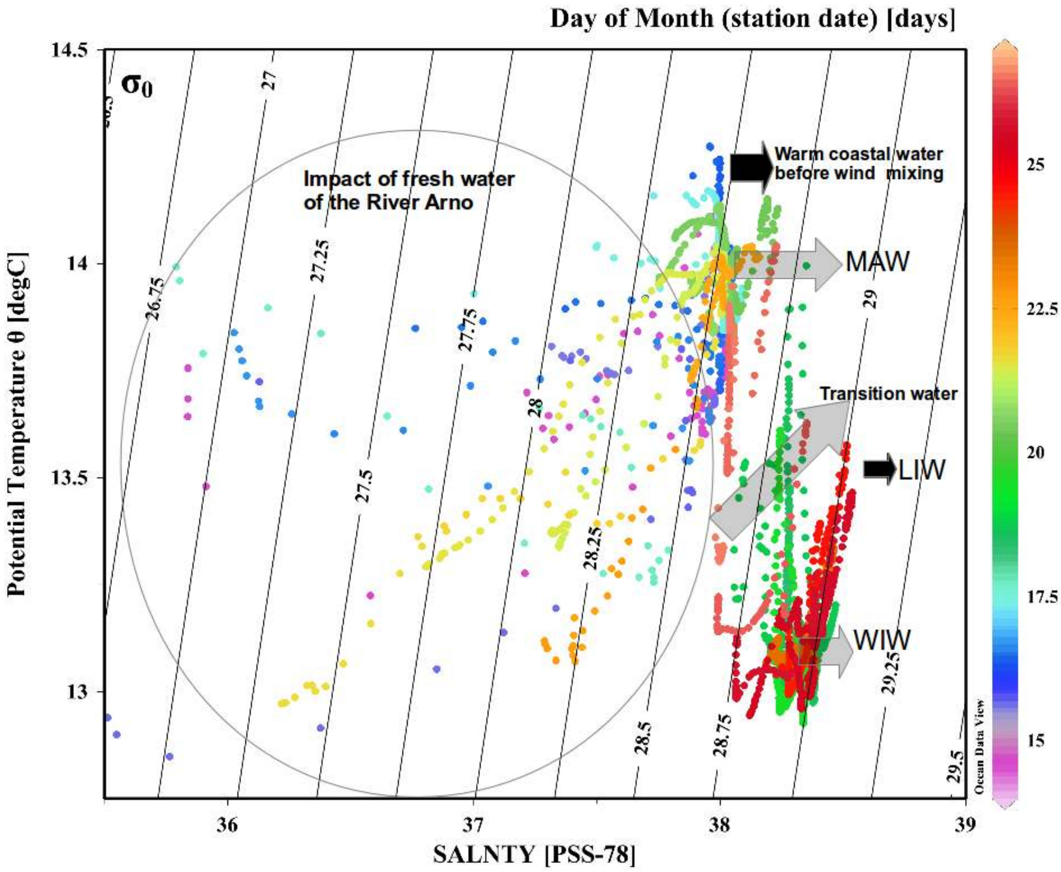

Figure 4.5 T-S Diagram of the stations during the cruise; colors refer to sampling day of cruise.

4.1.3 Remotely Sensed Structures in the Ligurian Sea

As seen in Figure 4.6, spatial distribution of MODIS SST (images on the left) shows colder water in the central zone and warmer water covers peripheral of the central zones remaining parallel to the coast as the known general movement of Ligurian-Provencal circulation (Astraldi et al., 1990; Picco et al., 2010). The impact of fresh water input by the River Arno can be seen in SST images as a colder area along the eastern coast.

Parallel to MODIS SST images, products of MERIS K_d490 (Figure 4.6, on the right) show two distinct zones, as well. Higher MERIS K_d490 values are seen in central zone of Ligurian Sea due to spring bloom stimulated by winter deep convection. Time series of MERIS K_d490 images also indicate the dynamics of spring bloom that is more intense in the beginning of the cruise and shows a decreasing trend towards to the end of the cruise. It is also noted that low values in products of MERIS K_d490 and MODIS SST are observed on the 26th of March in the central zone. High values in product of MERIS K_d490 in a part of the coastal zone, which is near to output of the River Arno, indicates particulate loading in this region. Relatively colder coastal water that is detected from MODIS SST images, increased MERIS K_d 490 values in that part of the eastern Ligurian Sea are another support for impact of freshwater input by rivers. Coastal current region has lower MERIS K_d490 values due to lower production than central zone and to lower particulate input compared to the region with terrestrial input.

Satellite images also show some persistent meso- and sub-meso-scale features such as meanders, eddies, filaments. These meso-scale features are seen during the period of the cruise in the front between the two defined zones. This fact supports having some stations that have transition profile features, between zones.

The effects of the wind-mixing event are also observed in MODIS SST images. As seen in Figure 4.6, MODIS SST distribution before the wind mixing event show wider and warmer surface water in the area, while MODIS SST distribution after the event are narrower and relatively colder in both zones.

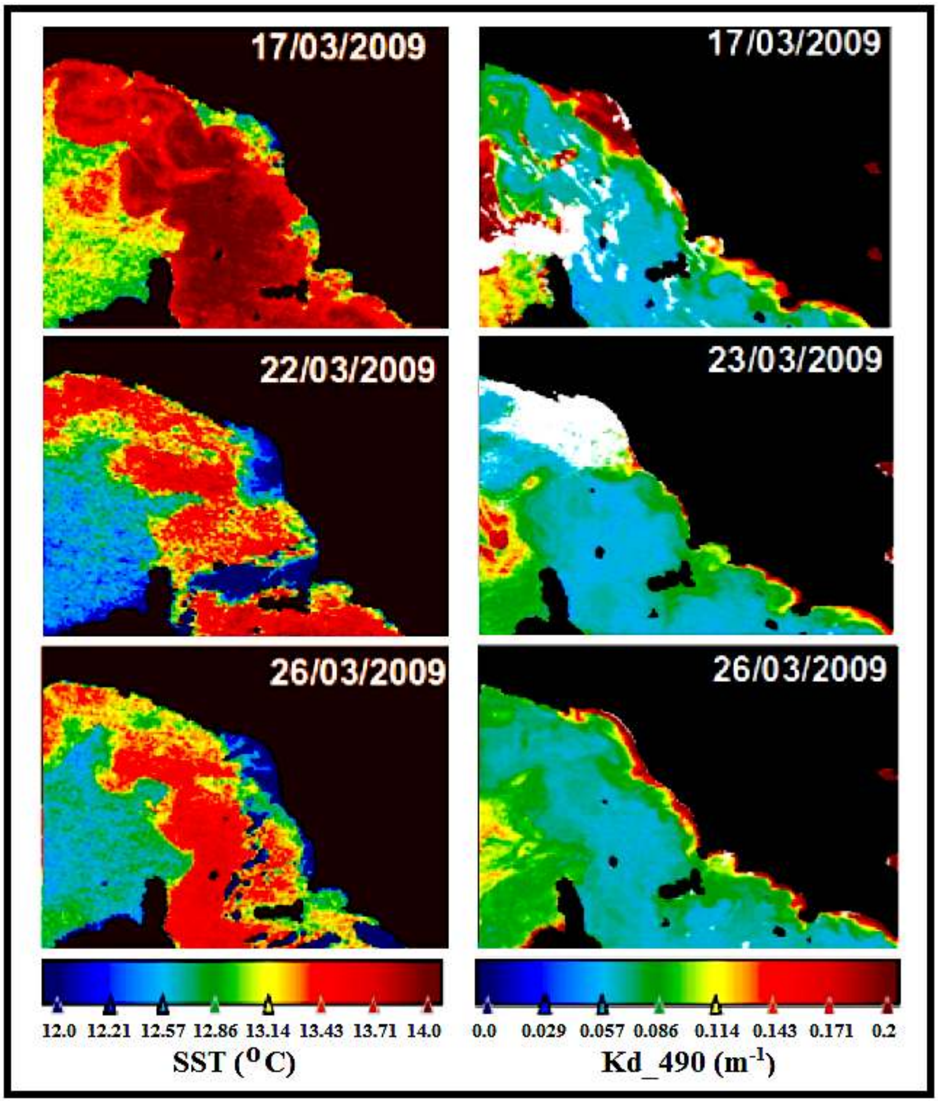

Figure 4.6 SST products from MODIS Aqua (left) and K_d 490 products from Meris (right) in cloud free days of the cruise.

4.2 Optical Description of the Ligurian Sea

4.2.1 Inherent Optical Properties

4.2.1.1 Bio-optical Properties and Bio-optical Water Types

Optical depth calculations from E_d (PAR) measurement meters were used to evaluate distribution of IOPs in first optical depth in the study area. IOP measurements of each depth within first optical depth are taken to calculate average values for this depth. Calculated average values in first optical depth were used for the analysis. The highest value in spectrum was at 412 nm, while the lowest value was in 715 nm for absorption. Other variables show relatively uniform distribution in spectrum. Measurements of the IOPs averaged of all the stations at first optical depth are given in Table 4.1. Figure 4.7 shows the spectrum of total absorption coefficient, scattering coefficient, attenuation coefficient and particulate backscattering coefficient of the stations. Ranges of the IOPs show similar variation with previous study (Velluci, 2007) in Mediterranean Sea.

There is no distinctive separation between the spectral trends and data distribution in different stations in both region. Stations, which are the closest to the shallow onshore region, can be distinguished with extreme values in spectrum of all variables in Figure 4.7. Figure 4.8 shows that stations with high values have spatial relationship with each other. Particles that are carried into the sea by the River Arno or re-suspension, might be the reason for these extremely high values at the blue region of the spectrum (Figure 4.7 and Figure 4.8) stations closest to land. Second peak of the regions (at 676 nm) for Chlorophyll in absorption spectrum of these stations have weak slope in these measurements compared to blue region, thus these spectral patterns indicate the different communities of the particle populations. Other high values with weakest peaks at 676 nm are also located near coastal with relation to the impact zone of the terrestrial input or sediment suspension, especially with high backscattering coefficient values (Figure 4.8).

Table 4.1 IOPs distribution in first optical depth in the stations.

Wavelengths nm	**absorption m^{-1}**		**scattering m^{-1}**		**attenuation m^{-1}**		**backscattering m^{-1}**	
	mean	**std**	**mean**	**std**	**mean**	**std**	**mean**	**std**
412	0.11	0.06	0.50	0.29	0.61	0.35	0.007	0.006
440	0.09	0.05	0.49	0.28	0.58	0.33	0.006	0.005
488	0.06	0.03	0.48	0.28	0.54	0.32	0.007	0.005
510	0.04	0.03	0.49	0.29	0.53	0.31	0.007	0.005
532	0.03	0.02	0.48	0.29	0.51	0.31	0.006	0.005
555	0.02	0.01	0.48	0.29	0.50	0.30	0.006	0.005
650	0.01	0.01	0.44	0.28	0.45	0.28	0.006	0.005
676	0.03	0.02	0.41	0.26	0.44	0.28	0.005	0.004
715	0.00	0.00	0.43	0.27	0.43	0.27	0.005	0.004

On the other hand, Figure 4.8 also shows that the inner part of the central zone of the Ligurian Sea has higher values than average distribution of the IOPs measurements due to spring bloom.

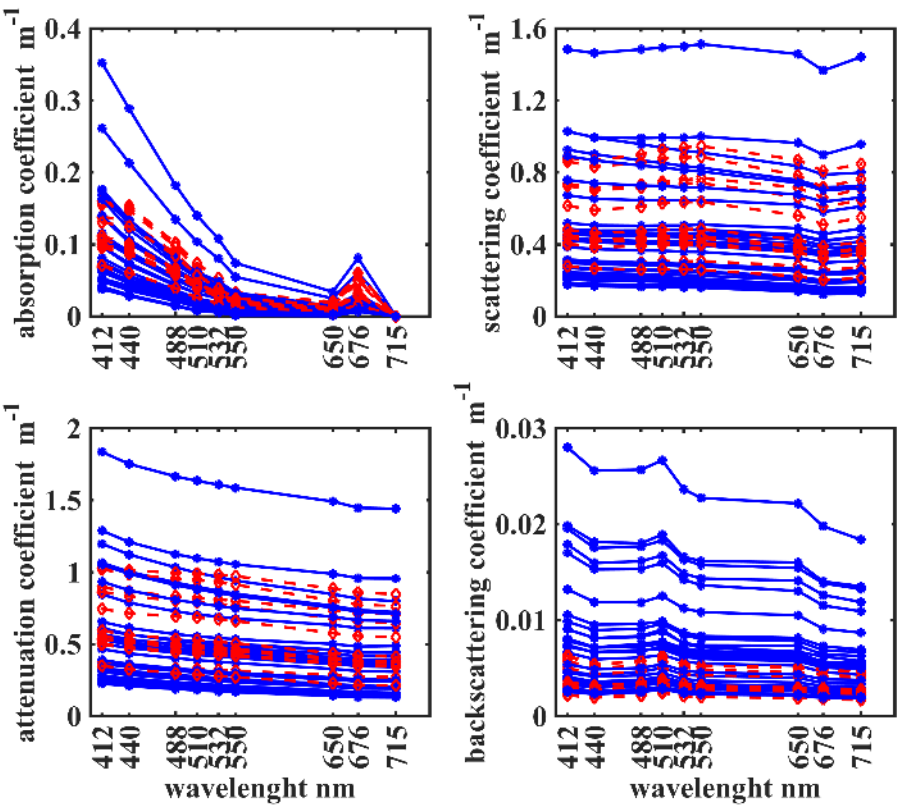

Figure 4.7 Spectrums of total absorption coefficient (left-top), scattering coefficient (right-top), attenuation coefficient (left-bottom) (from AC-9) and particulate backscattering coefficient (right-bottom) (from ECO BB-9) of stations.

Availability of the measurements in same wavelengths in spectral instruments AC-9 and ECO BB-9 makes it possible to use the measurements together. Since different particle types have different IOPs, using the measurements together can help to define different optical water types in the study area.

Absorption and particulate backscattering at 676 nm in spectrum has a special indication due to characteristics of the phytoplankton. Figure 4.9 shows the data frequency at the ratio of particulate backscattering to absorption at 676 nm. The data are divided into two clusters as low and high ratio clusters. Some data points in the

Figure 4.9 shows very high ratio value due to re-suspension or fresh water input with terrestrial particles.

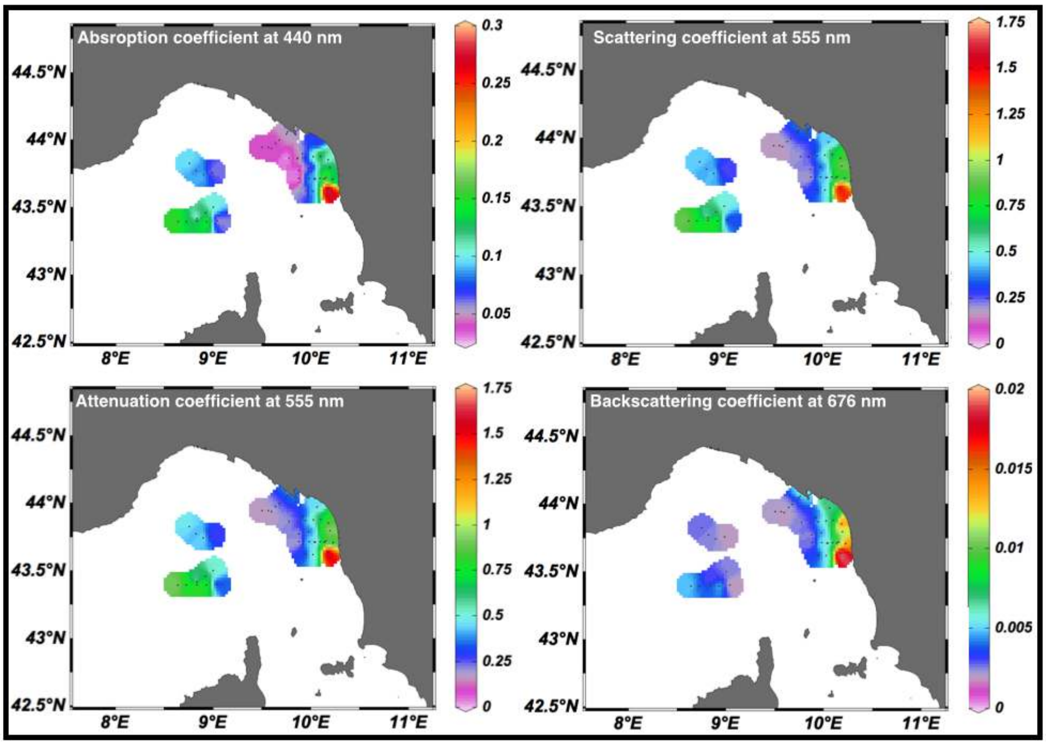

Figure 4.8 Spatial distribution of total absorption coefficient at 440 nm (left-top), scattering coefficient at 550 nm (right-top), attenuation coefficient at 550 nm (left-bottom) and particulate backscattering coefficient at 676 nm (right-bottom) of stations in first optical depth. Units are m^{-1}.

To parameterize the clusters, 0.9 quantile of the data were calculated and the data within this interval was used to remove the skewness in the histogram due to extreme effect of terrestrial inputs. Since data clusters do not have the same data points to calculate the separation coefficient between clusters, the average values of the clusters were calculated and these values were used to find separation coefficients. The average values of the clusters are 0.085 for low ratio cluster and 0.264 for high ratio cluster (Figure 4.9). Data distributions at first optical depth of the clusters are presented in Table 4.2. The separation coefficient between two clusters and the value of the 90% quantile of the dataset are 0.175 and 0.425, respectively.

The value of the 90% quantile might also indicate the separation between re-suspension or terrestrial particulate and phytoplankton dominated optical water type in the region, when taking into account spatial distribution of the stations (Figure 4.10). Geographical distribution of the stations show that clusters locate in different regions parallel to hydrography of the region (Figure 4.10). While cluster 1 is located in central zone of the Ligurian Sea, cluster 2 is located in the coastal zone of the Ligurian Sea. Higher ratios that are outside of the values of 0.9 quantile are located parallel to coastline, which also indicates the local impacts of the re-suspension in shallow depths and fresh water inputs.

Table 4.2 IOPs distribution in first optical depth in the stations.

Variable	Cluster	Parameter	Wavelength nm							
			412	440	488	510	532	555	650	676
absorption m^{-1}	**2**	**mean**	0.106	0.082	0.050	0.036	0.028	0.018	0.008	0.020
		std	0.074	0.061	0.039	0.031	0.024	0.017	0.008	0.017
	1	**mean**	0.116	0.107	0.071	0.048	0.033	0.021	0.013	0.038
		std	0.032	0.034	0.023	0.016	0.011	0.007	0.005	0.015
scattering m^{-1}	**2**	**mean**	0.451	0.439	0.433	0.433	0.428	0.429	0.398	0.369
		std	0.315	0.309	0.310	0.311	0.312	0.315	0.307	0.290
	1	**mean**	0.548	0.529	0.540	0.554	0.558	0.560	0.501	0.458
		std	0.209	0.206	0.215	0.222	0.226	0.229	0.211	0.197
backscattering m^{-1}	**2**	**mean**	0.008	0.007	0.007	0.007	0.007	0.006	0.006	0.005
		std	0.006	0.005	0.005	0.006	0.005	0.005	0.005	0.004
	1	**mean**	0.004	0.003	0.004	0.004	0.004	0.003	0.003	0.003
		std	0.002	0.001	0.001	0.001	0.001	0.001	0.001	0.001
bbp/abs	**2**	**mean**	0.070	0.083	0.147	0.234	0.266	0.629	1.072	0.264
		std	0.012	0.016	0.036	0.084	0.095	0.734	1.094	0.047
	1	**mean**	0.032	0.031	0.052	0.085	0.106	0.160	0.261	0.085
		std	0.005	0.004	0.007	0.013	0.015	0.031	0.053	0.014
bbp/b	**2**	**mean**	0.016	0.015	0.016	0.017	0.015	0.014	0.015	0.015
		std	0.002	0.001	0.001	0.001	0.001	0.001	0.001	0.001
	1	**mean**	0.007	0.006	0.007	0.008	0.006	0.006	0.007	0.007
		std	0.001	0.001	0.001	0.001	0.001	0.001	0.001	0.001

Figure 4.11 shows the relation between abs and b_{bp} at 676 nm with the separation coefficient and 0.9 quantile value of the data set. As seen in Figure 4.11, the coefficient separates distinctively the clusters each cluster. It also indicates the significant relationship between abs and b_{bp} at 676 nm. Cluster 1 shows lower b_{bp} coefficients with high absorption coefficients trend (R=0.96) while Cluster 2 shows higher b_{bp} coefficient with high absorption coefficients trend (R=0.96). High absorption trends at 676 nm in both clusters indicate existence of phytoplankton communities in these clusters but there are no clues about different communities with

a similar absorption range. On the other hand, the value group outside of 0.9-quantile has a trend with higher b_{bp} and lower absorption. This fact also supports extremely dominated mineral and/or detritus particle community for the group, but limited number of stations for this group does not allow detailed analysis.

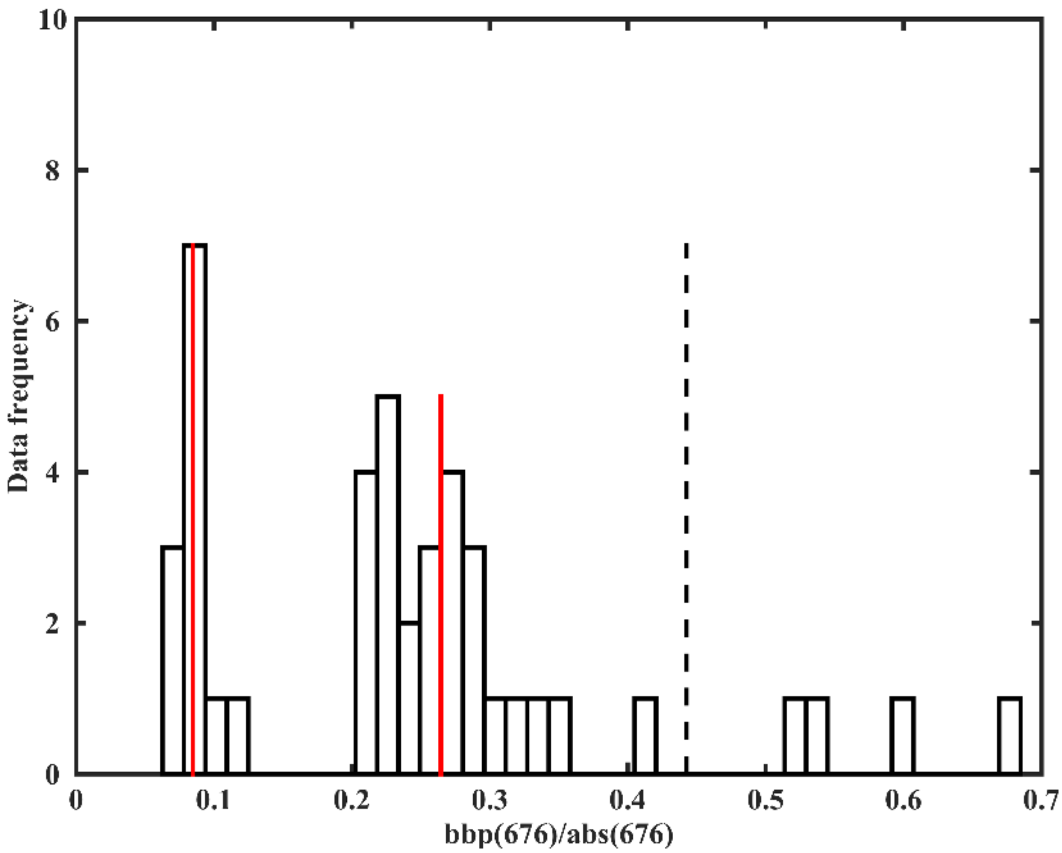

Figure 4.9 Data frequency histogram of the ratio of b_{bp} to absorption at 676 nm. The lines show the average values of the data clusters. Black dashed line shows 0.9 quantile of the dataset.

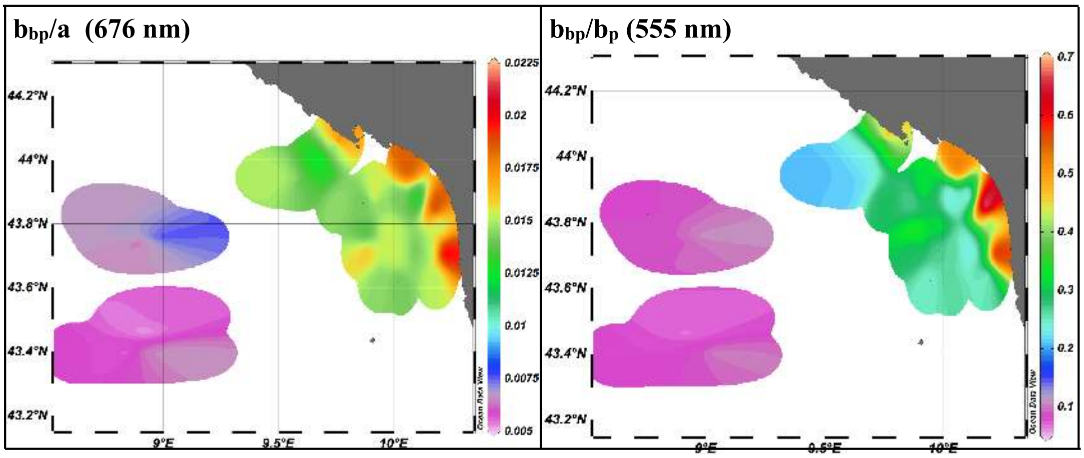

Figure 4.10 Station distributions based on clusters of $b_{bp}(676)$/abs(676)(left) and distribution of the ratio of $b_{bp}(555)/b_p(555)$ based on same clusters (right).

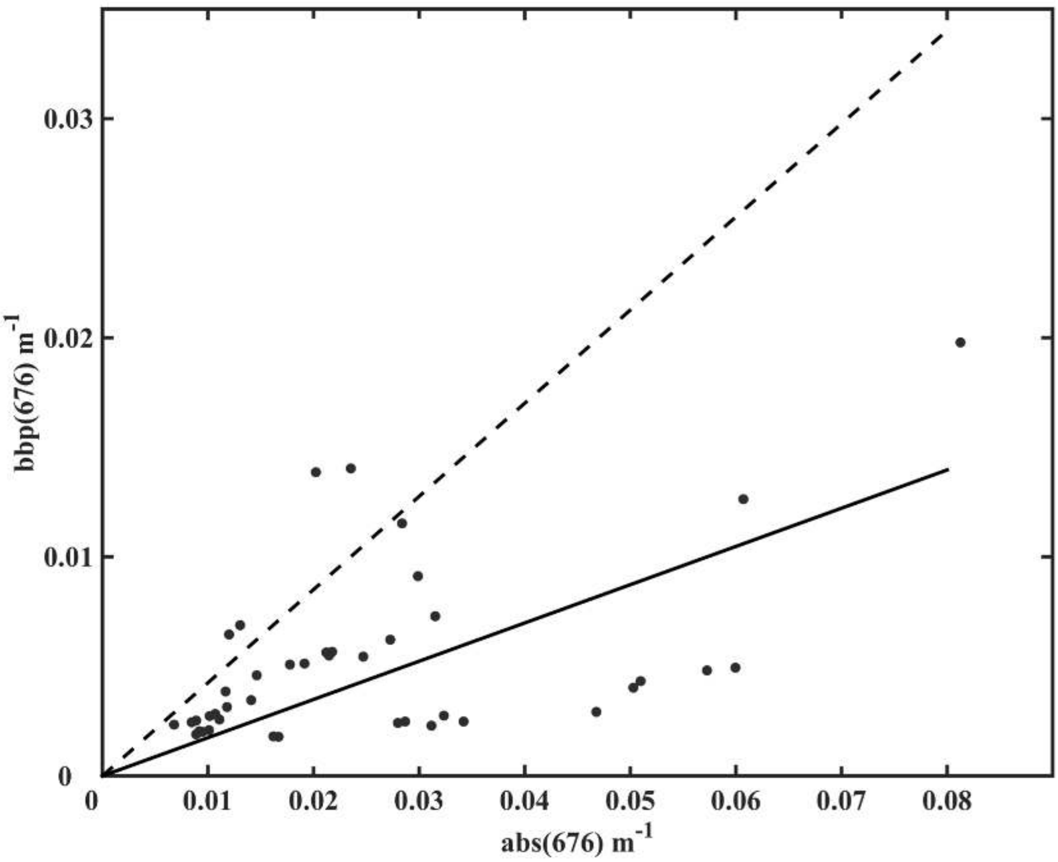

Figure 4.11 Relationship between absorption and b_{bp} at 676 nm. Solid line shows separation line (0.175) and dashed line shows the 0.9 quantile value (0.425) of the dataset.

4.2.2 Apparent Optical Properties

4.2.2.1 $K_{bio}(\lambda)$ from [Chl] Concentration

Mean weighted Chl concentrations [Chl] and biogenic contribution to diffuse attenuation coefficient ($K_{bio}(\lambda)$) were used to estimate empirically their relationships in euphotic depth and first optical depth. The results for the coefficients are reported in Table 4.3 for both euphotic depth and first optical depth. Regression coefficients for comparison at the wavelengths show a significant relationship. The regression coefficients are higher in euphotic depth than first optical depth. It is also noted that the regression coefficients have decreasing trend from blue region to green region. Statistical analyses were not applied for wavelengths longer than 555, because $K_d(\lambda)$ at longer wavelengths is flattened by Raman emission and this might be the reason of measured attenuation coefficients being less than expected in case contribution by only water.

Some empirical approaches were developed and improved to estimate depth of euphotic zone from chlorophyll as most measured variable. Cumulated Chl concentration (in euphotic zone) versus euphotic depth is shown in Figure 4.12. This iterative scheme is defined for shallower Z_{eu} than 102 meters as Eq. 4.1 by Morel & Berthon (1989) for all oceanic Case 1 waters and it is revised in Morel & Maritorena (2001) (Eq. 4.2). This relation was also localized for Mediterranean by Collela (2006) (Eq. 4.3). Results given by Morel & Berthon (1989)'s coefficients have better estimation than revised version of Morel & Maritorena (2001) and Collela (2006)'s modification in Mediterranean Sea (Figure 4.12).

Morel & Berthon (1986) also related mean weighted Chl concentration in first optical depth with cumulated chlorophyll in euphotic zone (Eq. 4.4). Relationship between [Chl] and euphotic depth, and relationship between [Chl] and diffuse attenuation coefficient for PAR in Euphotic depth ($K_{PAR}(Z_{eu})$), as seen in Eq. 4.5 and Eq. 4.6, respectively, are defined by Morel (1988). The results show similar relations with literature seen in Case1 waters of the Ligurian Sea (Figure 4.13, 4.14 and 4.15).

Table 4.3 Regional coefficients of matched K_{bio} and [Chl] as results of the least square fit analyses.

	Euphotic zone			First optical depth		
Wavelenght	**e(λ)**	**χ(λ)**	**R^2**	**e(λ)**	**χ(λ)**	**R^2**
400	0.45706	0.11931	0.94	0.52368	0.11491	0.70
405	0.47573	0.11973	0.95	0.54653	0.11572	0.72
410	0.50039	0.11947	0.95	0.57429	0.11583	0.74
415	0.52192	0.11838	0.95	0.59853	0.11509	0.75
420	0.54211	0.11608	0.96	0.62222	0.11308	0.76
425	0.56256	0.11356	0.96	0.64727	0.11085	0.77
430	0.58557	0.11166	0.96	0.67334	0.10928	0.77
435	0.60647	0.10979	0.96	0.69908	0.10779	0.78
440	0.62231	0.10613	0.96	0.71850	0.10436	0.78
445	0.62956	0.10152	0.96	0.73294	0.09967	0.77
450	0.63785	0.09636	0.96	0.74762	0.09444	0.75
455	0.64459	0.09317	0.96	0.75524	0.09132	0.75
460	0.65446	0.09103	0.96	0.76982	0.08926	0.75
465	0.66351	0.08902	0.96	0.78286	0.08731	0.74
470	0.66559	0.08653	0.96	0.79072	0.08469	0.74
475	0.66196	0.08347	0.95	0.79072	0.08146	0.73
480	0.65707	0.07986	0.95	0.78869	0.07767	0.71
485	0.64696	0.07708	0.95	0.78028	0.07472	0.70
490	0.63594	0.07445	0.95	0.77026	0.07206	0.68
495	0.62798	0.07144	0.95	0.76767	0.06895	0.66
500	0.61976	0.06803	0.95	0.76572	0.06532	0.64
505	0.61869	0.06337	0.94	0.77853	0.06015	0.61
510	0.61637	0.05911	0.93	0.79058	0.05513	0.57
515	0.61033	0.05497	0.92	0.80328	0.04992	0.53
520	0.57087	0.05458	0.91	0.76102	0.04881	0.49
525	0.54485	0.05364	0.91	0.72439	0.04755	0.46
530	0.52834	0.05220	0.90	0.70791	0.04570	0.43
535	0.50851	0.05143	0.89	0.68071	0.04463	0.40
540	0.48779	0.05101	0.89	0.65195	0.04398	0.37
545	0.47065	0.04999	0.88	0.62386	0.04264	0.34
550	0.46346	0.04778	0.87	0.62645	0.03986	0.31
555	0.43655	0.04721	0.84	0.59062	0.03894	0.27

$$Z_{eu}=568.2Chl_{tot}^{-0.746} \quad (4.1)$$

$$Z_{eu}=912.5Chl_{tot}^{-0.839} \quad (4.2)$$

$$Z_{eu}=199.85Chl_{tot}^{-0.435} \quad (4.3)$$

$$[Chl]_{tot}=40.6C_m^{0.459} \quad (4.4)$$

$$Z_{eu}=38[Chl]^{-0.428} \quad (4.5)$$

$$Kd_{PAR}=0.121[Chl]^{0.428} \quad (4.6)$$

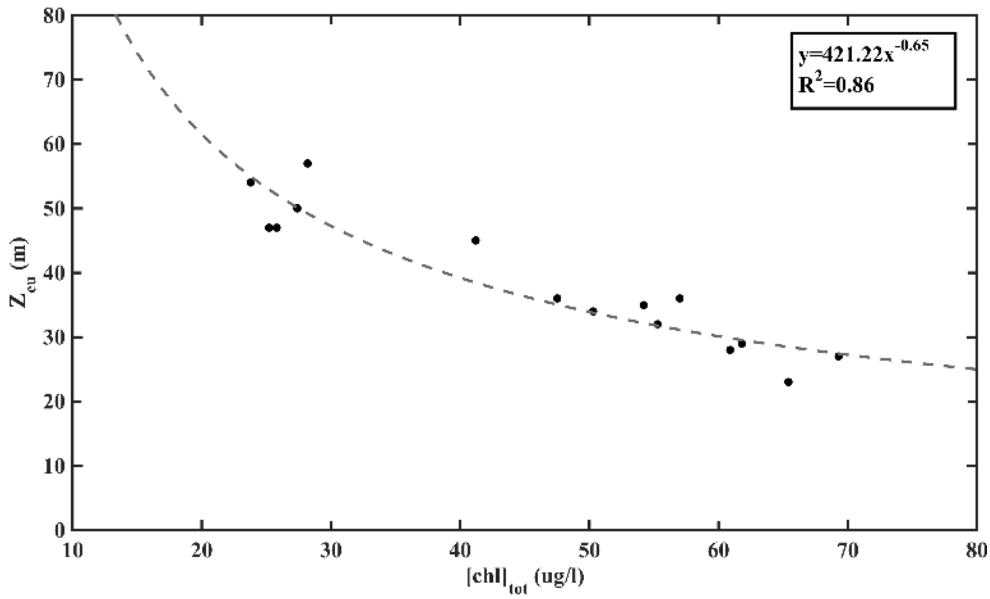

Figure 4.12 Relation between euphotic depth and cumulated Chl profile in Case 1 waters of Ligurian Sea.

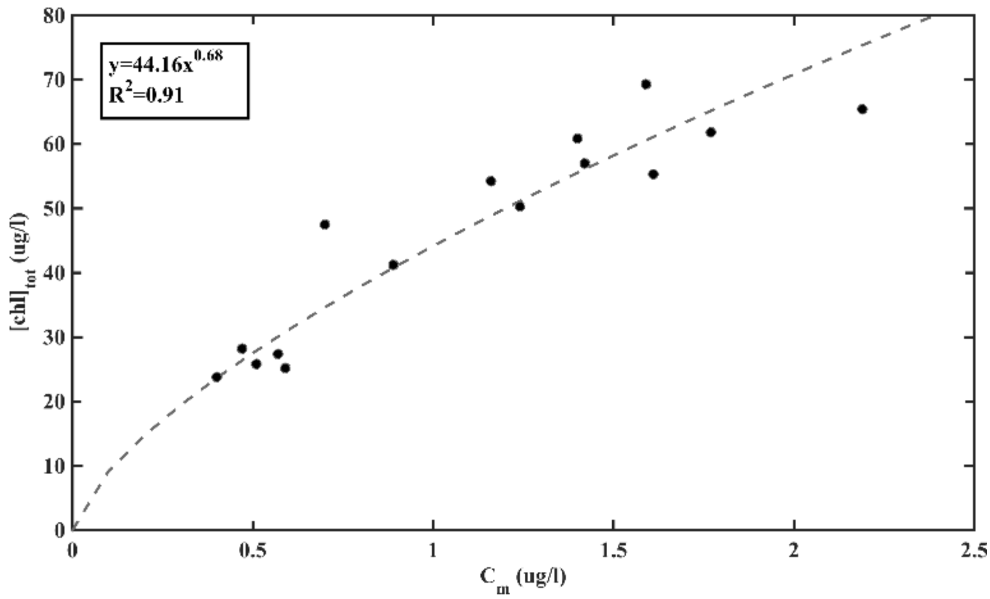

Figure 4.13 Relation between cumulated Chl profile in euphotic depth and mean weighted Chl concentration in first optical depth in Case 1 waters of Ligurian Sea.

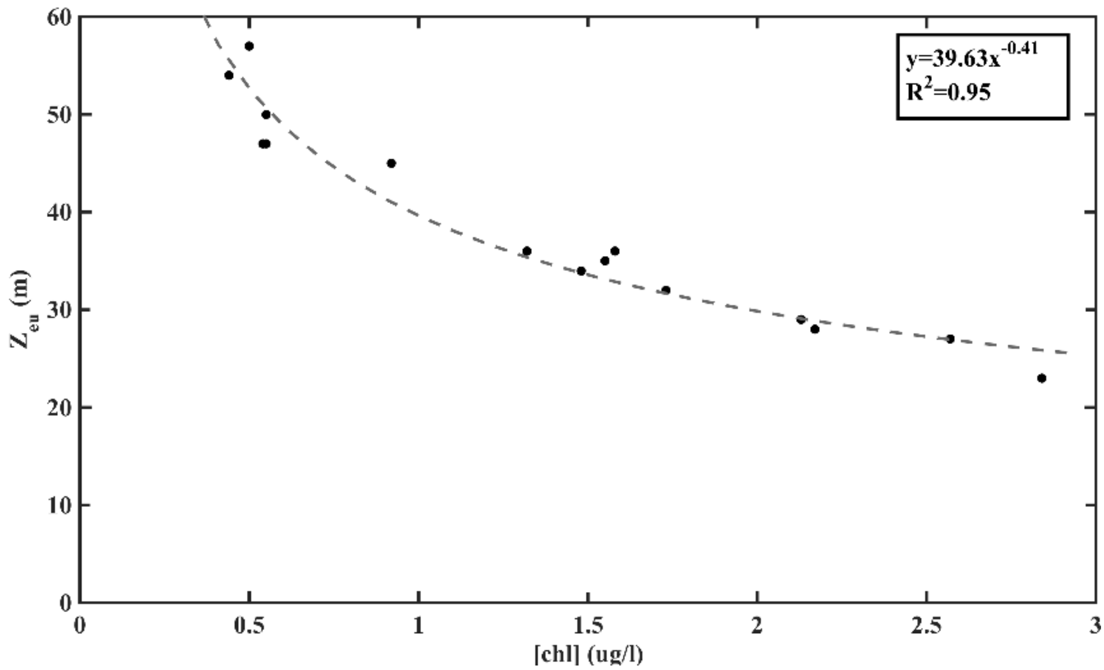

Figure 4.14 Relation between mean concentration of cumulated Chl profile in euphotic depth and euphotic depth in Case 1 waters of Ligurian Sea.

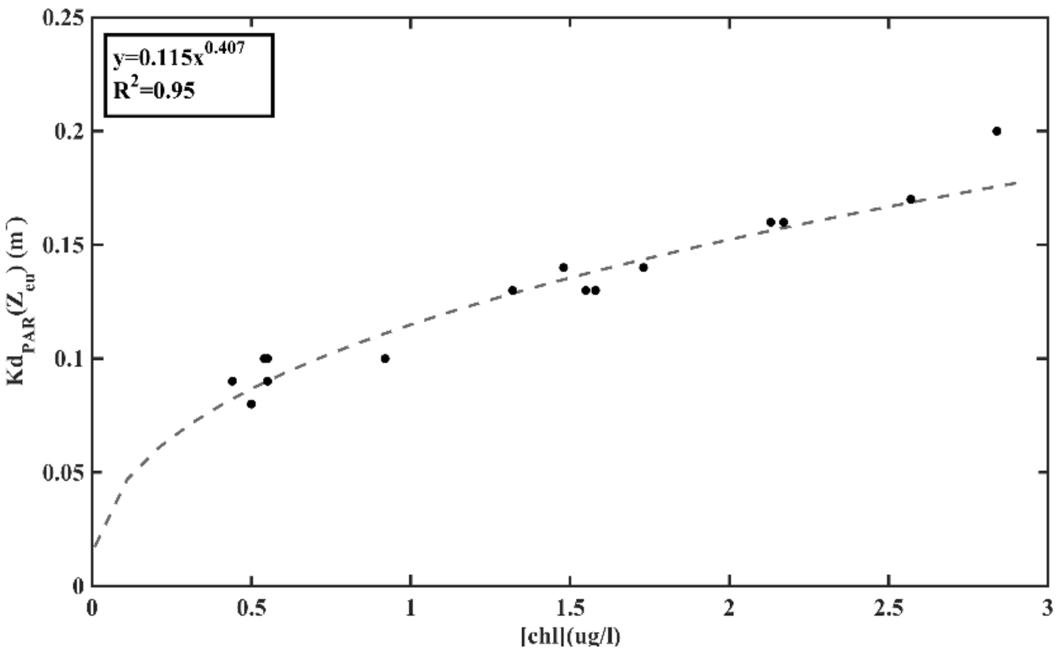

Figure 4.15 Relationship between mean concentration of cumulated Chl profile in euphotic depth and Kd_{PAR}in euphotic depth in Case 1 waters of Ligurian Sea.

4.3 Validation of the Data-sets for Radiative Transfer Modeling

To validate the outputs of the radiance fields derived from the measured IOPs, which were used for evaluation of the output of the bio-optical model, retrieved Ed and Lu from Ecolight simulations of measured IOPs and *in-situ* Ed and Lu measurements were compared (N= 452) in 8 wavelengths between 400 nm and 700 nm with selected statistical comparisons (Table 4.4). Descriptive statistical parameter of the datasets that were obtained from the model show similar values with *in-situ* measurements. The parameters for estimated dataset are given together with *in-situ* dataset in Table 4.5.

Table 4.4 Statistical results for comparison of the radiance field datasets between in-situ and derived from IOPs.

Statistics	Wavelengths (nm)							
	412	**440**	**488**	**510**	**532**	**555**	**650**	**676**
	Ed (in-situ vs. IOPs derived)							
Minimum error	-0.2132	-0.2030	-0.1956	-0.1873	-0.1637	-0.1462	-0.1058	-0.1346
Maximum error	0.0930	0.1306	0.2039	0.1952	0.2081	0.2147	0.1433	0.0934
Mean error	-0.0492	-0.0484	-0.0469	-0.0512	-0.0413	-0.0262	-0.0131	-0.0180
Root mean square error	0.0626	0.0640	0.0672	0.0693	0.0605	0.0482	0.0295	0.0324
Linear correlation (r)	0.98	0.98	0.98	0.98	0.98	0.99	0.98	0.98
Slope (in-situ/modeled)	1.1	1.1	1.1	1.1	1.1	1.0	1.0	1.1
R^2	0.96	0.97	0.96	0.96	0.97	0.97	0.97	0.95
	Lu (in-situ vs. IOPs derived)							
Minimum error	-0.0023	-0.0032	-0.0042	-0.0038	-0.0042	-0.0036	-0.0008	-0.0010
Maximum error	0.0002	0.0003	0.0012	0.0014	0.0007	0.0010	0.0006	0.0000
Mean error	-0.0006	-0.0008	-0.0007	-0.0005	-0.0006	-0.0003	0.0000	-0.0002
Root mean square error	0.0008	0.0010	0.0011	0.0008	0.0010	0.0007	0.0001	0.0002
Linear correlation (r)	0.98	0.98	0.96	0.96	0.96	0.97	0.96	0.87
Slope (in-situ/modeled)	1.3	13	1.1	1.1	1.2	1.1	1.1	1.9
R^2	0.96	0.96	0.93	0.93	0.93	0.94	0.92	0.76

Table 4.5 Descriptive statistical parameters for radiance field in both data-set, in-situ and derived from IOPs.

Parameter	Wavelengths (nm)							
	412	**440**	**488**	**510**	**532**	**555**	**650**	**676**
	***in-situ* Ed**							
Mean	0.299	0.362	0.475	0.470	0.463	0.433	0.126	0.096
Std	0.208	0.234	0.266	0.259	0.253	0.242	0.150	0.131
Max.	0.834	0.937	1.098	1.097	1.089	1.054	0.646	0.586
Min.	0.002	0.004	0.015	0.024	0.032	0.024	0.000	0.000
	IOPs derived Ed							
Mean	0.249	0.314	0.428	0.419	0.422	0.407	0.113	0.078
Std	0.195	0.223	0.263	0.255	0.253	0.246	0.150	0.124
Max.	0.837	0.944	1.095	1.065	1.066	1.041	0.662	0.561
Min.	0.000	0.001	0.008	0.011	0.019	0.023	0.000	0.000
	***in-situ* Lu**							
Mean	0.0025	0.0032	0.0050	0.0045	0.0041	0.0034	0.0002	0.0002
Std	0.0018	0.0022	0.0030	0.0026	0.0024	0.0022	0.0003	0.0003
Max.	0.0082	0.0107	0.0142	0.0122	0.0126	0.0133	0.0027	0.0019
Min.	1.60E-05	1.61E-05	6.90E-05	1.18E-04	1.62E-04	1.57E-04	2.69E-06	4.47E-06
	IOPs derived Lu							
Mean	0.0019	0.0025	0.0043	0.0040	0.0034	0.0030	0.0002	0.0001
Std	0.0015	0.0018	0.0027	0.0023	0.0020	0.0018	0.0003	0.0001
Max.	0.0074	0.0094	0.0139	0.0128	0.0109	0.0099	0.0032	0.0014
Min.	5.81E-06	1.14E-05	6.10E-05	1.13E-04	1.47E-04	1.64E-04	8.39E-07	6.07E-07

Significant correlations were observed between results from derived radiance fields and *in-situ* radiance fields in each variable at all wavelengths. Comparisons of Ed and Lu show similar correlation coefficients, however Ed has slightly better correlation coefficients than Lu. The highest correlation, 0.99, was observed in Eds comparison at 555 nm, while the lowest correlation, 0.76 which is the only correlation coefficients less than 0.96 among all comparisons, was observed in Lus comparison at 676 nm. Mean errors of the outputs of the model were very low for each variable; however, range of the errors show there were no biases in estimation. When comparing the mean of the data set and the error, the lowest mean error was observed at 555 nm in Ed and Lu, while the highest mean error was observed at 412 nm for both, Ed and Lu. Wavelengths comparisons of the radiance fields are presented in Figure 4.16 for Ed and Figure 4.17 for Lu.

A simple regression was forced through zero between estimated values and *in-situ* data to evaluate ratio of modeled and *in-situ* values. Significant regression coefficients were observed for all comparisons. Ratios between modeled and *in-situ* values were around 1 with a range between 1.0 and 1.9. The ratios in Ed were extremely close to 1 (between 1.0 and 1.1) with pretty high regression coefficients from 0.95 to 0.97. The ratios in Lu generally were around 1 with small deviation in blue region and relatively higher deviation at 676 nm. This relatively high deviation and relatively less significant correlation and regression coefficients might be the result of inelastic scattering addition to Raman scattering. Another fact is having deviation at deeper depths.

Results of the validation of IOPs data as representative of the radiance fields showed that dataset of IOPs can be used for further purposes such as developing a model and validation of the model.

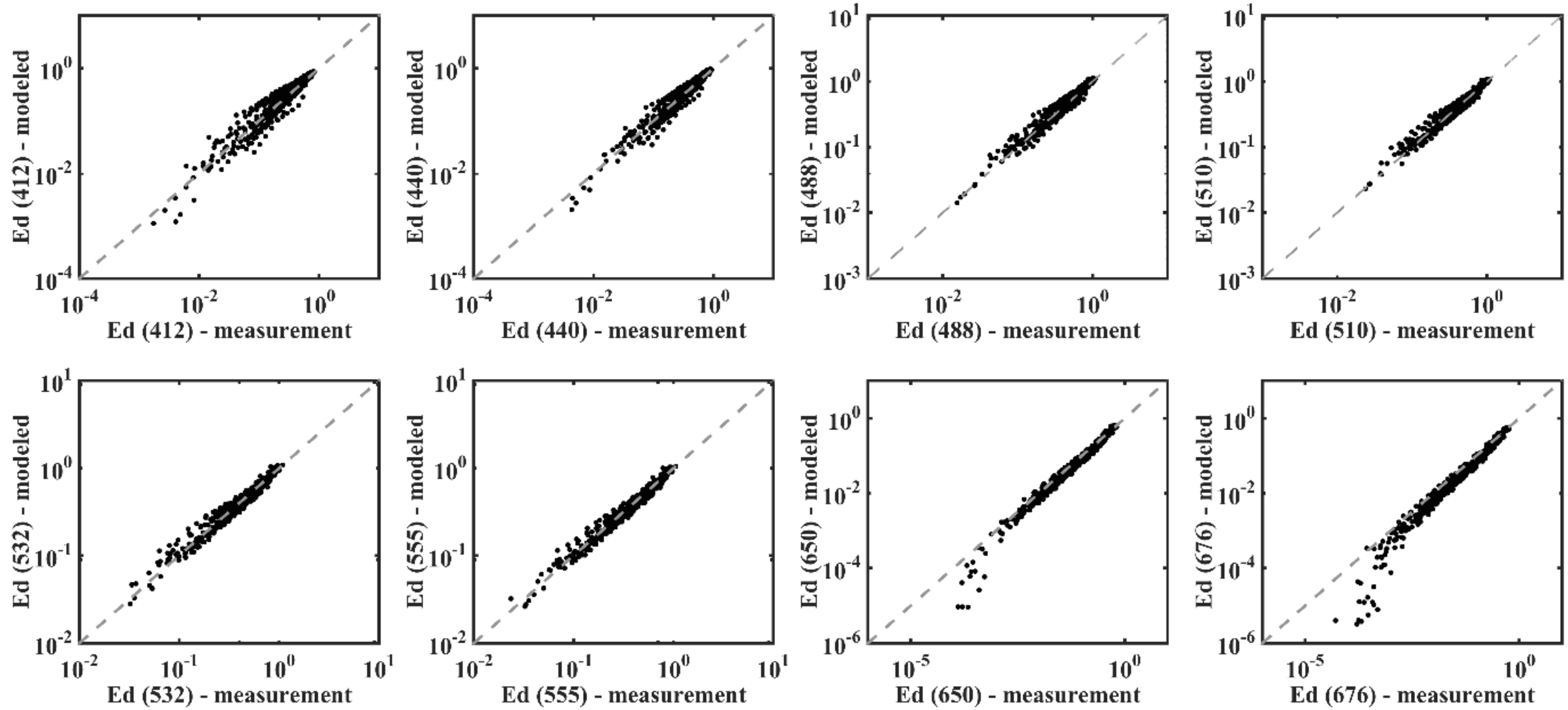

Figure 4.16 Comparison of *in-situ* downward irradiance and downward irradiance derived from IOPs' measurements at each measured wavelengths (nm). Dashed line shows 1:1 ratio.

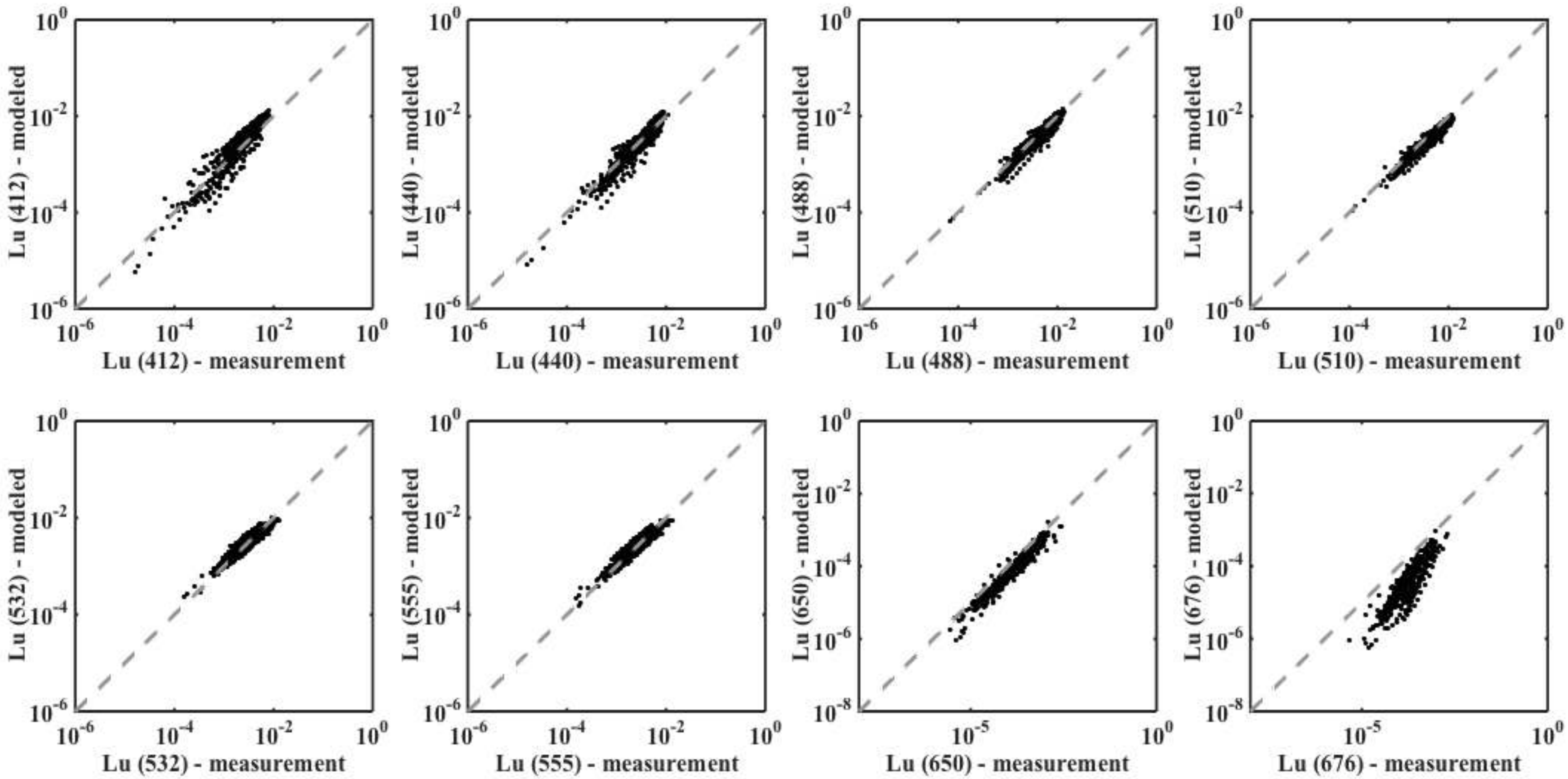

Figure 4.177 Comparison of *in-situ* upward radiance and upward radiance derived from IOPs' measurements at each measured wavelength (nm). Dashed line shows 1:1 ratio.

4.4 Bio-optical Model Development

The Ligurian Sea contains deep, open ocean waters that are broadly consistent with the Case 1 classification where non-water OACs are associated with algal production. For these waters it is relatively simple to establish a fairly standard Case 1 bio-optical model with the following form:

Case 1 IOP model is presented in Eq. 4.7, 4.8 and 4.9 :

$$a(\lambda)=a_w(\lambda)+a(\lambda)_{ph}+{}_{bio}a(\lambda)_{nap}+{}_{bio}a(\lambda)_{CDOM} \qquad (4.7)$$

$$b(\lambda) = b_w(\lambda)+{}_{bio}b_p(\lambda) \qquad (4.8)$$

$$b_b(\lambda) = b_{bw}(\lambda)+{}_{bio}b_{bp}(\lambda) \qquad (4.9)$$

where $a(\lambda)$, $b(\lambda)$, and $b_b(\lambda)$ are spectral absorption, scattering and backscattering coefficients. Subscripts *w*, *ph*, *nap* and *CDOM* refer to water, phytoplankton, non-algal particles and coloured dissolved organic material, while the subscript *p* refers to particles. The subscript *bio* has been introduced to emphasise that the Case 1 assumption implies that NAP absorption, CDOM absorption and particulate scattering and backscattering are all assumed to be biogenic in origin and will subsequently be related to the phytoplankton (Chl) concentration. Note that the biogenic scattering and backscattering components include all particles present in these waters i.e. phytoplankton and any other associated particles such as biogenic detritus.

Coastal waters of the Ligurian Sea are subject to inputs of terrigenous materials from freshwater inflows and resuspension of benthic materials in shallow waters. The following Case 2 bio-optical model is intended to reflect the more complex OAC composition of these waters.

Case 2 IOP model is presented in Eq. 4.10, 4.11:

$$a(\lambda)=a_w(\lambda)+a_{ph}(\lambda)\ +_{bio}a(\lambda)_{nap}+_{nonbio}a(\lambda)_{nap}+_{bio}a(\lambda)_{CDOM}+_{nonbio}a(\lambda)_{CDOM} \quad (4.10)$$

$$b(\lambda) = b_w(\lambda)+_{bio}b_p(\lambda) + {}_{nonbio}b_p(\lambda) \quad (4.11)$$

$$b_b(\lambda) = b_{bw}(\lambda)+_{bio}b_{bp}(\lambda) + {}_{nonbio}b_{bp}(\lambda) \quad (4.12)$$

The Case 2 absorption model builds on the Case 1 version by adding nonbiogenic (*nonbio*) NAP particles, effectively an independent sediment fraction, and non-biogenic CDOM absorption, which is intended to reflect freshwater sources of CDOM. Case 2 scattering and backscattering models include additional non-biogenic components, again reflecting contributions, e.g. sediment resuspension, that are independent of the phytoplankton population.

The next step in the model development is to relate each non-water partial IOP to a relevant ecosystem model currency parameter. For the Case 1 model, the relevant ecosystem model currency is Chl. There is a wealth of literature on potential Case 1 relationships from which the following were selected having been found to provide reasonable fits with the offshore section of the BP09 data and the global NOMAD data set (Werdell & Bailey, 2005).

These Case 1 relationships are assumed to hold for the biogenic material found in Case 2 waters. What follows now is an attempt to obtain models for nonbiogenic particulate absorption, scattering and backscattering. In Case 1 waters, *TSS* is assumed to consist of biogenic particles only. A simple regression forced through zero for offshore stations between *TSS* and Chl (Figure 4.18) gives biogenic *TSS* per unit Chl:

$$TSS_{bio}=0.285*Chl \quad (4.13)$$

Eq.4.13 can be used to estimate the biogenic component of TSS in Case 2 waters, with the nonbiogenic TSS obtained by subtraction (Eq. 4.14):

$$TSS_{nonbio} = TSS_{Case2} - TSS_{bio} \quad (4.14)$$

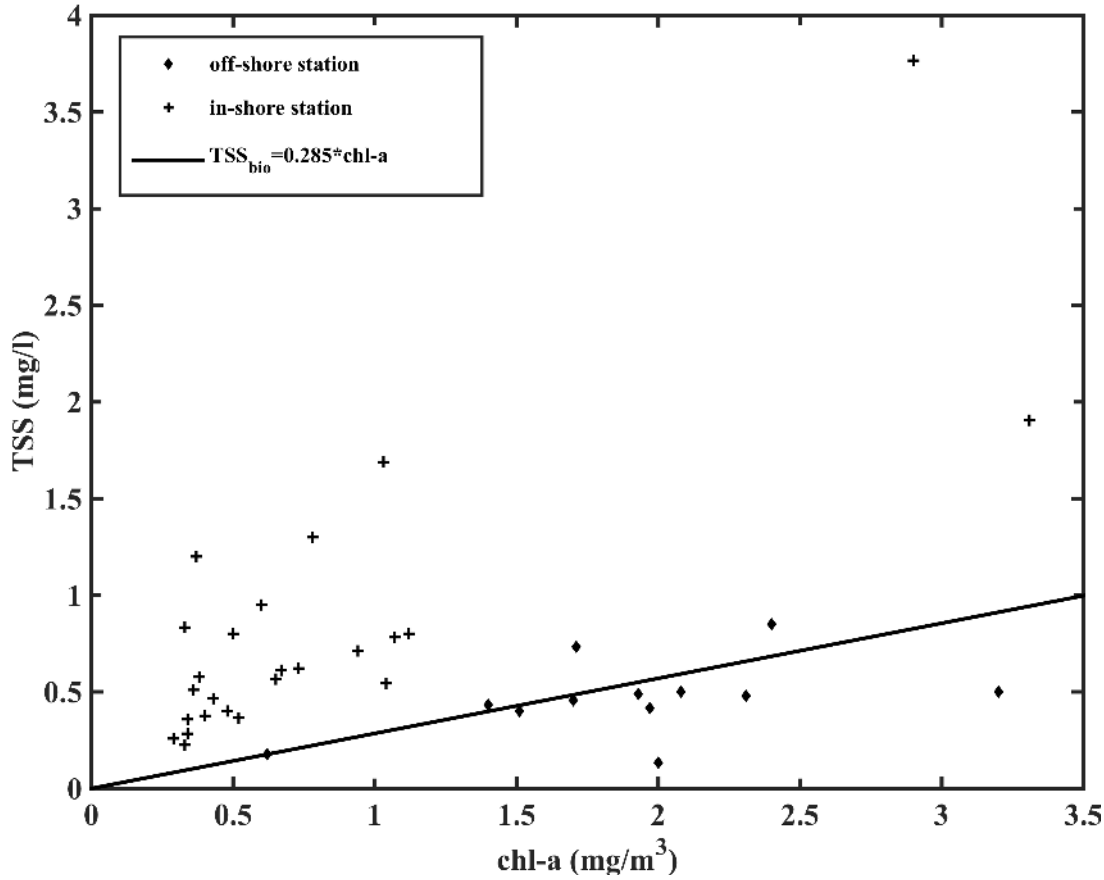

Figure 4.18 Relationship between TSS and Chl in station groups. Black line shows the relation between TSS_{ph} and Chl.

While it is possible to experimentally partition TSS into combustible and non-combustible components, these do not necessarily provide helpful measures for this type of modelling as, for example, the presence of diatom frustules in the non-combustible component potentially breaches the biogenic vs. nonbiogenic partitioning. The TSS partitioning approach presented here is admittedly a little crude, but has the merit of maintaining consistency with the overall model development strategy. For Case 2 waters, the absorption by nonbiogenic particles is obtained by subtracting ${}_{bio}a_{nap}$ obtained using Eqs. 4.18 and 4.19 from measured a_{det}. Likewise, nonbiogenic scattering and backscattering are obtained by subtracting ${}_{bio}b_p$ and ${}_{bio}b_{bp}$ from observed b_p and b_{bp} for Case 2 stations. Best-fit power law regression of these nonbiogenic partial IOPs against TSS_{nonbio} gives relationships of the form (Eq. 4.15, 4.16, 4.17):

$$_{nonbio}a_{nap}(\lambda)= A(\lambda)*TSS_{nonbio}^{B(\lambda)} \quad (4.15)$$

$$_{nonbio}b_{p}(\lambda)= A(\lambda)* TSS_{nonbio}^{B(\lambda)} \quad (4.16)$$

$$_{nonbio}b_{bp}(\lambda)= A(\lambda)* TSS_{nonbio}^{B(\lambda)} \quad (4.17)$$

The bio-optical model focuses Case 1 water, which has mainly phytoplankton as optically significant constituent first part (Case 1water type), additionally other components related in second part (Case 2 water type). The assumption is that the stations have mixed population of phytoplankton and offshore stations have Case 1 water type optical properties. Onshore stations may include additional impact of the other optically active components.

4.4.1 Case 1 Water Type

4.4.1.1 Absorption Coefficient by Phytoplankton

Absorption coefficients by phytoplankton are mainly related with chlorophyll-a due to capturing the light for photosynthesis. chlorophyll-a shows two peaks in visible light spectrum; one is in blue region and other is in red region. Even though the peak centers change due to phytoplankton groups, 440 nm and 676 nm are generally accepted as center of chlorophyll-a peaks of mixed phytoplankton communities in the spectrum. The a_{ph} is main contributor for variability in Case 1 water type, thus its role is really important to understand the light distribution and estimation of primary production. Well-known approach estimating a_{ph} from chlorophyll-a in the literature is to express a_{ph} as a power function of Chl (Prieur & Sathyendranath, 1981; Bricaud et al., 1995, 1998; Velluci, 2007).

Bricaud et al. (1995) is the most popular relationship for this purpose. Velluci (2007) has a local dataset in the study to present the relationship in the Mediterranean Sea. To compare field measurement with global data-set (NOMAD) and relationships of Bricaud et al. (1995) and Velluci (2007) between a_{ph} and Chl at 440nm and 676 nm are presented in Figure 4.19.Field data-set has good agreement with NOMAD data-set, thus, we can assume NOMAD data-set represents the field measurements in wider range of Chl and a_{ph}at 440 nm (and 676 nm). Both of the methods explain most of the data in both wavelengths. But, relationship defined by Velluci (2007) has better performance than relationship of Bricaud et al. (1995) in higher Chlorophyll-a values at 440 nm. When taking into account this fact, Velluci (2007) used Mediterranean dataset to define relationship, the method given by Velluci (2007) is better for the Ligurian Sea. The power relationship is shown in Eq.4.18 and coefficients are presented in Table 4.6.

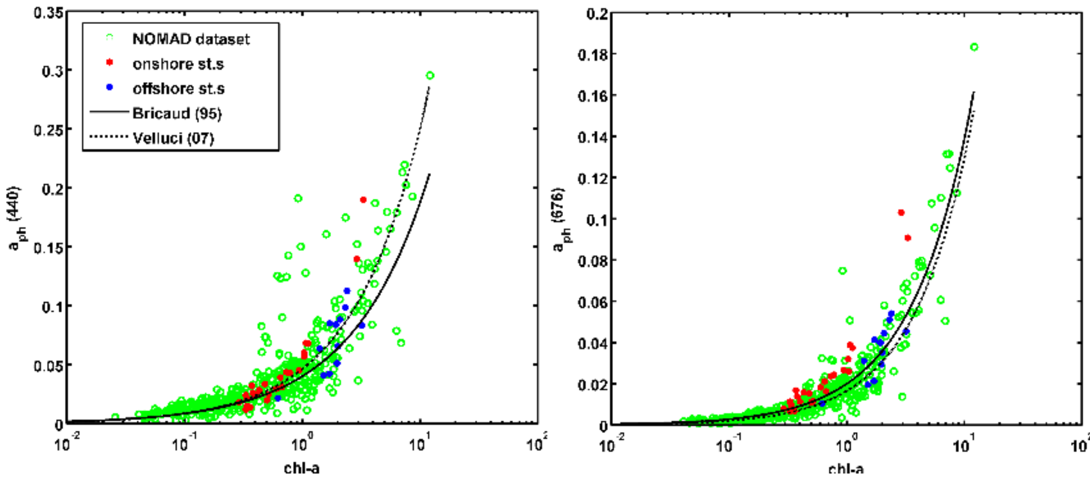

Figure 4.19 Relationship between Chlorophyll-a and a_{ph} at 440 nm (left) and at 676 nm (right).

$$\alpha(\lambda) * [Chl]^{\beta(\lambda)} \quad (4.18)$$

4.4.1.2 Absorption Coefficient by Non-algal Particles

Absorption coefficient by non-algal particles in Case 1 waters refers detrital particles released by organism or remnant of death organisms. Thus, it is expected to have relationship between Chlorophyll-a and a_{nap} in Case 1 waters. Bricaud et al.

(1998) presented a power relationship between a_{nap} and Chl by using a_p and a_{ph} and they reported this relationship is not as strong as relationship of a_p and a_{ph} with Chl. Velluci (2007) also reported coefficients for this conversion, but also notes that the relationship has very low regression coefficients. Both publications also reported a power relation between a_p and Chl.

Table 4.6 α(λ) and β(λ) coefficients for $a_{ph}(\lambda)$ for euphotic depth (from Velluci (2007)).

(λ)	**α(λ)**	**β(λ)**
412	0.04203	0.70935
440	0.04657	0.73119
488	0.02946	0.71921
510	0.01847	0.7176
532	0.0115	0.6956
554	0.00782	0.67126
650	0.0074	0.78503
676	0.01654	0.89313

Spectral dependence of a_{nap} is defined as exponential function between reference wavelength in high absorption region (blue) and interested wavelengths. Mean slope in Mediterranean are reported as 0.011 by Velluci (2007) with a large dataset, this value is the same in the study by Bricaud et al. (1998). Babin et al. (2003) reported the slope value in European seas. This value is 0.0129 in the Mediterranean (N=53).

As seen in Figure 4.20, NOMAD dataset has good agreement with most of field measurements for comparison of Chl and a_{nap}. Onshore stations and some offshore stations have different trend. The difference might be input of terrestrial particles as expected in Case 2 waters. While relationship given by Bricaud (1998) explains most of the data, the relationship given by Velluci (2007) has no sense to explain relationship between a_{nap} and Chl. This fact was also reported by Velluci (2007). The power function as given in Eq. (4.19). As alternative, relationship between a_p at 440 nm and Chl were compared with the methods given by Bricaud (1998) and Velluci (2007). Besides data sets having agreement both of the relationships have good agreement with each other and they explains most of the data. Velluci (2007) is more suitable for explaining the relationship between a_p and Chl due to being local tuning and slightly closer to data distribution in higher Chl values. The coefficients from Velluci (2007) are given in Table 4.7. Relationship among a_p, a_{ph} and a_{nap} are given in Eq.(4.20).

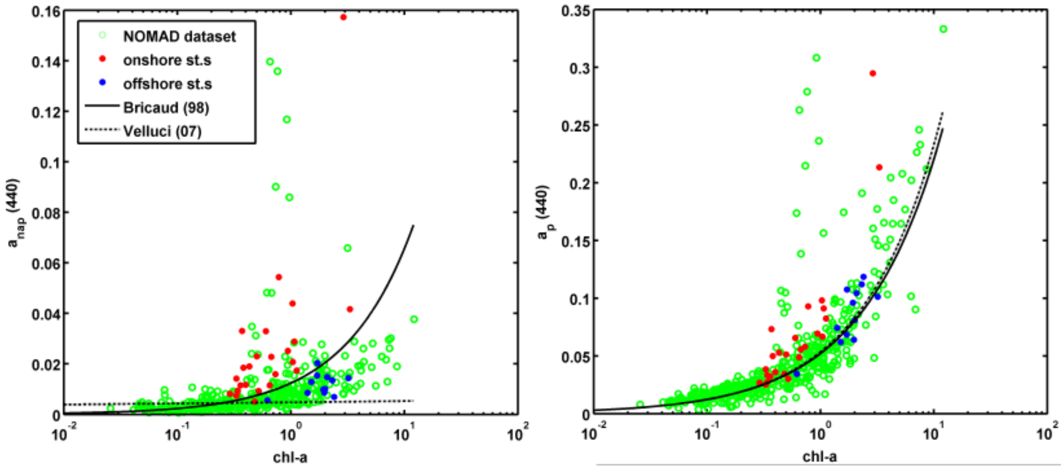

Figure 4.20 Relationship between Chlorophyll-a and a_{nap} at 440 nm (left) and between Chlorophyll-a and a_p at 440 nm (right).

$$a_{nap}(\lambda) = a_{nap}(440)*\exp[-S*(\lambda-440)] \quad (4.19)$$

$$a_{nap}(440)=0.0124*[Chl]^{0.724} \quad (4.20)$$

$$a_p(\lambda) = a_{nap}(\lambda) + a_{ph}(\lambda) \quad (4.21)$$

Table 4.7 $\alpha(\lambda)$ and $\beta(\lambda)$ coefficients for $a_p(\lambda)$ for euphotic depth (from Velluci (2007)).

(λ)	**α(λ)**	**β(λ)**
412	0.05126	0.59732
440	0.05341	0.63923
488	0.03332	0.62464
510	0.02153	0.60715
532	0.01393	0.57341
554	0.00971	0.54664
650	0.00812	0.71736
676	0.01725	0.86031

4.4.1.3 Absorption Coefficient by Colored Dissolved Organic Matter (CDOM)

Colored dissolved organic matter is an important part of dissolved organic matter that forms exudation of living organisms. It has importance for living organism due to absorbing UV part of light spectrum, which has a harmful effect on them. Absorption by CDOM has exponential relationship with light spectrum such as non-algal particulate absorption (Eq. (4.8)), decreases towards higher wavelengths. Babin et al., (2003) reported the slope value as 0.017 in the Mediterranean Sea. Main source for CDOM in Case 1 waters is phytoplankton species. Its main source may vary in Case 2 waters with terrestrial input or re-suspension.

Relationship between Chl and a_{cdom} were studied by Prieur & Sathyendranath (1981) and defined as a power function of Chl with contribution of water absorption (a_w). This relationship was modified by Velluci (2007) for the Mediterranean Sea, but it should be noted that CDOM dataset was obtained from total absorption by subtracting a_p and a_w in the study. Another relationship was defined by Morel (2009) as power function of Chl. Bricaud et al. (1998) defined a relationship between a_{cdom} and sum of a_w and a_p.

The relationships that are mentioned above were compared with field measurements and NOMAD dataset at 440 nm and results are presented in Figure 4.21. As seen in Figure 4.21, data scatter in NOMAD dataset. Field data shows two main trends; offshore data-set shows lower increasing trend than onshore dataset as expected. Besides the contribution of terrestrial inputs and/or re-suspension, competition among particles and fresh water input might be the reason for high mortality rate in onshore waters with high exudation of CDOM. Comparison of the relationships are given below with the field data showing that the most suitable relationship is the one given by Prieur & Sathyendranath (1981) for the Ligurian Sea. The relationship is given in Eq. (4.22).

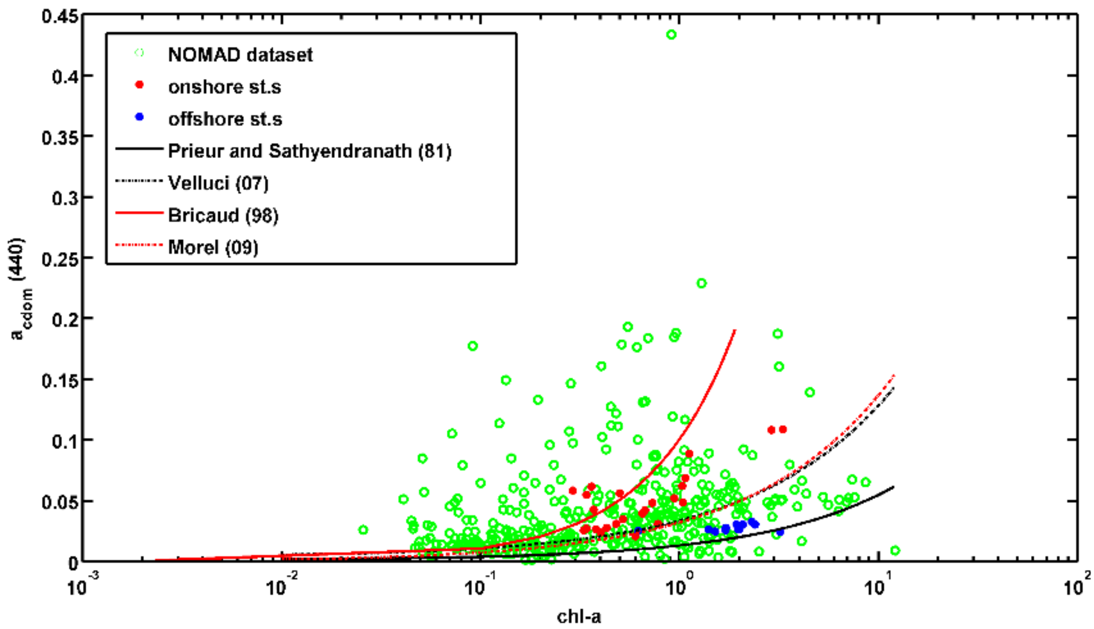

Figure 4.21 Relationship between Chlorophyll-a and a_{cdom} at 440 nm for dataset NOMAD and this study. Blue dots, off-shore stations, are important due to representing Case 1 waters. Even though all relationships explain the dataset because of the datasets disperse, Prieur & Sathyendranath (1981) shows better explanation for measurements in off-shore region.

$$a_{cdom}(440)=0.2*[aw(440)+0.06*(Chl)^{0.65}] \quad (4.22)$$

4.4.1.4 Scattering by Particulate Matter

Scattering coefficients in Case 1 water are expected to be related with phytoplankton community due to being the main contributor for optically active components. Some studies reported the relationship between Chl and particulate scattering coefficient (b_p) (Gordon & Morel, 1981; Loisel & Morel, 1998; Velluci, 2007). Spectral dependency of b_p can be formulized as function of power relationship of Chl and wavelengths ratio (λ/λ_o).

Due to not having data on b_p in NOMAD dataset, field data was used for comparing the relationships. As seen in Figure 4.22, while data from offshore stations show a trend with Chl, most of the onshore stations are scattered. Result of the comparison among the relationships given by previous studies shows Gordon & Morel (1981) and Velluci (2007) are more suitable for offshore area of the Ligurian

Sea. Equation (4.23) shows the relationship between Chl and b_p as given by Velluci (2007), which was improved by using, dataset from the Mediterranean Sea.

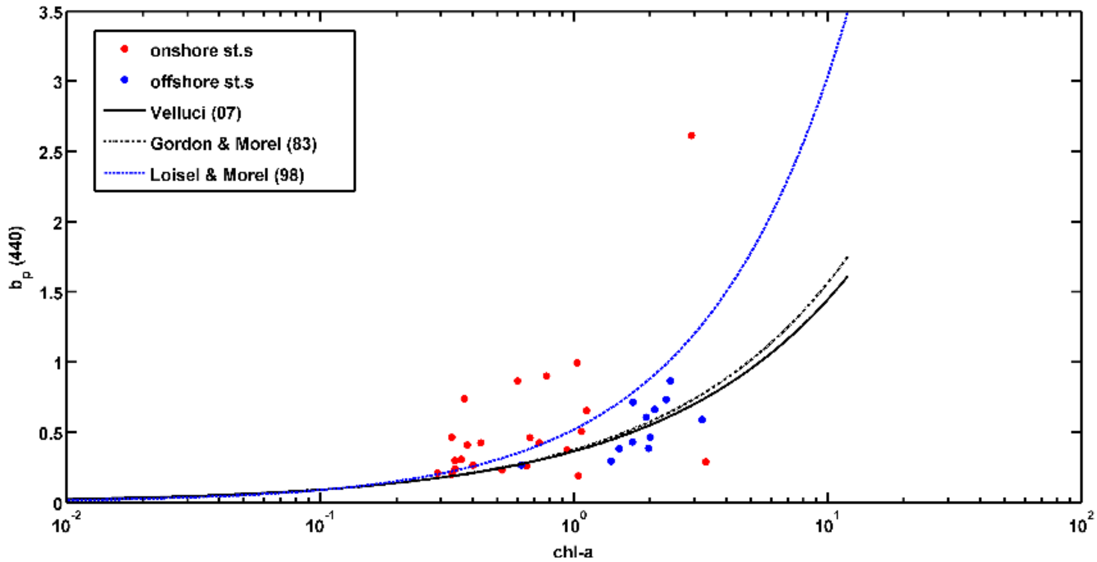

Figure 4.22Relationship between Chlorophyll-a and b_p at 440 nm.

$$b_p(\lambda) = 0.289 * [Chl]^{0.598} * (\lambda/\lambda o) \quad (4.23)$$

4.4.1.5 Backscattering by Particulate Matter

Phytoplankton are known for their weak backscattering features due to plasmic cell structure, excluding some special groups that are covered by inorganic matter. Backscattering coefficients in non-algal particles are stronger than phytoplankton. In Case 1 waters, due to dominancy of phytoplankton, a relationship between particulate backscattering coefficient (b_{bp}) and Chl was expected. Morel (1988) presented a relationship between b_{bp} and Chl, it is modified in Morel & Maritorena (2001). Velluci (2007) used Mediterranean dataset to define power function between them.

As seen in Figure 4.23, most of NOMAD data and field measurements show that similar increasing tendency depend on Chl. Some of the stations in field measurements scattered and show high b_{bp} in low Chl concentrations. It might be because of presence of non-algal particle content. Results of the comparison of the methods and datasets show relationship given by Velluci (2007) explains most of the NOMAD dataset and offshore stations. Coefficients of the power relationship between b_{bp} and Chl are shown in Table 4.8.

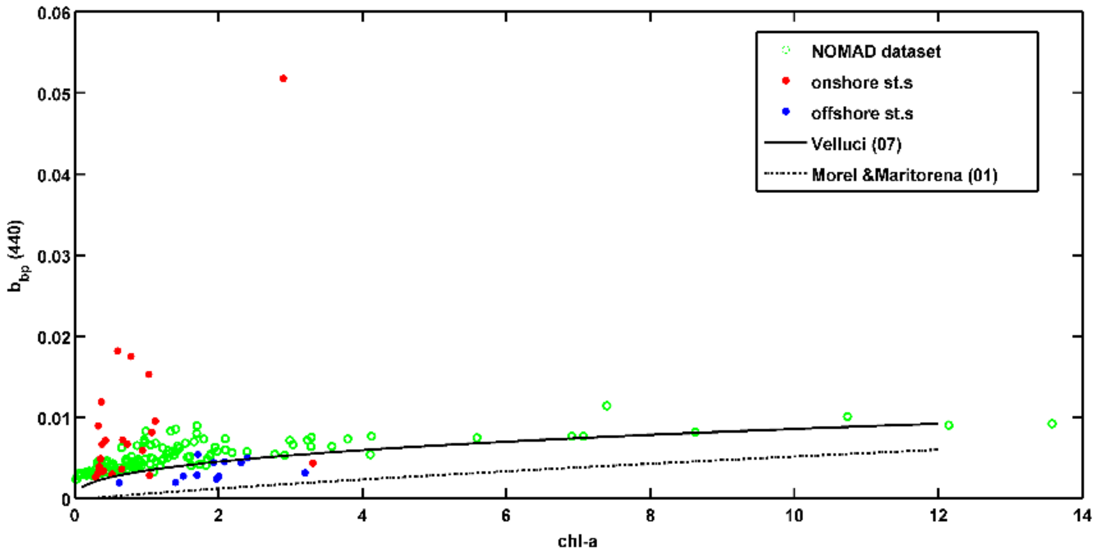

Figure 4.23 Relationship between Chlorophyll-a and b_{bp} at 440 nm. The relationship given by Velluci (2007) is for 443 nm.

Table 4.8α(λ) and β(λ) coefficients for b_{bp}(λ) (from Velluci (2007)).

(λ)	α(λ)	β(λ)
400	0.00342	0.48635
412	0.00384	0.47311
443	0.00342	0.39816
470	0.00366	0.45569
491	0.0034	0.51667
510	0.00366	0.51504
532	0.00318	0.57934
555	0.00315	0.64753

4.4.2 Case 2 Water Type

4.4.2.1 Nonbiogenic Non-algal Particulate Absorption Coefficient ($_{nonbio}a_{nap}$) by Nonbiogenic TSS

TSS_{nonbio} related part of non-algal absorption ($_{nonbio}a_{nap}$) is calculated by subtracting results of Eq. 4.9 from measured a_{nap} of onshore stations. TSS_{nonbio} showed significant relationship with $_{nonbio}a_{nap}$. Figure 4.24 and Eq. 4.24 show the relationship.

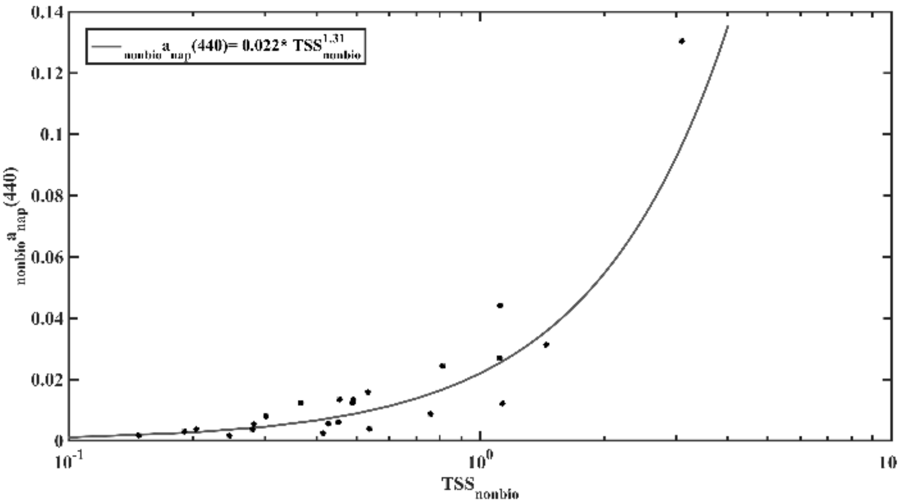

Figure 4.24 Relationship between TSS_{nonbio} and $_{nonbio}a_{nap}$ at 440 nm.

$$_{nonbio}a_{nap}(440)= 0.022* TSS_{nonbio}^{1.31} \qquad (4.24)$$

4.4.2.2 Nonbiogenic Particulate Scattering Coefficient ($_{nonbio}b_p$) by Nonbiogenic TSS

TSS_{nonbio} related part of non-algal related part of particulate scattering ($_{nonbio}b_p$) is calculated by subtracting from calculated b_p of AC-9 in onshore stations. TSS_{nonbio} showed significant relationship with $_{nonbio}b_p$. Figure 4.25 and Eq. 4.25 show the relationship.

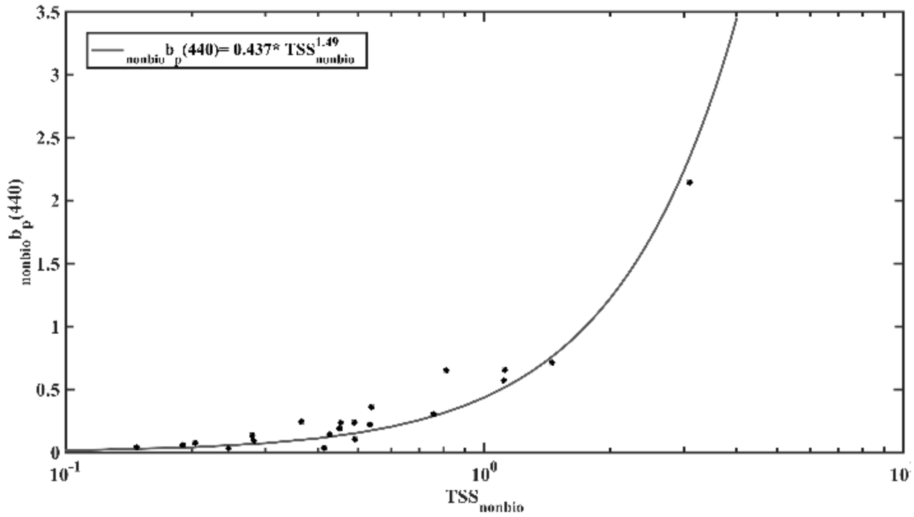

Figure 4.25 Relationship between TSS_{nonbio} and ${}_{nonbio}b_p$ at 440 nm.

$$ {}_{nap}b_p(440)= 0.437* TSS_{nap}^{1.49} \qquad (4.25) $$

4.4.2.3 Nonbiogenic Particulate Backscattering Coefficient (${}_{nonbio}b_{bp}$) by Nonbiogenic TSS

TSS_{nonbio} related part of non-algal related part of particulate scattering (${}_{nonbio}b_{bp}$) is calculated by subtracting of results of Eq. 4.12 from measured b_{bp} in onshore stations. TSS_{nonbio} showed significant relationship with ${}_{nonbio}b_{bp}$. Figure 4.26 and Eq. 4.26 show the relationship.

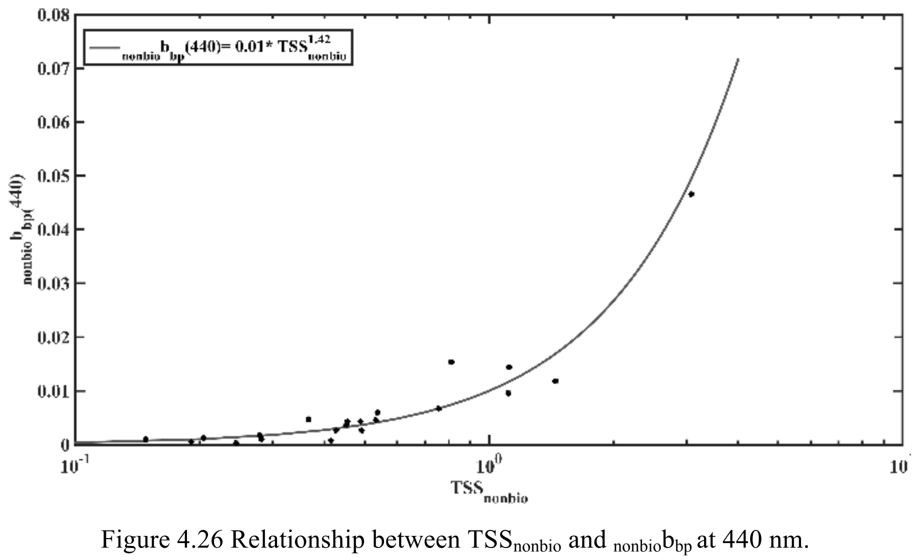

Figure 4.26 Relationship between TSS_{nonbio} and ${}_{nonbio}b_{bp}$ at 440 nm.

$$_{nap}b_{bp}(440) = 0.01 * TSS_{nonbio}^{1.42} \quad (4.26)$$

Coefficients for the relationships between IOPs and TSS_{nonbio} are given in Table 4.9.

Table 4.9 Coefficient values for $_{nap}a_{nap}(\lambda)$, $_{nap}b_{p}(\lambda)$ and $_{nap}b_{bp}(\lambda)$.

Variables	Coefficients	Wavelengths (nm)							
		412	**440**	**488**	**510**	**532**	**555**	**650**	**676**
$_{nonbio}a_{nap}$	**A(λ)**	0.028	0.020	0.013	0.013	0.011	0.009	0.007	0.002
	B(λ)	1.405	1.3045	1.45	1.49	1.065	1.26	0.87	0.85
	R^2	**0.81**	**0.77**	**0.83**	**0.80**	**0.82**	**0.84**	**0.67**	**0.62**
$_{nonbio}b_{p}$	**A(λ)**	0.446	0.451	0.43	0.442	0.4452	0.455	0.435	0.391
	B(λ)	1.4167	1.357	1.3135	1.265	1.2566	1.22	1.245	1.342
	R^2	**0.83**	**0.81**	**0.87**	**0.88**	**0.83**	**0.82**	**0.86**	**0.85**
$_{nonbio}b_{bp}$	**A(λ)**	0.0091	0.0081	0.0087	0.009	0.0081	0.007	0.008	0.006
	B(λ)	1.48	1.5646	1.3095	1.264	1.263	1.245	1.416	1.154
	R^2	**0.80**	**0.81**	**0.83**	**0.84**	**0.84**	**0.84**	**0.83**	**0.82**

4.4.2.4 Contribution of Absorption by CDOM to Total Absorption in Case 2 Water

Absorption by CDOM is one of the challenges in bio-optical modeling. As known, in Case 1 waters, phytoplankton are the main source for the CDOM. In Case 2 waters, main source depends on common terrestrial sources generally carried into thesea by flowing rivers and other fresh/brackish water sources. This fact makes difficult modeling absorption by CDOM in Case 2 waters. Despite this difficulty, CDOM absorption might be related with some indicators of the terrestrial inputs. Salinity is generally stable in marine water regions unless having inputs from different sources. Decreases in salinity of seawater might show the possible CDOM increases in the area.

Figure 4.27 shows a global relationship between CDOM absorption and salinity from the NOMAD dataset. Low salinity values are associated with regions of stronger freshwater input with higher levels of CDOM absorption. The

Mediterranean Sea has very restricted exchange with the global ocean and evaporation rates exceed freshwater inputs leading to unusually high salinity levels, as seen in the relatively high values for the BP09 data included in Figure 4.27. As a result, a small offset was added to the global salinity – CDOM relationship for operation in the relatively high salinity waters of the Mediterranean Sea.

$$_{nonbio}a_{CDOM}(440)=-0.018*salinity+0.73 \qquad (4.27).$$

This nonbiogenic component of CDOM absorption is only invoked when salinity drops below a threshold value of 37 PSU.

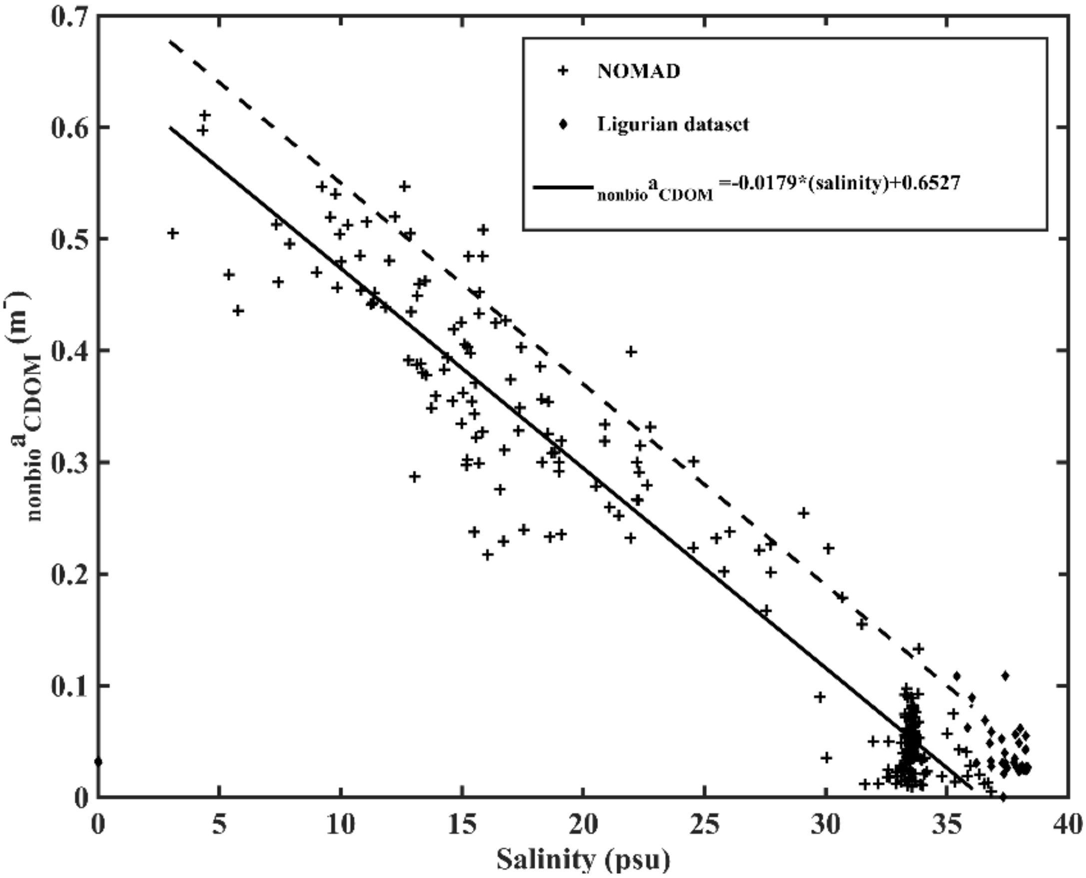

Figure 4.27 Relationship between $a_{cdom}(440)$ and salinity measurements. Symbol plus indicates NOMAD data-set, symbol diamond indicates the Ligurian Sea data-set. Solid line represents the best fit for NOMAD data set, dashed line represents the adapted the best fit related to salinity values of the Ligurian Sea.

4.4.3 Bio-optical Model Validation Strategy

The aim of this work is to develop a bio-optical model that will ultimately be incorporated into the Ligurian Sea ecosystem model to improve prediction of underwater light fields and associated impacts on phytoplankton photosynthesis and solar heating. Data for assimilation into and validation of the ecosystem model may ultimately come from a variety of sources including satellite remote sensing and/or in situ observations from moorings (static or profiling) or autonomous vehicle platforms. In each case there is a need to adopt a common currency between external data observations and the ecosystem model. In this work, this common currency has been selected to be Chl, TSS and Salinity. Here simple linear calibrations are applied to turbidity and fluorescence data collected on CTD profiles to generate proxy profiles of *TSS* and *Chl*. In this work the data has been partitioned by geographical location, with offshore stations regarded as Case 1 and onshore stations regarded as Case 2. In future it would be possible to further refine the assignment of Case 1 / 2 status using derived values of TSS and Chl to determine whether to use Case 1 or Case 2 bio-optical models for the particulate component of IOPs, with the bifurcation in Figure 4.18 acting as a simple threshold differentiator. Similarly, *Salinity* data reveals whether or not there is a significant freshwater influence and if a nonbiogenic component of CDOM absorption is required.

Validation of the proposed bio-optical model is therefore in four steps:

1. CTD + fluorescence + turbidity profiles provide *Salinity* and estimation of *Chl* and *TSS*.

2. Case 1 or Case 2 bio-optical models are selected as appropriate.

3. Proxy IOP profiles are determined and submitted as input to Ecolight.

4. Modelled radiometric data are compared against in situ measurements.

This optical closure approach using in situ *Ed* and *Lu* data for model validation provides a rigorous test of the bio-optical model and its implementation with a proxy data input method, and therefore gives a relatively strong indication of the level of performance that might be achievable from such a system in practise.

4.5 Bio-optical Model Validation

Turbidity and fluorescence sensors were calibrated with surface TSS and Chl data from across the region, using data from 35 and 32 stations respectively. The data ranged between 0.29 mg m^{-3} and 3.31 mg m^{-3} for Chl, and 0.13 mg l^{-1} and 3.77 mg l^{-1} for TSS. Significant linear relationships were found between turbidity values and *TSS*(R^2 = 0.85), and between fluorescence values and *Chl* (R^2 = 0.71) (Figure 4.28).

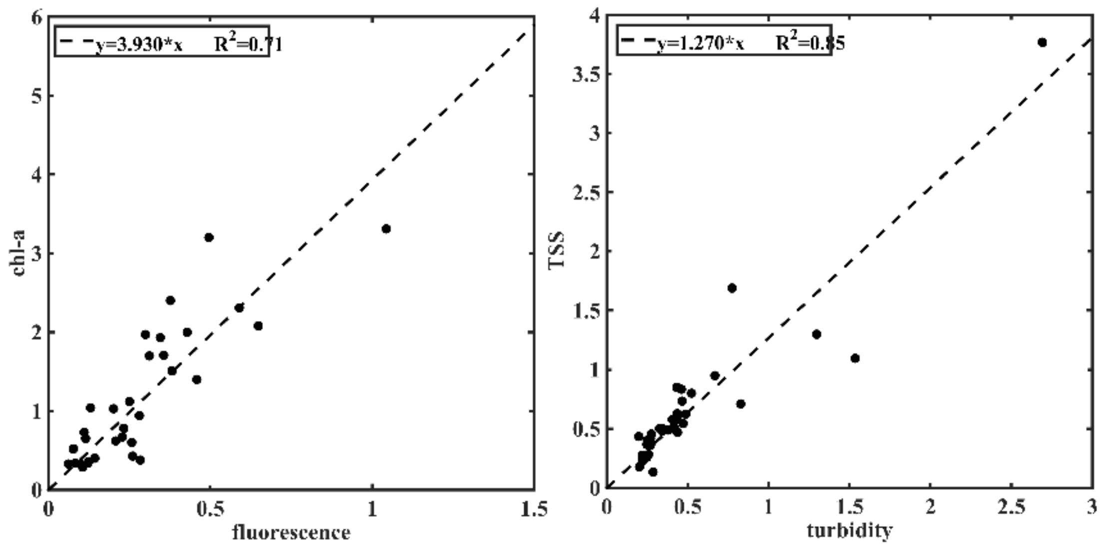

Figure 4.28 Relationship between Chlorophyll-a from HPLC and from fluorescence sensor (left panel); total suspended matter concentration from filter pad and FTU from turbidity-meter.

These calibrations were used to generate estimated profiles of *Chl* and *TSS* from CTD fluorescence and turbidity profiles, which, along with CTD *Salinity* profiles, are sufficient to parameterize the Ligurian Sea bio-optical model as described above. The performance of the bio-optical model was determined by comparison with corresponding IOP data obtained from in situ AC-9+ and BB9 measurements (see Table 4.10 for descriptive statistics for these measurements). The subsequent performance of Ecolight radiative transfer simulations using the Ligurian Sea bio-optical model as input was assessed against in situ radiometric measurements (downwards irradiance *Ed* and upwards radiance *Lu*) and derived apparent optical properties (downwards diffuse attenuation K_d and radiance reflectance R_L). Table 4.10 provides descriptive statistics for these measured light field parameters.

Table 4.10 Descriptive statistics of the *in-situ* data from AC-9+ and BB9 instruments (a_t=total absorption coefficient, a_w=absorption by seawater, b_p=scattering coefficient, b_{bp}=backscattering coefficient).

Variable	Parameter	Wavelength (nm)							
		412	440	488	510	532	555	650	676
a_t-a_w (m^{-1})	mean	0.0891	0.0688	0.0410	0.0293	0.0225	0.0140	0.0066	0.0175
	std	0.0301	0.0272	0.0184	0.0134	0.0098	0.0067	0.0036	0.0091
	max	0.6551	0.5402	0.3407	0.2646	0.2050	0.1429	0.0706	0.1606
	min	0.0013	0.0000	0.0000	0.0000	0.0000	0.0000	0.0000	0.0010
b_p (m^{-1})	mean	0.4538	0.4402	0.4298	0.4265	0.4201	0.4175	0.3777	0.3513
	std	0.1858	0.1816	0.1789	0.1786	0.1771	0.1753	0.1587	0.1501
	max	3.5746	3.5041	3.3555	3.2637	3.1909	3.1447	2.9598	2.7735
	min	0.0337	0.0302	0.0292	0.0263	0.0266	0.0259	0.0218	0.0158
b_{bp}(m^{-1})	mean	0.0086	0.0078	0.0079	0.0084	0.0074	0.0071	0.0069	0.0062
	std	0.0039	0.0035	0.0035	0.0037	0.0033	0.0032	0.0031	0.0028
	max	0.0932	0.0849	0.0837	0.0867	0.0775	0.0747	0.0732	0.0637
	min	0.0006	0.0006	0.0007	0.0010	0.0008	0.0007	0.0006	0.0005

To validate the outputs of the developed model, retrieved IOPs from model estimations without water contribution and *in-situ* measurements were compared (N= 2047 for absorption and scattering, N=2060 for backscattering) for each chosen wavelength. Significant correlations were observed between model results and *in-situ* data in each variable at all wavelengths (Table 4.11). The highest correlation, 0.88 was observed in absorption and particulate backscattering at 676 nm, while the lowest correlation, 0.78, was observed in scattering at 676 nm. Wavelengths from modeled and measured IOPs are presented in Figure 4.29 for absorption coefficient, Figure 4.30 for particulate scattering coefficient and Figure 4.31 for particulate backscattering coefficient. Mean errors of the outputs of the model were very low for each variable. However, range of the errors show that there are no biases in estimated dataset. A simple regression was forced through zero between estimated values and *in-situ* data to evaluate ratio of modeled and *in-situ* values. Significant regression coefficients were observed. Ratios between modeled and *in-situ* values were around 1 with a range between 0.6 and 1.3. The ratios in absorption were lower than 1 in all wavelengths. This fact indicates that absorption has an underestimation trend in all wavelengths. Selected statistical comparisons of the datasets are shown in Table 4.11.

Table 4.11 Resulting statistical comparison of the *in-situ* dataset and dataset retrieved from the model.

	Wavelengths (nm)							
Statistics	**412**	**440**	**488**	**510**	**532**	**555**	**650**	**676**
				a_t-a_w				
Minimum error	-0.207	-0.140	-0.116	-0.109	-0.099	-0.069	-0.021	-0.064
Maximum error	0.172	0.156	0.094	0.111	0.038	0.046	0.026	0.045
Mean error	0.010	0.015	0.008	0.005	0.002	0.004	0.005	0.001
Root mean square error	0.032	0.029	0.017	0.013	0.009	0.008	0.006	0.007
Linear correlation (r)	0.82	0.84	0.84	0.81	0.82	0.79	0.84	0.88
Slope (in-situ/modeled)	0.9	0.8	0.8	0.9	0.9	0.8	0.6	0.9
R^2	0.71	0.71	0.68	0.63	0.60	0.51	0.57	0.77
				b_p				
Minimum error	-2.012	-1.983	-2.064	-2.079	-2.088	-2.101	-2.019	-1.895
Maximum error	2.054	1.698	1.290	1.160	1.177	1.089	1.297	1.575
Mean error	0.013	0.008	-0.017	-0.026	-0.031	-0.037	-0.035	-0.027
Root mean square error	0.163	0.156	0.160	0.164	0.168	0.172	0.166	0.157
Linear correlation (r)	0.83	0.84	0.83	0.82	0.81	0.80	0.78	0.77
Slope (in-situ/modeled)	1.0	1.0	1.1	1.1	1.1	1.1	1.1	1.0
R^2	0.70	0.70	0.69	0.68	0.67	0.66	0.64	0.64
				b_{bp}				
Minimum error	-0.056	-0.053	-0.053	-0.055	-0.044	-0.041	-0.045	-0.040
Maximum error	0.038	0.048	0.015	0.010	0.011	0.010	0.029	0.005
Mean error	0.000	0.000	-0.001	-0.002	0.000	0.000	-0.001	-0.001
Root mean square error	0.004	0.003	0.003	0.004	0.003	0.003	0.003	0.002
Linear correlation (r)	0.82	0.79	0.84	0.85	0.84	0.84	0.82	0.87
Slope (in-situ/modeled)	1.0	0.9	1.2	1.3	1.1	1.0	1.1	1.2
R^2	0.67	0.65	0.73	0.75	0.69	0.67	0.71	0.73

Descriptive statistics of the modeled dataset (Table 4.12) show similar results with *in-situ* dataset (Table 4.12). Modeled dataset has lower mean values than *in-situ* dataset for all variables of all wavelengths. Absorption has systematically lower estimated values for maximum values of the dataset ranges, while it is significantly higher values for minimum. Scattering shows higher estimations in both, maximum and minimum. Backscattering estimations vary depending on the wavelengths.

Table 4.12 Descriptive statistics of the dataset retrieved from model.

Variable	Parameter	Wavelength (nm)							
		412	440	488	510	532	555	650	676
a (m^{-1})	mean	0.0860	0.0766	0.0452	0.0306	0.0209	0.0147	0.0106	0.0190
	Std	0.0520	0.0456	0.0268	0.0188	0.0117	0.0086	0.0061	0.0139
	Max	0.6308	0.5112	0.2854	0.1998	0.1318	0.0939	0.0644	0.1383
	Min	0.0146	0.0121	0.0070	0.0047	0.0039	0.0026	0.0020	0.0019
b_p (m^{-1})	mean	0.3526	0.3357	0.3067	0.2990	0.2899	0.2832	0.2481	0.2328
	Std	0.2604	0.2463	0.2235	0.2180	0.2160	0.2123	0.2044	0.2023
	Max	5.0583	4.6401	4.1121	3.9081	3.8658	3.7227	3.6732	3.8596
	Min	0.0916	0.0892	0.0831	0.0832	0.0812	0.0812	0.0704	0.0623
b_{bp} (m^{-1})	mean	0.0050	0.0045	0.0034	0.0034	0.0043	0.0043	0.0033	0.0031
	Std	0.0053	0.0051	0.0042	0.0041	0.0039	0.0037	0.0043	0.0029
	Max	0.1112	0.1133	0.0794	0.0762	0.0700	0.0650	0.0869	0.0488
	min	0.0013	0.0013	0.0009	0.0009	0.0010	0.0009	0.0010	0.0010

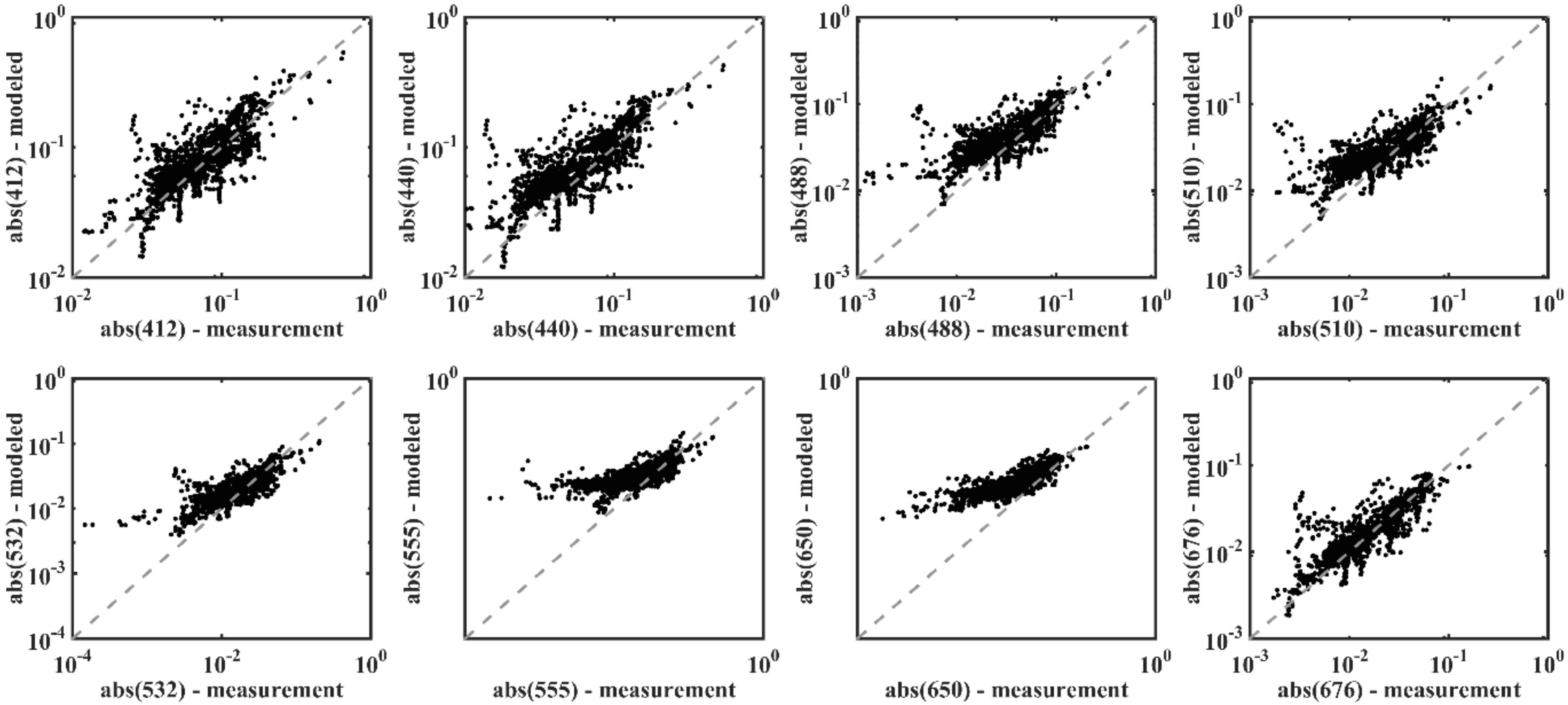

Figure 4.29 Relationship between measured absorption coefficients and modeled absorption coefficients at the wavelengths (m^{-1})

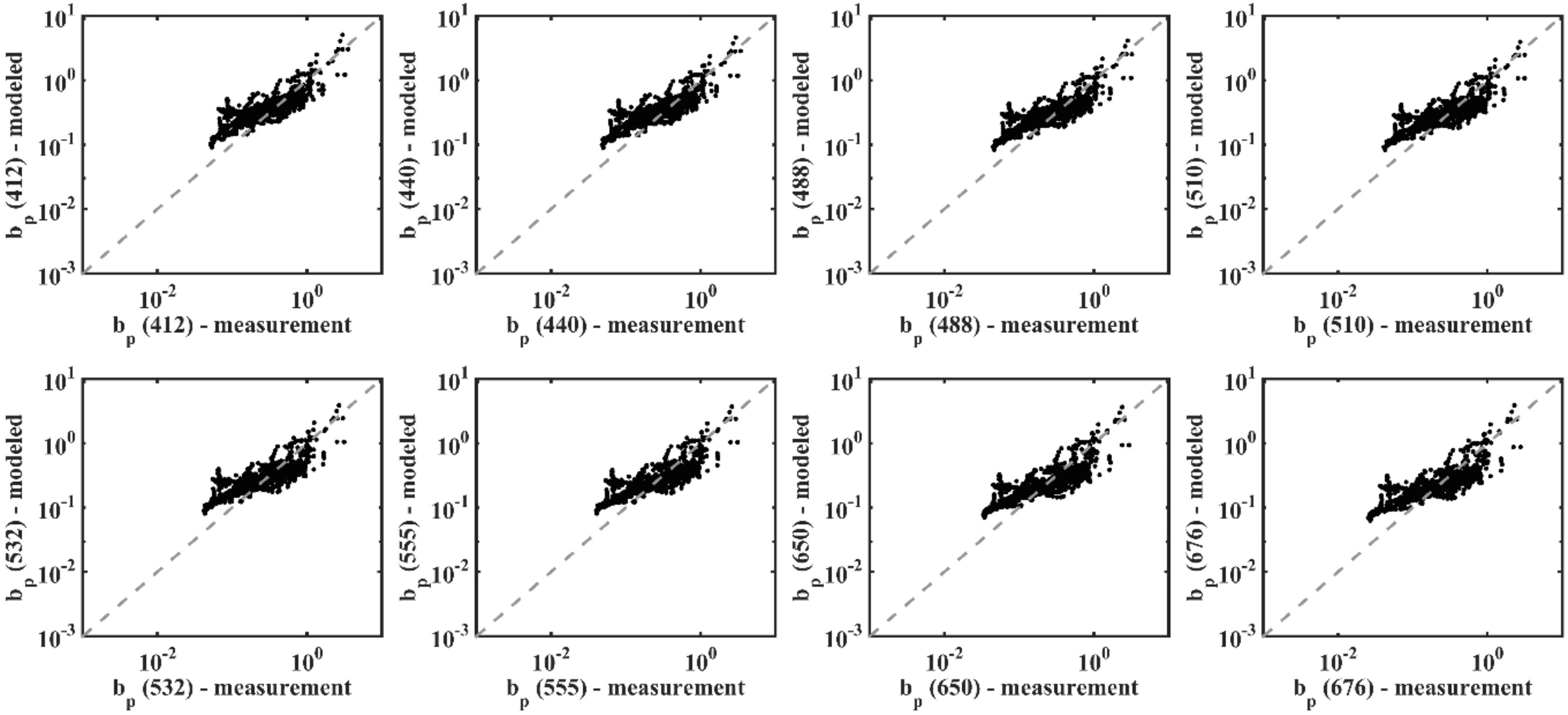

Figure 4.30 Relationship between measured particulate scattering coefficients and modeled particulate scattering coefficients at the wavelengths (m^{-1})

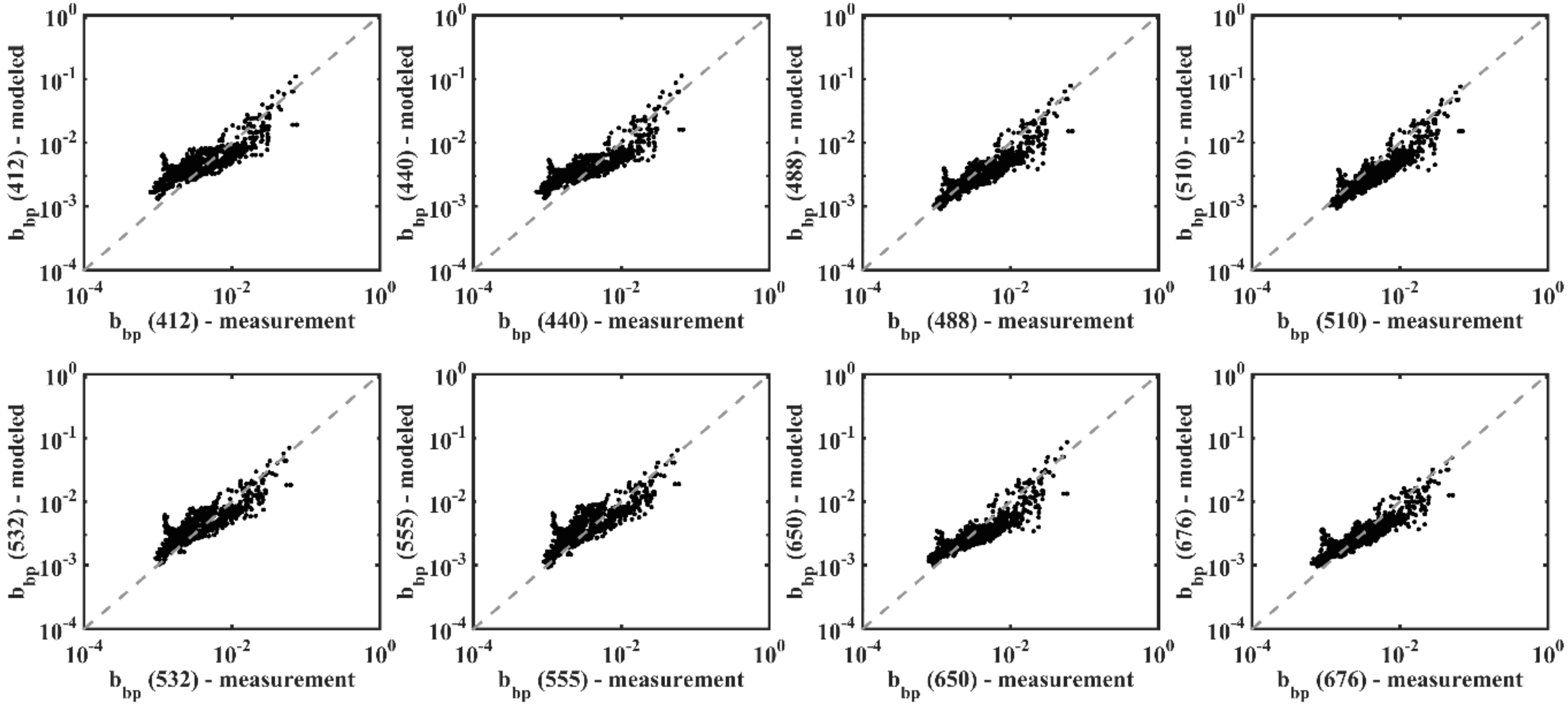

Figure 4.31 Relationship between measured particulate backscattering coefficients and modeled particulate backscattering coefficients at the wavelengths (m^{-1}).

4.6 Radiative Transfer Model Validation

Underwater light fields were simulated for each station using Ecolight (Sequoia Scientific Inc.) and parameterized using the bio-optical model described above, together with measured above surface downwards irradiance values and solar zenith angles. Simulated underwater radiometry outputs were validated against *in situ* spectral E_d and L_u measurements (N = 452, Figure 4.29) and integrated (400 – 700 nm) photosynthetically active radiation (E_{PAR} and L_{PAR}). Descriptive parameters of the dataset that were obtained from model show similar values with *in-situ* measurements. The parameters for estimated dataset are given together with *in-situ* dataset in Table 4.13. Significant correlations were observed between results from the model and *in-situ* measurements in each variable at all wavelengths and PAR (Table 4.14). As an example, a comparison *in-situ* and modeled profiles of a station in wavelengths are presented in Figure 4.32

Table 4.13 Descriptive statistics of Ed and Lu *in-situ* dataset and dataset retrieved from model.

	Wavelengths (nm)								
Parameter	**412**	**440**	**488**	**510**	**532**	**555**	**650**	**676**	**PAR**
					***in-situ* Ed**				
Mean	0.299	0.362	0.475	0.470	0.463	0.433	0.126	0.096	2.47E+20
Std	0.208	0.234	0.266	0.259	0.253	0.242	0.150	0.131	1.63E+20
Maximum	0.834	0.937	1.098	1.097	1.089	1.054	0.646	0.586	7.00E+20
Minimum	0.002	0.004	0.015	0.024	0.032	0.024	0.000	0.000	1.00E+19
					Model Ed				
Mean	0.312	0.370	0.494	0.473	0.462	0.429	0.115	0.081	2.46E+20
Std	0.222	0.248	0.281	0.266	0.259	0.249	0.151	0.128	1.66E+20
Maximum	0.887	0.988	1.124	1.084	1.082	1.050	0.661	0.571	7.00E+20
Minimum	0.001	0.002	0.014	0.023	0.028	0.026	0.000	0.000	9.00E+18
					***in-situ* Lu**				
Mean	0.0025	0.0032	0.0050	0.0045	0.0041	0.0034	0.0002	0.0002	1.94E+18
Std	0.0018	0.0022	0.0030	0.0026	0.0024	0.0022	0.0003	0.0003	1.20E+18
Maximum	0.0082	0.0107	0.0142	0.0122	0.0126	0.0133	0.0027	0.0019	6.00E+18
Minimum	1.60E-05	1.61E-05	6.90E-05	1.18E-04	1.62E-04	1.57E-04	2.69E-06	4.47E-06	5.00E+16
					Model Lu				
Mean	0.0030	0.0033	0.0045	0.0037	0.0040	0.0032	0.0001	0.0001	1.79E+18
Std	0.0026	0.0026	0.0029	0.0021	0.0021	0.0017	0.0002	0.0001	1.08E+18
Maximum	0.0128	0.0127	0.0139	0.0109	0.0102	0.0091	0.0016	0.0009	5.00E+18
Minimum	5.60E-06	7.98E-06	6.41E-05	1.13E-04	2.25E-04	1.48E-04	9.30E-07	5.90E-07	6.00E+16

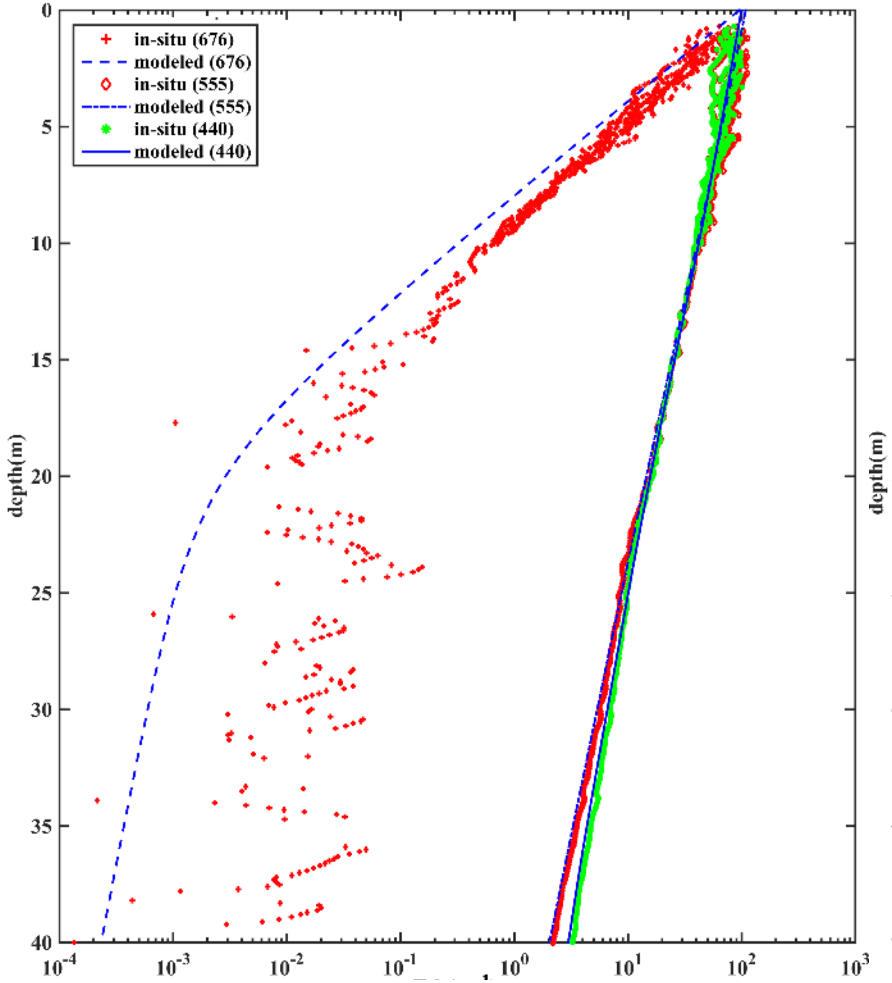

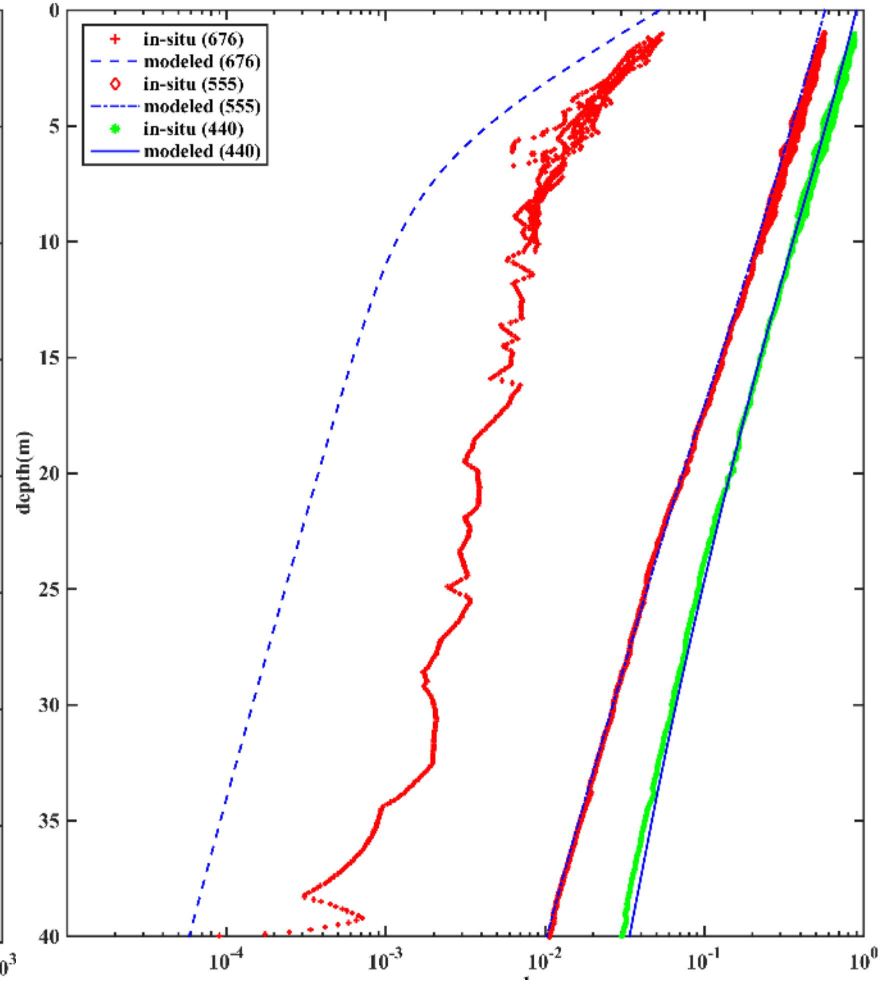

Figure 4.32 A. Representation in-situ and modeled profile of an example station's downward irradiance profile (Wm^{-2}); B. Representation in-situ and modeled profile of the same example station's upward radiance profile (Wm^{-2}).

The E_d comparison shows better correlation than Lu's comparison. The highest correlation, 0.97 was observed in Ed's comparison at 555 and 650 nm, while the lowest correlation, 0.74, was observed in Lu's comparison at 676 nm. Mean errors of the outputs of the model were very low for each variable; however, range of the errors show there were no biases in estimation. When compared the mean of the data set and the error, the lowest mean error was observed at PAR in Ed and at 532 nm in Lu, while the highest mean error was observed at 676 nm for both, Ed and Lu (Table 4.13). A simple regression was forced through zero between estimated values and *in-situ* data to evaluate ratio of modeled and *in-situ* values. Significant regression coefficients were observed for all comparisons. Ratios between modeled and *in-situ* values were around 1 with a range between 0.7 and 2.4. The ratios in Ed were extremely close to 1 with pretty high regression coefficients from 0.92 to 0.99. The ratios in Lu were generally around 1 with a decreasing trend of the ratios from long wavelength to shorter wavelengths. Ratio deviates more in longer wavelengths (at 650 and 676). This may be the result of inelastic scattering addition to Raman scattering which model configuration takes only into account. However, PAR ratio was also very close to 1 in Lu (Table 4.13). Comparison modeled and measured Ed and Lu are presented in Figure 4.33 and Figure 4.34, respectively.

Table 4.14 Resulting statistical comparison of Ed and Lu from *in-situ* and modeled by Ecolight.

Statistics	Wavelengths (nm)								
	412	440	488	510	532	555	650	676	PAR
	Ed								
Minimum error	-0.2593	-0.2621	-0.2217	-0.1950	-0.1624	-0.1399	-0.1023	-0.1262	-1.00E+20
Maximum error	0.1770	0.1677	0.2166	0.2038	0.2151	0.2177	0.1417	0.0962	1.00E+20
Mean error	0.0132	0.0083	0.0188	0.0036	-0.0012	-0.0040	-0.0108	-0.0142	-4.67E+17
Root mean square error	0.0673	0.0656	0.0676	0.0552	0.0493	0.0447	0.0280	0.0289	4.74E+19
Linear correlation (r)	0.95	0.97	0.97	0.98	0.98	0.98	0.99	0.98	0.96
Slope (in-situ/modeled)	0.9	1.0	1.0	1.0	1.0	1.0	1.0	1.1	1.0
R^2	0.92	0.93	0.95	0.96	0.96	0.97	0.97	0.96	0.92
	Lu								
Minimum error	-0.0024	-0.0031	-0.0043	-0.0044	-0.0037	-0.0042	-0.0014	-0.0012	-2.00E+18
Maximum error	0.0047	0.0037	0.0021	0.0011	0.0024	0.0020	0.0004	0.0000	1.00E+18
Mean error	0.0005	0.0001	-0.0005	-0.0008	-0.0001	-0.0002	-0.0001	-0.0002	-1.41E+17
Root mean square error	0.0013	0.0010	0.0012	0.0012	0.0009	0.0009	0.0002	0.0002	5.55E+17
Linear correlation (r)	0.92	0.93	0.93	0.95	0.93	0.92	0.91	0.85	0.89
Slope (in-situ/modeled)	0.7	0.9	1.1	1.2	1.0	1.1	1.6	2.4	1.1
R^2	0.86	0.87	0.88	0.90	0.85	0.83	0.84	0.74	0.82

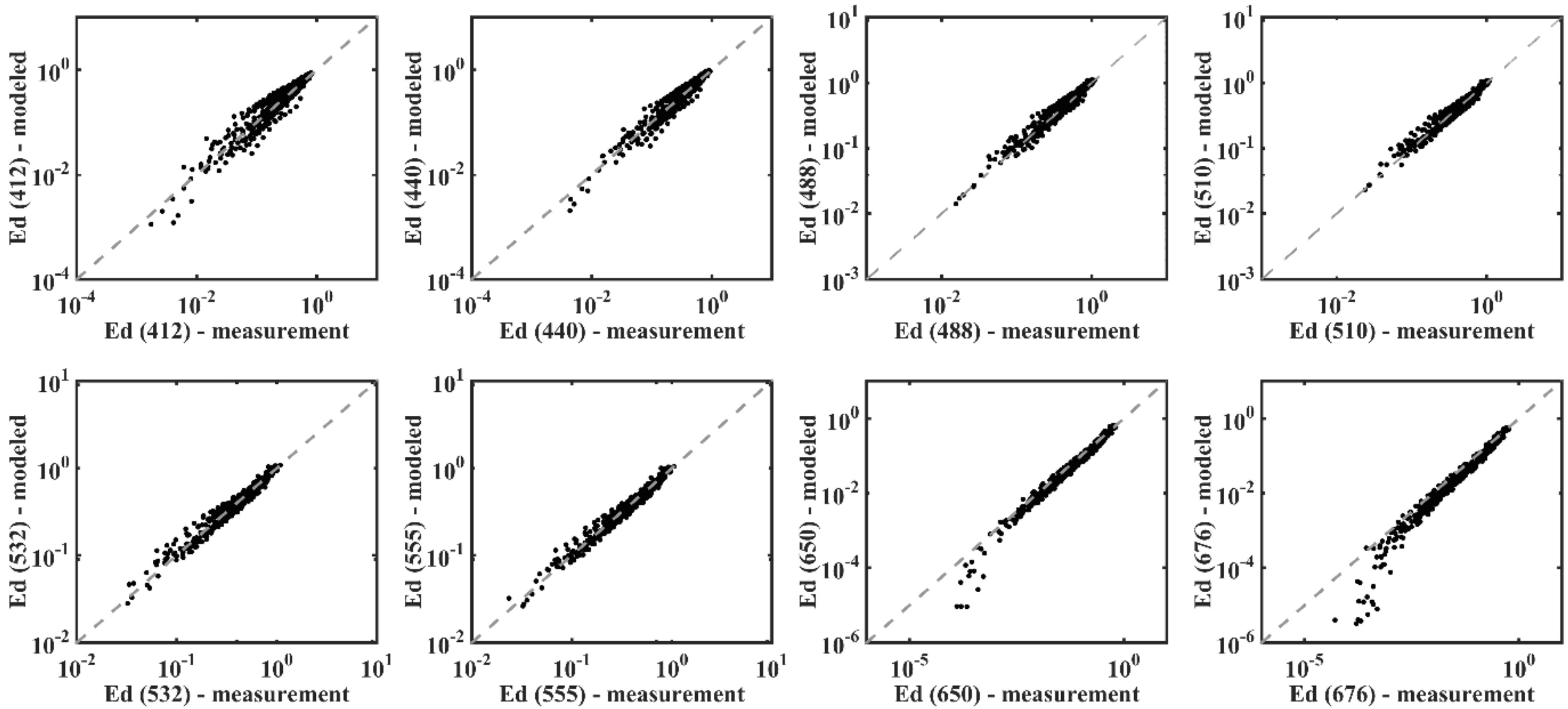

Figure 4.33 Relationship between measured downward irradiance and modeled downward irradiance at the wavelengths (m^{-1})

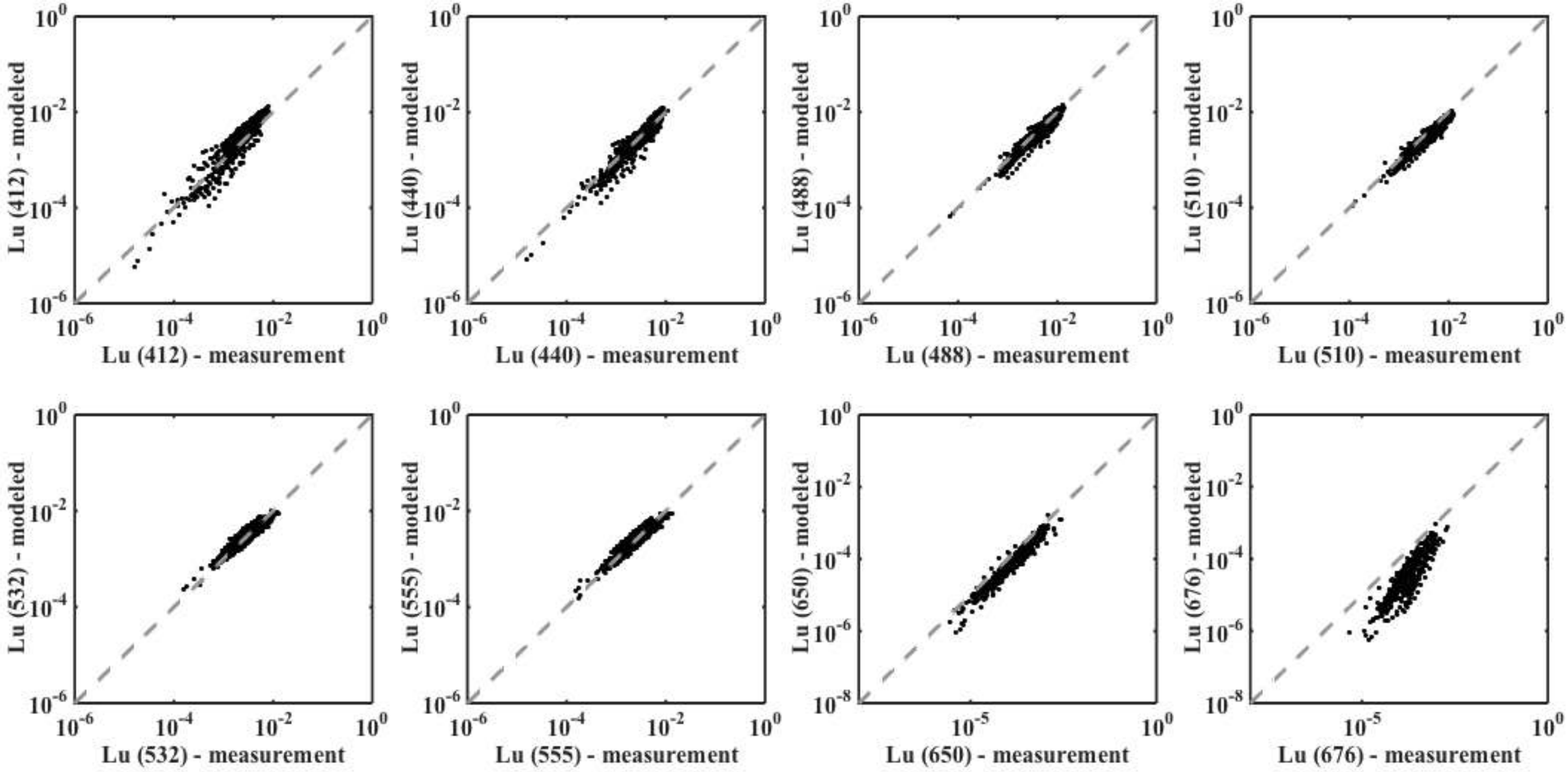

Figure 4.34 Relationship between measured upward radiance and modeled upward irradiance at the wavelengths (m^{-1})

Derived ratios between Lu and Ed in the wavelengths (water leaving radiance), also shows significant correlations with low average errors. Relatively lower correlation coefficients and error parameters are seen at longer wavelengths, 650 nm and 676 nm (r= 0.65; r=0.61, respectively), than other wavelengths (r between 0.84 and 0.96) due to deviation of inelastic scattering in Lu. Effect of the inelastic scattering happens in depths higher than 15 meters. Since water leaving radiance are important for ocean color remote sensing, this deviation can be eliminated because of using water leaving radiance and remote sensing reflectance for ocean color purposes. Water leaving radiance and remote sensing reflectance of some stations are given in Figure 4.35.

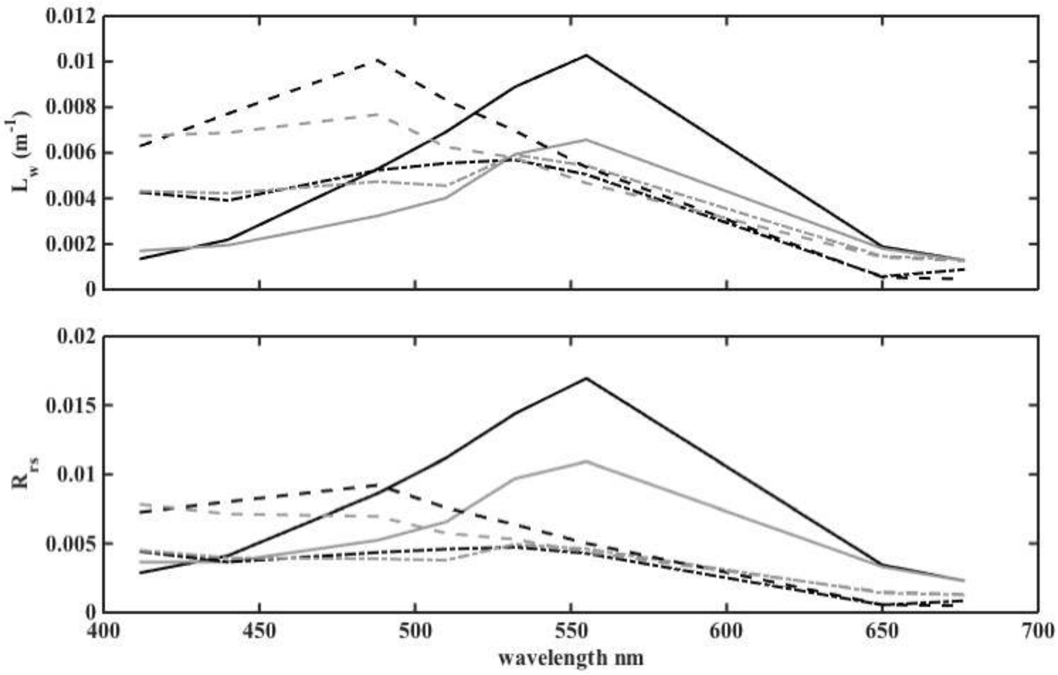

Figure 4.35 Water leaving radiance (W m^{-2}) (upper panel) and Remote sensing reflectance (lower panel) at spectrum for some example stations.

The PAR values from the profiles, which have significant correlation and low errors in the results (see example for PAR comparison, Figure 4.36), were used to calculate 1% and 10% light depths (euphotic and mid-euphotic depths, respectively). Results from measurements and model outputs showed significant correlations and low errors. Maximum error was 6 meter in euphotic depth, while in mid-euphotic depth maximum error was 8 meter between calculated depths of the model and *in-*

situ. As seen in Figure 4.37, the comparisons disperse 1:1 line in both, euphotic and mid-euphotic depths. This situation indicates that distribution of light fields in water column estimates with low errors.

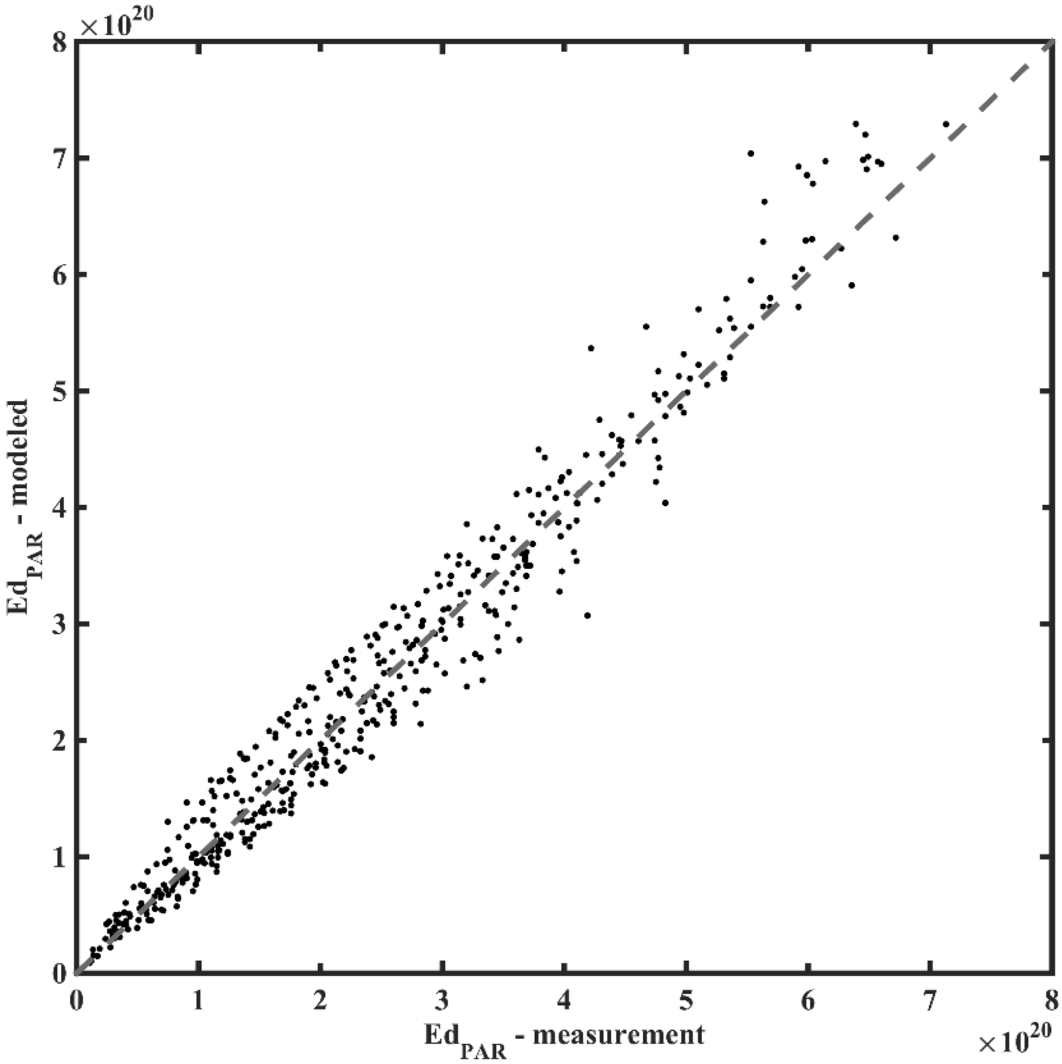

Figure 4.36 Comparison of modeled and *in-situ* Ed_{PAR} in depths of stations.

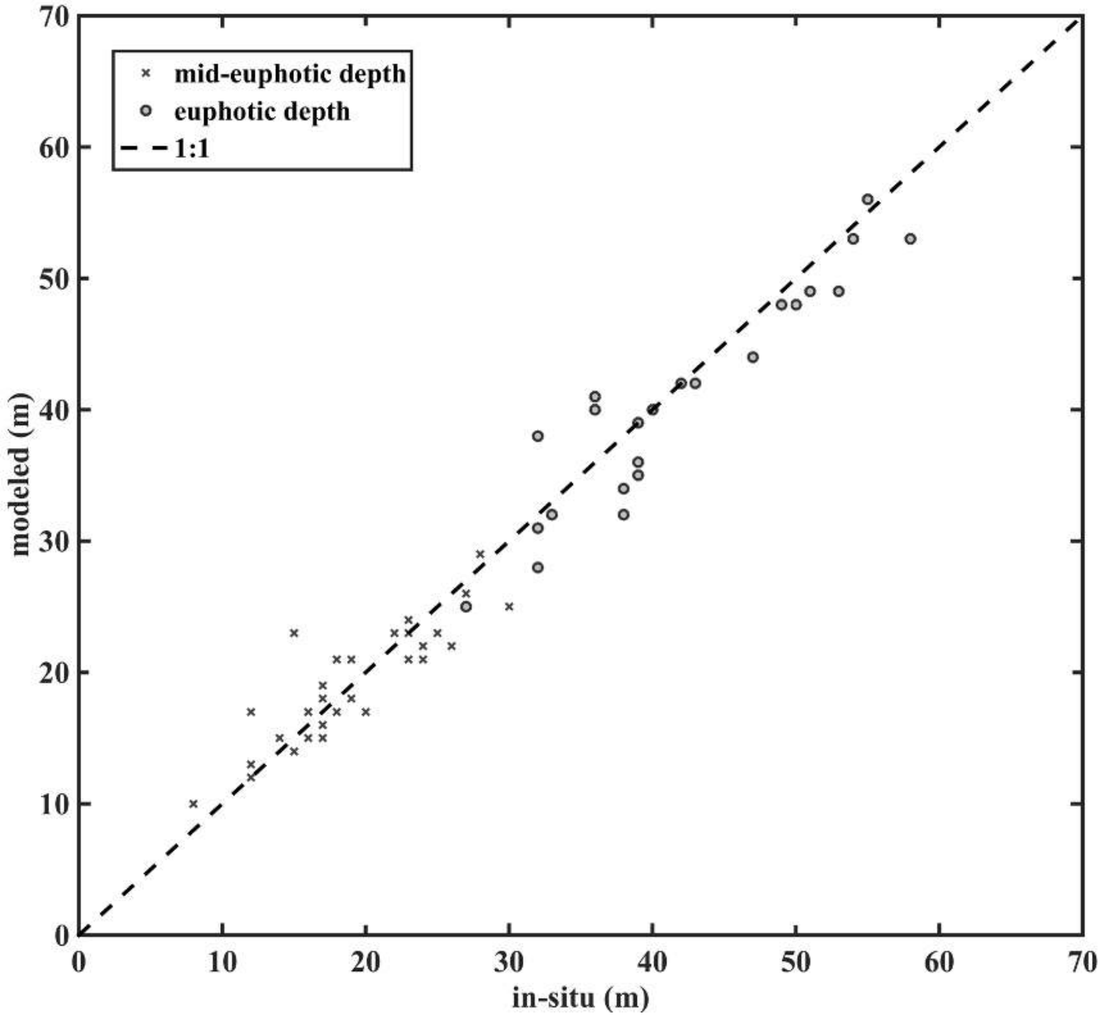

Figure 4.37 Comparison of modeled and *in-situ* euphotic and mid-euphotic zone depth in stations.

CHAPTER FIVE
DISCUSSION AND CONCLUSION

5.1 Oceanography of the Ligurian Sea

The *in-situ* measurements and meteorological records indicate that wind mixing had occurred in the Ligurian Sea in the middle of the cruise period. As parallel to the literature knowledge (Raick et al., 2005), late winter-early spring is the season for wind induced vertical mixing and this event is the reason for the spring bloom due to availability of the nutrients that rise into the euphotic zone in the Ligurian Sea. Deeper thermocline or straight vertical profiles in physical variables are evident of this fact. It should also be noted that colder surface water is not only the result of wind mixing, but also freshwater input from rivers. The input affects the variation in salinity and density in both horizontal and vertical distributions in coastal region, as offshore region has higher salinity and density than coastal region. As mentioned in previous studies (Sournia et al., 1990; Picco et al., 2010), zonal water distinction was observed in the cruise period between onshore and offshore region. All these physical characteristics of the Ligurian Sea can be observed by variables that are derived remotely from satellite images. The images make it available to completely see the distributions of sub-mesoscale structures in the area as well as supporting the results of physical properties.

5.2 Optical Properties of the Ligurian Sea

Due to limited number of data of this high ratio cluster (out of 90% quartile of the dataset), further analysis was not possible for this group. Such high values of the ratio might be local by re-suspension or terrestrial input shallow stations, increased ratio in Figure 5.2 indicates the re-suspension impact on some stations. The study by McKee & Cunningham (2006) also found/reported a separation coefficient of 0.330 for highly mineral dominated Case 2 water of Irish Sea. The separation value of the ratio found by McKee & Cunningham (2006) was between the separation value and 90% quantile value of this study (0.175 and 0.425, respectively). Further studies that will be designed for fresh water input and near coastal water (re-suspension) can help detail analysis to define this water type in the region. The studies on the phytoplankton communities in the Ligurian Sea and adjacent sea have pointed out different phytoplankton communities in zones of the Ligurian Sea. The study by Ruggieri et al., (2006) on the coast of the eastern Ligurian Sea reported chain-forming diatoms are the main group in spring bloom in February-March. Gomez & Gorsky (2003) reported silicoflagellates are the dominant group in the northwestern coast of the Ligurian Sea, due to colder temperatures in the winter. Bonomo et al., (2014) reviewed extensiv0ely the annual dynamics of coccolithophore taxa in the Mediterranean Sea and mentioned seasonally controlled production of coccolithophores. Knappertsbusch (1993) represented that the species number belonging to coccolithophore taxa increases rapidly during winter due to their growth strategy and higher nutrient concentrations related to wind mixing (and also the existence of the taxa in the central-southern Tyrrhenian Sea, which is the main source for coastal waters of the Ligurian Sea. The studies on the phytoplankton communities of the central zone of the Liguarian Sea are concentrated on time series data of the DYFAMED buoy. As a result of their nine year analysis Marty et al., (2002) showed a maximal contribution of the nanoflagellates in March in the central zone of the Ligurian Sea. Bethoux, Morin, & Ruis-Pino (2002) mentions a shift of phytoplankton from diatom-dominated ecosystem towards a non-siliceous one due to increases and ratio changes of nutrients since the early '60s. These literatures are in consistency with the results of the study. The coastal population with high backscattering can be dominated by species with calcareous and silicate plates due to relatively lower backscattering nutrient available, while central zone has non-siliceous species. Figure 5.1 presents the relationship between b_p and b_{bp} at 555 nm for the clusters. Higher backscattering ratio trends in cluster 2 (R=1) than cluster 1 (R=0.96)) which also indicates different particle communities in the clusters. This difference might be due to some specific phytoplankton taxonomic/taxon groups covered with calcareous or silicate plates such as coccolithophores and diatoms as well as other particles that are different than algal groups. These taxa have higher backscattering ratio than other phytoplankton taxa without plates, which have inorganic plates that cover the cell or cell-chains. Analysis on specific absorption by phytoplankton showed no differences between the clusters, thus it is not possible to say specifically that there are two different community of phytoplankton based on the specific absorption of the phytoplankton.

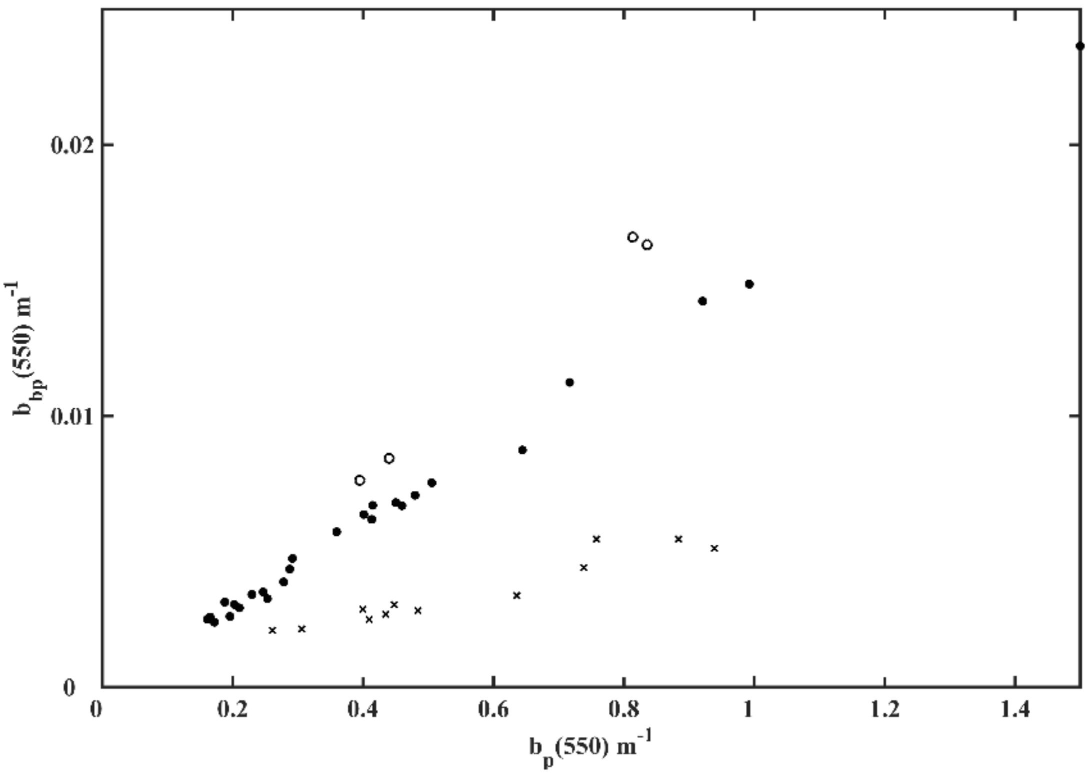

Figure 5.1 Relationship between b_p and b_{bp} at 550 nm. crosses show low ratio cluster (<0.175), circles show high ratio cluster (>0.175 and dots show the out of 0.9 quantile value (>0.425) of the dataset.

Separation coefficient and the 90% quantile value of the dataset was applied to vertical distribution of the ration of b_{bp} (676) and absorption (676) (Figure 5.2). As seen in the figure, the separation is distinctive in the upper layer, while the clusters unit each other and become as one population around 50 meters. Analysis on dataset of apparent optical properties showed that maximum euphotic depth is 57 meters in the dataset. Similarity in distribution between the 1% light zone and particle community properties was also supports that the zones of the Ligurian Sea have different particle communities.

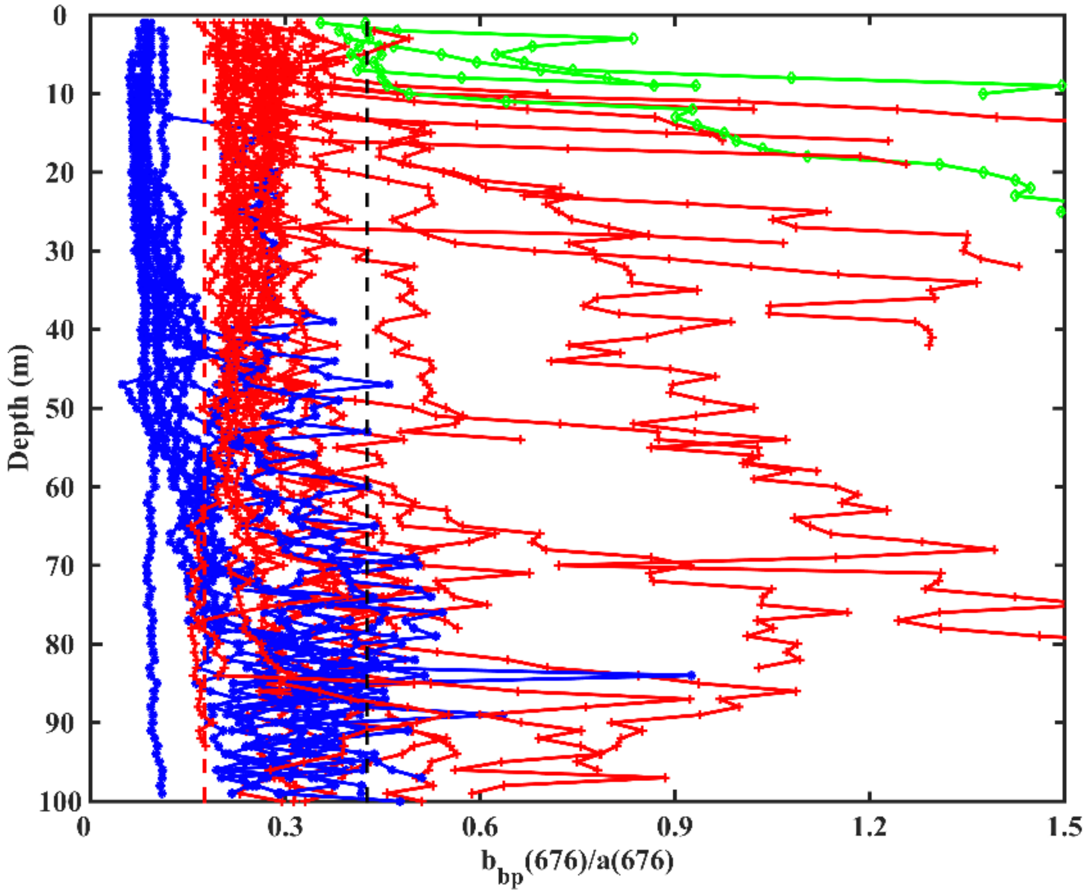

Figure 5.2 Vertical distribution of the ratio between b_{bp} and absorption at 676 nm. The light dashed line on The left shows separation coefficient, dark dashed line on the right shows the 90% quantile of the dataset.

Comparison of the results of coefficients of K_{bio} with global coefficients from Morel & Maritorena (2001) and local coefficients from Velluci (2007) are presented in Figure 5.3 for first optical depth, for euphotic zone Figure 5.4. Results show, in first optical depth that regression coefficients of fits are not as good as in Velluci (2007), especially after 470 nm. Coefficients of $\chi(\lambda)$ are almost the same for both studies, except Velluci (2007)'s coefficients are slightly higher in blue region compared to other regions. Coefficients of $e(\lambda)$ show large deviation from short wavelengths to longer wavelengths. When regression coefficients are taken into account, Velluci (2007)'s coefficients have better results of best-fit analyses. Results for euphotic zone shows that the study and results of Velluci (2007) have the same pattern for both coefficients. Coefficients of $\chi(\lambda)$ are almost the same for Velluci (2007), while results of Morel & Maritorena (2001) are slightly higher in blue region, and lower in green region. Coefficients of e(λ) in the study show transition between global and regional coefficients. From 400 nm to 470, e(λ) gets closer to global coefficient, then again it gets closer to local coefficients after 470 nm. As seen in Velluci (2007), e(λ) has a sharp decrease in green region in respect to Morel& Maritorena (2001). When taking into account the regression coefficients, the present study coefficients areas are as good as in Morel & Maritorena (2001) and even better results for best-fit analyses.

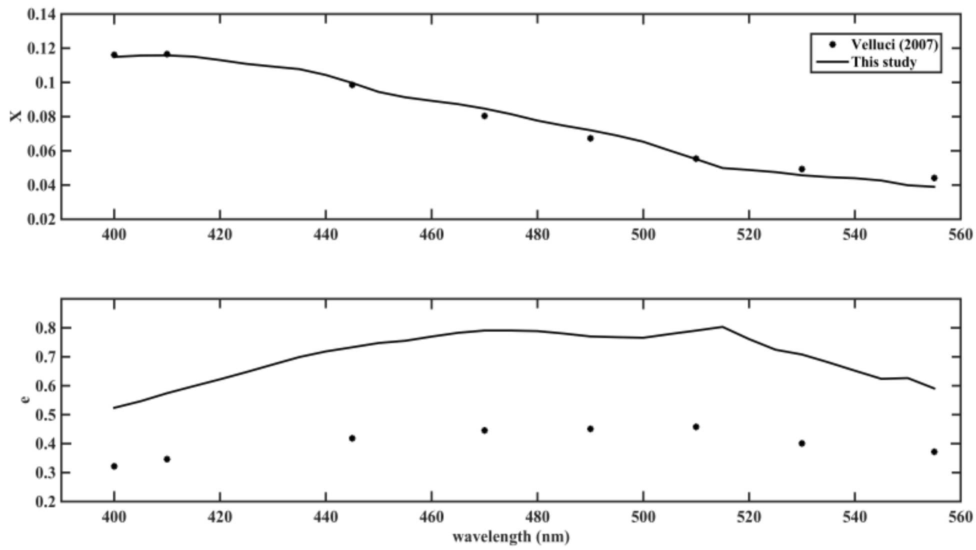

Figure 5.3 Coefficient e(λ) and χ(λ) in first optical depth.

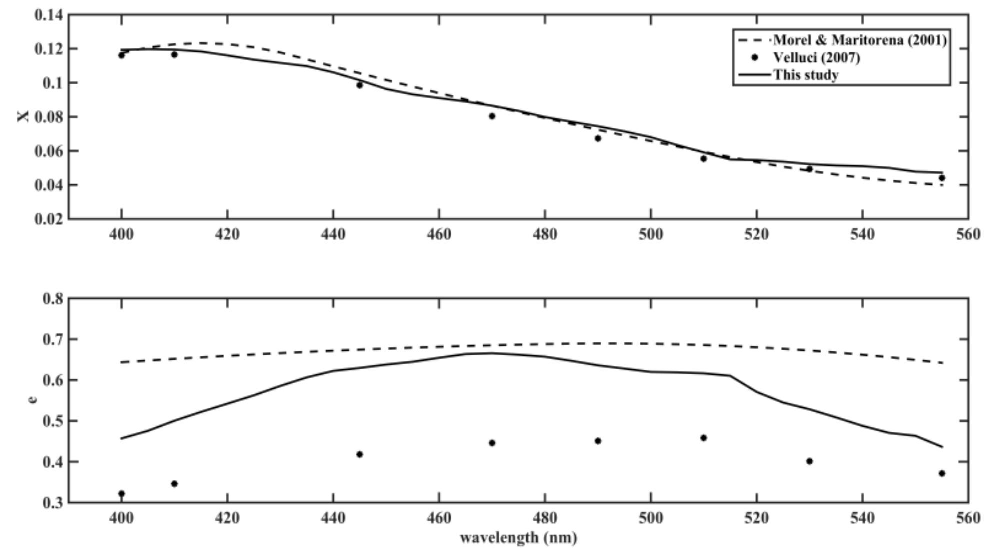

Figure 5.4 Coefficient e(λ) and χ(λ) in euphotic zone.

Applications of calculation of K_{bio} were done by using coefficients from mentioned studies to compare results. Minimum (0.4 µg/l) and maximum (2.8 µg/l) [Chl] concentrations in Case 1 dataset were used as representative for low and high trophic levels. As seen in Figure 5.5, derived coefficients in this study overestimate in the beginning and end regions of interested spectrum interval, while Velluci (2007)'s local coefficients overestimates through interested spectrum interval than global coefficients in low concentration. Oppositely, derived coefficients in this study underestimates the beginning and end regions of interested spectrum interval, while Velluci (2007)'s local coefficients underestimate more in all interested spectrum interval than global coefficients in high concentration.

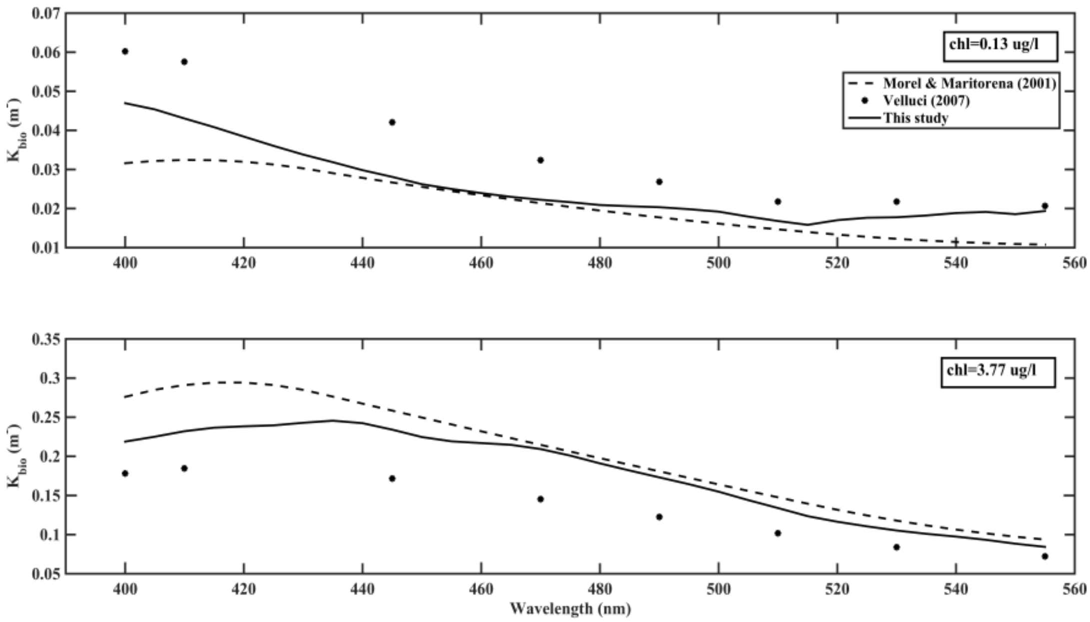

Figure 5.5 Kd distribution at spectrum in low and high [Chl] concentrations.

5.4 Improving the Bio-optical Model for the Ligurian Sea.

The integrated Case 1 and Case 2 Ligurian Sea bio-optical model developed here has been shown to provide an effective characterization of the optical properties of the region. In doing so, it is worth considering the various stages of model development that have been incorporated into the validation scheme. Although the Case 1 elements of the bio-optical model are relatively standard, Case 2 section contains several innovations including statistical partitioning of TSS and derivation of partial IOPs for non-biogenic particles. It also includes a separation of CDOM contributions from biogenic (effectively phytoplankton) and non-biogenic (freshwater) sources. A scheme for partitioning the region into Case 1, Case 2 (non-biogenic particles) and Case 2 (freshwater influence) zones based on Chl, TSS and Salinity values has been presented which is essential for correctly selecting the appropriate bio-optical model for any given point in space. It is also worth emphasizing that the performance of the model has been demonstrated using proxy values of Chl and TSS derived from in situ fluorescence and turbidity measurements, which introduces another set of measurement uncertainties into the analysis. The resulting comparisons with in situ IOP data are therefore particularly encouraging given this added layer of data manipulation.

The utility of this bio-optical model for predicting underwater and water-leaving light fields has been tested through rigorous optical closure analysis against *in situ* and remotely sensed radiometry and AOPs. When considering the level of performance achieved, it should be recognized that direct optical closure between *in situ* IOPs and radiometry remains elusive and poorly demonstrated to date. The degree of closure demonstrated here is therefore very encouraging and suggests that major features of the optical characteristics of the region have been satisfactorily captured in the bio-optical model.

Results and analysis show that the model performs accurately in each step from bio-geochemical to the radiance fields. Model results show overestimation in low values, especially in scattering and backscattering, in addition to the radiance fields in red region as a result of inelastic scattering effect. Sensitivity analysis of the instruments that were used for model calibration point out that such small values may be effect result of uncertainty of the instrument. On the other hand, there are many conversions that how to apply the datasets from sensors of fluorescence and turbidity to the radiance fields retrieved by radiative transfer modeling as well as empirical relationships, such as between biogeochemical and bio-optical variables. These relationships may be another effect for lower accuracy in lower values of the datasets. Percentage error distributions of calculated PAR values from *in-situ* and estimated data are given in Figure 5.6a. Most of the percentages of difference are located near 0, while 4% data points (a total of 452 data points)show larger than 40 %. Euphotic depths, as derivation of PAR values in vertical distribution, were calculated with model and light distribution approaches of previous ecosystem models (Raick et al., 2005; Lacroix & Nival, 1998; Lacroix & Gregoire, 2002) that were conducted in the Ligurian Sea. Differences between calculated euphotic depths from *in-situ* data and different approaches are given in Figure 5.6b. Narrow anomaly belongs to the IOP model that was implemented in this study with a range between +6 meter and -6 meter. Light distribution approach that was used by Lacroix & Gregoire (2002) has better performance than the other two approaches. Even though the modeled PAR dataset has few high errors in percentage, euphotic depth calculations showed very wide deviation from *in-situ* values and improved the estimated euphotic depth values compared to the other approaches that were used in previous studies.

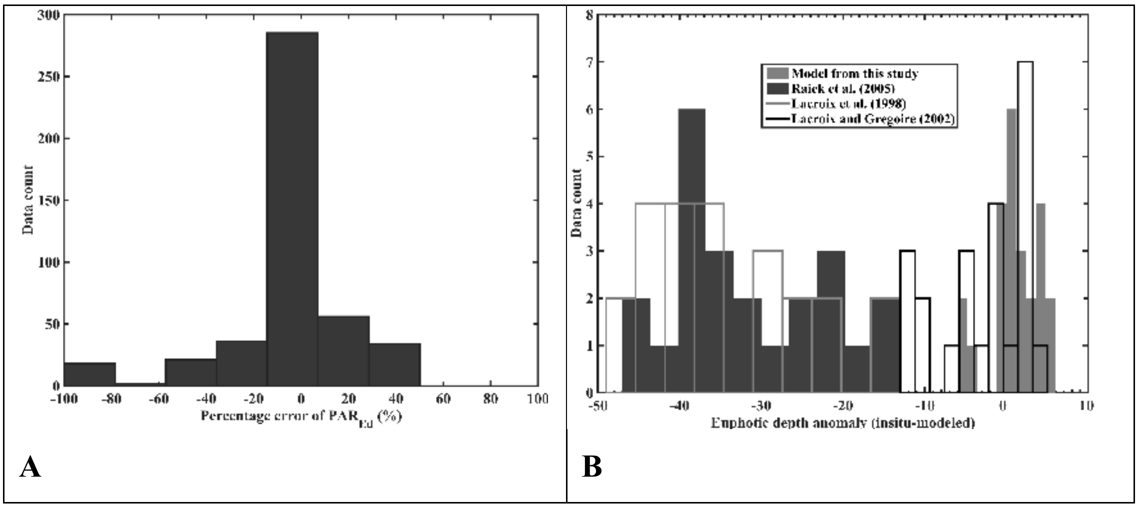

Figure 5.6 A. Anomaly of modeled PAR_{Ed} values from the *in-situ* values; B. Anomaly of model euphotic zone depths of the model and approaches of previous study from the in-situ euphotic zone depths.

+

Another comparison was applied to understand how accurately the improved model estimates percentages of light distribution in vertical profiles. The model deviates from percentages *in-situ* light distribution less than 20% maximum, as the other approaches have deviation more than 40% maximum (Figure 5.7). Results and comparison with the other approaches from previous studies indicate that the light model presented in this study achieved light distribution based on biogeochemical variables as well as euphotic zone depth more accurately than previous approaches.

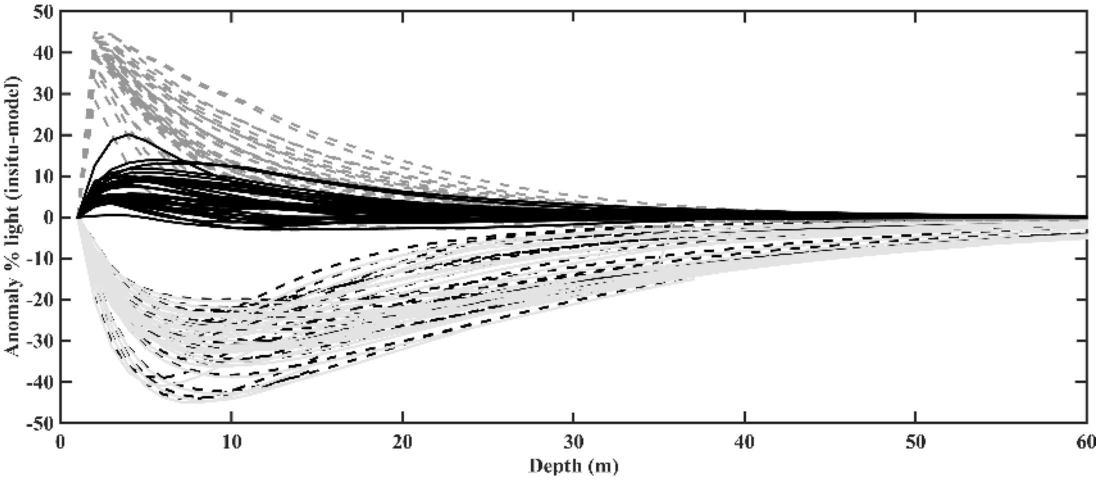

Figure 5.7 Anomaly of modeled light percentage from in-situ light percentages at depth. Solid black line shows results of model from this study; dashed black line is for results of Lacroix et al. (1998); solid grey line shows results from Raick et al (2005); dashed grey line is for Lacroix and Gregoire (2002).

Results did not show any significant difference between onshore and offshore stations. Performance of the model is almost the same for both regions. This fact is better progress for the model as to previous approach of Lacroix & Gregoire (2002). Figure 5.8 shows euphotic zone depth calculations from *in-situ*, the improved model and the approach of Lacroix & Gregoire (2002) in each station groups, based on regions. As seen in the figure, while the literature approach showed good performance in offshore region, it did not show good performance for inshore region with overestimation by not taking into account other colored components other than phytoplankton. The model showed better and similar performance than the other approach in both regions. When the other colored components are taking into account with CDOM indirectly from salinity and other particles, e.g. minerals, TSS concentrations improved the performance for estimations of euphotic zone depth for in-shore region.

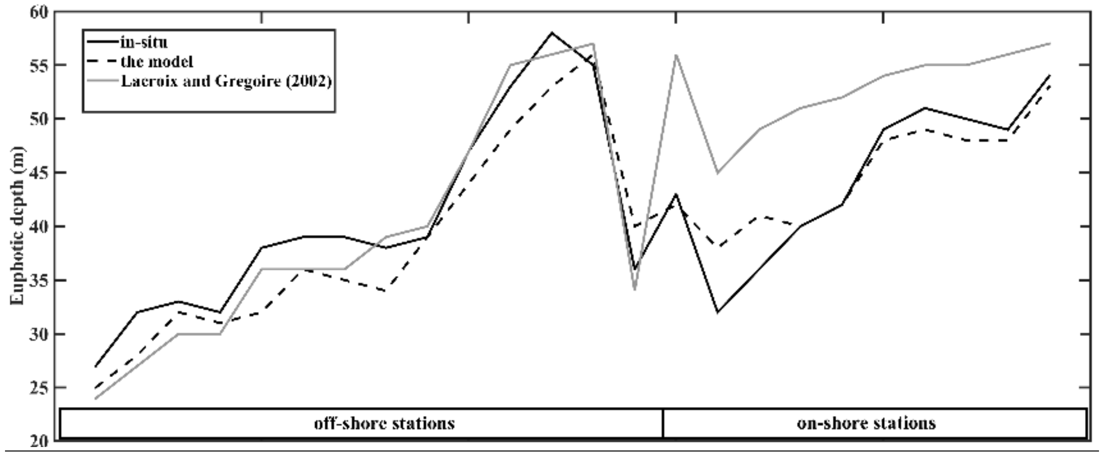

Figure 5.8 Comparison in-situ, modeled and approach of Lacroix and Gregoire (2002) euphotic zone depth distributions of in off-shore and onshore stations.

Input variables of the improved model are easy to obtain from coupled physical-ecosystem models. All coupled physical-ecosystem models include salinity and chlorophyll-a variables. As well as TSS can be used as state variable for ecosystem models (e.g., Everett, Baird, & Suthers,F 2007) or obtain with coupled sediments transport models (Sheng & Kim, 2009). The coupled physical-ecosystem models with sediment transport model will help to obtain more accurate underwater light fields by taking into account re-suspension and particle inputs from rivers. TSS is also a variable that might be estimated by using remotely sensed data from different sensors (for instance, Klemas, Borchhardt, & Treasure (1974) from Landsat, Stumpf & Pennock (1989) from AVHRR, Froidefond et al. (2002), Binding, Bowers, & Mithelsen-Jacob (2003) and Binding, Bowers, & Mithelsen-Jacob (2005) from SeaWIFS, Miller & McKee (2004) from MODIS). This ability for the variable is an advantage for data assimilation purpose of the modeling.

5.5 Conclusion

Physical and bio-optical data were analyzed in the Ligurian Sea to represent bio-optical characterization of the Ligurian Sea as a part of Mediterranean Sea in highly productive season and water types were identified. Physical measurements showed two distinctive zones in the Ligurian Sea, central and coastal zone, as parallel to the common knowledge of the Ligurian Sea. Bio-optical measurements indicated two distinctive particulate populations, which define bio-optical water types in the Ligurian Sea with agreement with physical properties. Offshore region showed Case 1 water characteristics with dominancy of Phytoplankton, while onshore region showed Case 2 water characteristics with contribution of other optically active components.

Based on the bio-optical characterization, a bio-optical model was developed to represent characterization of bio-optical properties of the Ligurian Sea. This is an important step for establishing a conceptual framework to integrate a robust bio-optical model into future coupled physical-ecosystem models for this region. Case 1 type waters of the Ligurian sea are required chlorophyll to estimate IOPs, Case 2 type waters of the Ligurian sea are required non-biogenic total suspended solids (for non-algal particulates) and salinity (for non-biogenic colored dissolved organic matter) in addition to chlorophyll.

The integrated offshore and coastal Ligurian Sea bio-optical model developed here has been shown to provide an effective characterization of the optical properties of the region. The utility of this bio-optical model for predicting underwater and water-leaving light fields has been tested through rigorous optical closure analysis against in situ AOPs. The degree of closure demonstrated here suggests that major features of the optical characteristics of the region have been satisfactorily captured in the bio-optical model. Validation results showed that our model is superior to the previous models due to the inclusion of non-biogenic material in addition to biogenic material.

The Ligurian Sea bio-optical model developed has been specifically designed to be able to accommodate a wide variety of potential data sources and to integrate into ecosystem models with minimal need for adaptation.

REFERENCES

Aguirre-Gomez, R., Weeks, A. R., & Boxall, S. R. (2001).The identification of phytoplankton pigments from absorption spectra. *International Journal of Remote Sensing*, *22*(2), 315–338. http://doi.org/10.1080/014311601449952.

Astraldi, M., & Gasparini, G. P. (1992).The seasonal characteristics of the circulation in the north Mediterranean basin and their relationship with the atmospheric-climatic conditions .*Journal of Earth System Science*, *97*(C6), 9531–9540.

Astraldi, M., Gasparini, G. P., Manzella, G. M. R., & Hopkins, T. S. (1990).Temporal variability of currents in the eastern Ligurian Sea. *Journal of Geophysical Research*, *95*(C2), 1515–1522.

Babin, M., Stramski, D., Ferrari, G. M., Claustre, H., Bricaud, A., Obolensky, G., et al. (2003).Variations in the light absorption coefficients of phytoplankton, nonalgal particles, and dissolved organic matter in coastal waters around Europe. *Journal of Geophysical Research*, *108*(C7), 3211. http://doi.org/10.1029/2001JC000882.

Barlow, R. G., Aiken, J., Holligan, P. M., Cummings, D. G., Maritorena, S., & Hooker, S. (2002). Phytoplankton pigment and absorption characteristics along meridional transects in the Atlantic Ocean. *Deep-Sea Research Part I: Oceanographic Research Papers*, *49*(4), 637–660. http://doi.org/10.1016/S0967-0637(01)00081-4.

Beşiktepe, Ş. ¸ T., Lermusiaux, P. F. J., & Robinson, A. R. (2003). Coupled physical and biogeochemical data-driven simulations of Massachusetts Bay in late summer: Real-time and post cruise data assimilation. *Journal of Marine Systems*, *40-41*, 171–212. http://doi.org/10.1016/S0924-7963(03)00018-6.

Béthoux, J. P., Morin, P., & Ruiz-Pino, D. P. (2002). Temporal trends in nutrient ratios: Chemical evidence of Mediterranean ecosystem changes driven by human activity. *Deep-Sea Research Part II: Topical Studies in Oceanography*, *49*(11), 2007–2016. http://doi.org/10.1016/S0967-0645(02)00024-3.

Bidigare, R., Schofield, O., & Prezelin, B. (1989). Influence of zeaxanthin on quantum yield of photosynthesis of synechococcus clone WH7803 (DC2). *Marine Ecology Progress Series*, *56*, 177–188.http://doi.org/10.3354/meps056177.

Binding, C. E., Bowers, D. G., & Mitchelson-Jacob, E. G. (2003).An algorithm for the retrieval of suspended sediment concentrations in the Irish Sea from SeaWiFS ocean color satellite imagery. *International Journal of Remote Sensing*, *24*(19), 3791–3806. http://doi.org/10.1080/0143116021000024131.

Binding, C. E., Bowers, D. G., & Mitchelson-Jacob, E. G. (2005). Estimating suspended sediment concentrations from ocean color measurements in moderately turbid waters: The impact of variable particle scattering properties. *Remote Sensing of Environment*, *94*(3), 373–383. http://doi.org/10.1016/j.rse.2004.11.002.

Bonomo, S., Cascella, A., Alberico, I., Ferraro, L., Giordano, L., Lirer, F., et al. (2014). Coccolithophores from near the Volturno estuary (central Tyrrhenian Sea). *Marine Micropaleontology*, *111*, 26–37. http://doi.org/10.1016/j.marmicro.2014.06.001.

Bowers, D. G., Harker, G. E. L., Smith, P. S. D., & Tett, P. (2000). Optical properties of a region of freshwater influence (the Clyde Sea). *Estuarine Coastal and Shelf Science*, *50*, 717–726.

Bricaud, A., Morel, A., Babin, M., Allali, K., & Claustre, H. (1998). Variations of light absorption by suspended particles with Chlorophyll a concentration in oceanic (case 1) waters: analysis and implications of bio-optical models. *Journal of Geophysical Research*, *103*(C13), 31033–31044.

Bricaud, A., Roesler, C., & Zaneveld, J. R. V. (1995). In situ methods for measuring the inherent optical properties of ocean waters. *Limnology and Oceanography*, *40*(2), 393–410. http://doi.org/10.4319/lo.1995.40.2.0393.

Ciavatta, S., Torres, R., Martinez-Vicente, V., Smyth, T., Olmo, G. D., Polimene, L., et al. (2014).Progress in oceanography assimilation of remotely-sensed optical properties to improve marine biogeochemistry modelling. *Progress in Oceanography*, *127*, 74–95.

Cleveland, J. S., & Sundman, L. K. (1993). Quantifying absorption by aquatic particles: A multiple scattering correction for glass-fiber filters. *Limnology and Oceanography*, *38*(6), 1321–1327.

Colella, S. (2006) .*La produzioneprimarianel mar Mediterraneo da satellite : Sviluppo di un modello regionale e suaapplicazione aidati SeaWiFS , MODIS e MERIS*. PhD Thesis, University of Napoli "Federico II", Naples.

Dickey, T. D., & Falkowski, P. G. (2002). *Solar energy and its biological – physical interactions in the sea*. (A. R. Robinson, J. J. McCarthy, & R. B. J., Eds.) *The Sea* (Vol. 12). New York: John Wiley & Sons, Inc.

Dickey, T., Lewis, M., & Chang, G. (2006). Optical oceanography: recent advances and future directions using global remote sensing and in situ observations. *Reviews of Geophysics*, *44* (2003), 1–39. http://doi.org/10.1029/2003RG000148.1.INTRODUCTION.

Esposito, A., & Manzella, G. (1982). Current circulation in the Ligurian Sea. In *J Nihoul (Ed.), Hydrodynamics of semi-enclosed seas, Elsevier Scientific Publishing Company, Amsterdam* (pp. 187–203).

Everett, J. D., Baird, M. E., & Suthers, I. M. (2007). Nutrient and plankton dynamics in an intermittently closed/open lagoon, Smiths Lake, southeastern Australia: An ecological model. *Estuarine, Coastal and Shelf Science*, *72*(4), 690–702. http://doi.org/10.1016/j.ecss.2006.12.001.

Gomez, F., & Gorsky, G. (2003).Annual microplankton cycles in Villefranche Bay, Ligurian Sea, NW Mediterranean. *Journal of Plankton Research*, *25*(4), 323–339.

Froidefond, J. M., Lavender, S., Laborde, P., Herbland, A., & Lafon, V. (2002). SeaWiFS data interpretation in a coastal area in the Bay of Biscay. *International Journal of Remote Sensing*, *23*, 881–904.

Fujii, M., Boss, E., & Chai, F. (2007). The value of adding optics to ecosystem models : A case study. *Biogeoscience*, *4*, 817–835.

Gordon, H. R., & Morel, A. (1981). Water color measurements - an introduction. *Marine Science*, *13*(Oceanography from Space), 207–212.

Gregoire, M., & Oğuz, T. (2009). Modeling biogeochemical processes in marine ecosystems. In C. T. A. Nihoul, J. C. J., Chen (Ed.), *Oceanography encyclopedia of life support systems (EOLSS)* (p. Vol III). Oxford: Eolss Publishers.

Hoepffner, N., & Sathyendranath, S. (1991). Effect of pigment composition on absorption properties of phytoplankton. *Marine Ecology Progress Series*, *73*, 11–23. http://doi.org/10.3354/meps073011.

Kirk, J. T. O. (2011). *Light and photosynthesis in aquatic ecosystems*. *Cambridge University Pr ess* (3rd ed.). Cambridge: Cambridge University Press. http://doi.org/10.1016/0304-3770(95)90010-1.

Klemas, V., Borchardt, J. F., & Treasure, W. M. (1973). Suspended sediments observations from ERTS-1. *Remote Sensing of Environment*, *2*, 205–221.

Knappertsbusch, M. (1993). Geographic distribution of living and holocene coccolithophores in the Mediterranean Sea. *Marine Micropaleontology*, *21*(1), 219–247.

Lacroix, G., & Gregoire, M. (2002). Revisited ecosystem model (MODECOGeL) of the ligurian sea: seasonal and interannual variability due to atmospheric forcing. *Journal of Marine Systems*, *37*(4), 229–258. http://doi.org/http://dx.doi.org/10.1016/S0924-7963(02)00190-2.

Lacroix, G., & Nival, P. (1998). Influence of meteorological variability on primary production dynamics in the Ligurian Sea (NW Mediterranean Sea) with a 1D hydrodynamic/biological model. *Journal of Marine Systems*, *16*(1-2), 23–50. http://doi.org/10.1016/S0924-7963(97)00098-5.

Lazzara, L., Marchese, C., Massi, L., Nuccio, C., Maselli, F., Santini, C., et al. (2010).Sub-regional patterns of primary production annual cycle in the Ligurian and north Tyrrhenian seas, from satellite data. *Italian Journal of Remote Sensing*, *42*(2), 87–102. http://doi.org/10.5721/ItJRS20104227.

Lee, Z. P., Du, K. P., Arnone, R., Liew, S. C., & Penta, B. (2005). Penetration of solar radiation in the upper ocean: A numerical model for oceanic and coastal waters. *Journal of Geophysical Research*, *110*(9), 1–12. http://doi.org/10.1029/2004JC002780.

Loisel, H., & Morel, A. (1998). Light scattering and Chlorophyll concentration in case 1 waters: A re-examination. *Limnology and Oceanography*, *43*(5), 847–858. http://doi.org/10.4319/lo.1998.43.5.0847.

Marty, J. C., Chiavérini, J., Pizay, M. D., & Avril, B. (2002). Seasonal and inter-annual dynamics of nutrients and phytoplankton pigments in the western Mediterranean Sea at the DYFAMED time-series station (1991-1999).*Deep-Sea*

Research Part II: Topical Studies in Oceanography, *49*(11), 1965–1985. http://doi.org/10.1016/S0967-0645(02)00022-X.

McKee, D., & Cunningham, A. (2006). Identification and characterization of two optical water types in the Irish Sea from in situ inherent optical properties and seawater constituents. *Estuarine, Coastal and Shelf Science*, *68*(1), 305–316. http://doi.org/10.1016/j.ecss.2006.02.010.

McKee, D., Röttgers, R., Neukermans, G., Calzado, V. S., Trees, C., Ampolo-Rella, M., et al. (2014).Impact of measurement uncertainties on determination of Chlorophyll-specific absorption coefficient for marine phytoplankton. *Geophysical Research Oceans*, *119*, 9013–9025.

Miller, R. L., & McKee, B. A. (2004). Using MODIS terra 250 m imagery to map concentrations of total suspended matter in coastal waters. *Remote Sensing of Environment*, *93*, 259−266.

Mobley, C. D. (1994). *Light and water*. New York: Academic Press.

Mobley, C. D., Sundman, L. K., & Boss, E. (2002). Phase function effects on oceanic light fields. *Applied Optics*, *41*(6), 1035–1050.

Morel, A. (1974). Optical properties of pure water and pure seawater. In E. S. Jerlov N. G., Nielsen (Ed.), *Optical aspects of oceanography* (pp. 1–24). London and New York: Academic Press.

Morel, A. (1988). Optical modeling of the upper ocean in relation to its biogenous matter content (case 1 waters). *Journal of Geophysical Research, 93,* 10,749-10,768.

Morel, A. (2009). Are the empirical relationships describing the bio-optical properties of case 1 waters consistent and internally compatible? *Journal of*

Geophysical Research: Oceans, *114*(C01016), 1–15. http://doi.org/10.1029/2008JC004803.

Morel, A., & Berthon, J. F. (1989). Surface pigments, algal biomass profiles, and potential production of the euphotic layer: Relationships re-investigated in view of remote-sensing applications. *Limnology and Oceanography*, *34*(8), 1545–1562. http://doi.org/10.4319/lo.1989.34.8.1545.

Morel, A., & Maritorena, S. (2001). Bio-optical properties of oceanic waters : A reappraisal. *Journal of Geophysical Research*, *106*, 7163–7180.

Niewiadomska, K., Prieur, L., Ortenzio, F., Villefranche, D., Curie-paris, M., & Oce, L. (2008). Submesoscale physical-biogeochemical coupling across the Ligurian Current (Northwestern Mediterranean) using a bio-optical glider. *Limnology and Oceanography, 53*, 2210–2225.

Oceanopticsbook (n.d.). *Apparent optical properties*. Retrieved May 20, 2015, from http://www.oceanopticsbook.info/view/overview_of_optical_oceanography/apparent_optical_properties).

Pegau, W., Gray, D., & Zaneveld, J. (1997). Absorption and attenuation of visible and near-infrared light in water: Dependence on temperature and salinity. *Applied Optics*, *36*, 6035–6046.

Penta, B., Lee, Z., Kudela, R. M., Palacios, S. L., Gray, D. J., Jolliff, J. K., et al. (2008). An underwater light attenuation scheme for marine ecosystem models. *Optics Express*, *16*(21), 16581–16591.

Picco, P., Cappelletti, A., Sparnocchia, S., Schiano, M. E., Pensieri, S., & Bozzano, R. (2010). Upper layer current variability in the central Ligurian Sea. *Ocean Science*, *6*(4), 825–836. http://doi.org/10.5194/os-6-825-2010.

Pope, R. M., & Fry, E. S. (1997). Absorption spectrum (380-700 nm) of pure water, II. integrating cavity measurements. *Applied Optics*, *36*(33), 8710–8723. http://doi.org/10.1364/AO.36.008710.

Prieur, L., & Sathyendranath, S. (1981). An optical classification of coastal and oceanic waters based on the specific spectral absorption curves of phytoplankton pigments, dissolved organic matter, and other particulate materials. *Limnology And Oceanography*, *26*(4), 671–689. http://doi.org/10.2307/2836033.

Raick, C., Delhez, E. J. M., Soetaert, K., & Grégoire, M. (2005). Study of the seasonal cycle of the biogeochemical processes in the Ligurian Sea using a 1d interdisciplinary model. *Journal of Marine Systems*, *55*(3-4), 177–203. http://doi.org/10.1016/j.jmarsys.2004.09.005.

Roesler, C. S. (1998). Theoretical and experimental approaches to improve the accuracy of particulate absorption coefficients derived from the quantitative filter technique. *Limnology and Oceanography*, *43*(7), 1649–1660. http://doi.org/10.4319/lo.1998.43.7.1649.

Rothstein, L., Cullen, J., Abbott, M., Chassignet, E., Denman, K., Doney, et al. (2006). Modeling ocean ecosystems: The PARADIGM program. *Oceanography*, *19*(1), 22–51. http://doi.org/10.5670/oceanog.2006.89.

Röttgers, R., & Doerffer, R. (2007). Measurements of optical absorption by chromophoric dissolved organic matter using a point-source integrating-cavity absorption meter. *Limnology and Oceanography Methods*, *5*, 126–135.

Röttgers, R., Schönfeld, W., Kipp, P.R., & Doerffer, R. (2005). Practical test of a point-source integrating cavity absorption meter: The performance of different collector assemblies. *Applied Optics*, *44*, 5549–5560.

Ruggieri, N., Castellano, M., Misic, C., Gasparini, G., Cattaneo-Vietti, R., & Povero, P. (2006).Seasonal and interannual dynamics of a coastal ecosystem (Portofino, Ligurian Sea) in relation to meteorological constraints. In *Geophysical Research Abstracts* (p. 07774).European Geosciences Union.

Sanjuan-Calzado, V. (2009).*Bio-optical modeling for ecosystems in case II waters*. PhD Thesis, University of Southampton*,* Southampton.

Sheng, Y. P., & Kim, T. (2009). Skill assessment of an integrated modeling system for shallow coastal and estuarine ecosystems. *Journal of Marine Systems*, *76*(1-2), 212–243. http://doi.org/10.1016/j.jmarsys.2008.05.011.

Shulman, I., Frolov, S., Anderson, S., Penta, B., Gould, R., Sakalaukus, P., et al. (2013). Impact of bio-optical data assimilation on short-term coupled physical, bio-optical model predictions. *Journal of Geophysical Research: Oceans*, *118*(4), 2215–2230. http://doi.org/10.1002/jgrc.20177.

Smith, R. C., & Baker, K. S. (1981). Optical properties of the clearest natural waters (200-800 nm). Applied Optics, *20*(2), 177–184.

Sournia, A., Brylinski, J. M., Dallot, S., LeCorre, P., Leveau, M., Prieur, L., et al. (1990). Fronts hydrologiques au large des côtes françaises: Les sites-ateliers de programme frontal. *Oceanologica Acta*, *13*(4), 413–438.

Stumpf, R. P., & Pennock, J. R. (1989). Calibration of a general optical equation for remote sensing of suspended sediments in a moderately turbid estuary. *Journal of Geophysical Research*, *94*, 14363–14371.

Trees, C., Sanjuan-Calzado, V., Besiktepe, S., McKee, D., Bengil, F., Gunduz, M., et al. (2012). Optical, Physical and ecosystem regional modeling assessment (OPERA): A revolutionary. In *Ocean Optics XXI*. Glasgow.

Vellucci, V. (2007).*Optical properties in the Mediterranean open waters*. PhD Thesis, University of Napoli "Federico II", Naples.

Werdell, P. J., & Bailey, S. W. (2005). An improved in-situ bio-optical data set for ocean color algorithm development and satellite data product validation. *Remote Sensing of Environment*, *98*(1), 122–140.

Zaneveld, J. R. V., Kitchen, J. C., & Moore, C. (1994).The scattering error correction of reflecting-tube absorption meters. *Ocean Optics XII .International Society for Optics and Photonics*. http://doi.org/10.1117/12.190095.

APPENDICES

List of Abbrevations

a: Absorption coefficient

a_{cdom}: Absorption coefficient by colored dissolved organic matter

a_{nap}: Absorption coefficient by non-algal particles

AOPs: Apparent optical properties

a_p: Particulate absorption coefficient

a_{ph}: Absorption coefficient by phytoplankton

a_w: Absorption coefficient by water

b: Scattering coefficients

b_b: Backscattering coefficients

b_{bp}: Barticulate backscattering coefficient

b_{bw}: Backscattering coefficients by water

b_p: Particulate scattering coefficient

b_w: Scattering coefficients by water

c: Attenuation coefficient

CDOM: Colored dissolved organic matter

Chl: Chlorophyll-a

IOPs: Inherent optical properties

K_{bio}: Biologic contribution to diffusive attenuation coefficient

K_d: Diffusive attenuation coefficient

LWCC: Liquid waveguide capillary cell

NAP: Non-algal particulate

OAC: Optically active components

OD_{det}: Optical density by detritus

OD_p: Optical density by particles

PAR: Photosynthetically active radiation

PSICAM: Point source integrating cavity absorption meter

R_{rs}: Remote sensing reflectance

TSS: Total supended solids

VSF: Volume scattering function

Z_{eu}: Euphotic depth, Optical depth 4.6

Z_{pd}: First optical depth